Lawrence Berkeley National Laboratory

Title
APPLICATIONS OF HIGH RESOLUTION NMR TO GEOCHEMISTRY: CRYSTALLINE, GLASS, AND MOLTEN SILICATES

Permalink
https://escholarship.org/uc/item/6zx5g8jc

Author
Schneider, E.

Publication Date
1985-11-01

Peer reviewed
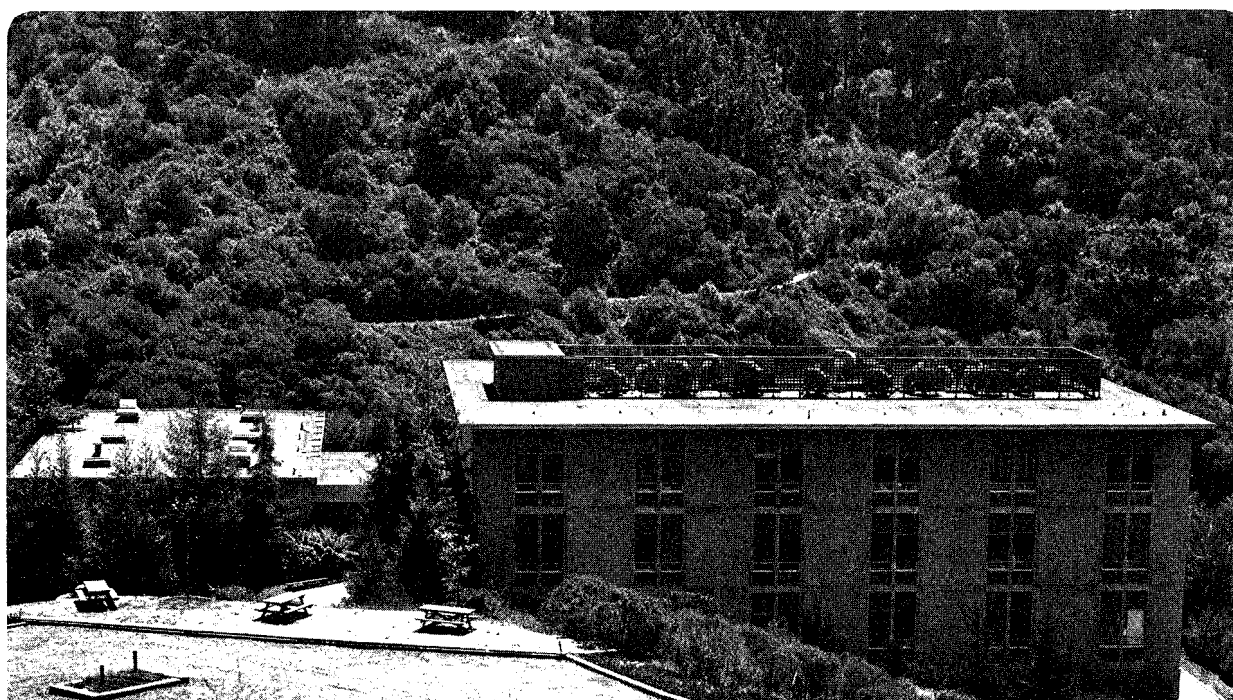
Lawrence Berkeley Laboratory
UNIVERSITY OF CALIFORNIA

Materials & Molecular Research Division

APPLICATIONS OF HIGH RESOLUTION NMR TO
GEOCHEMISTRY: CRYSTALLINE, GLASS,
AND MOLTEN SILICATES

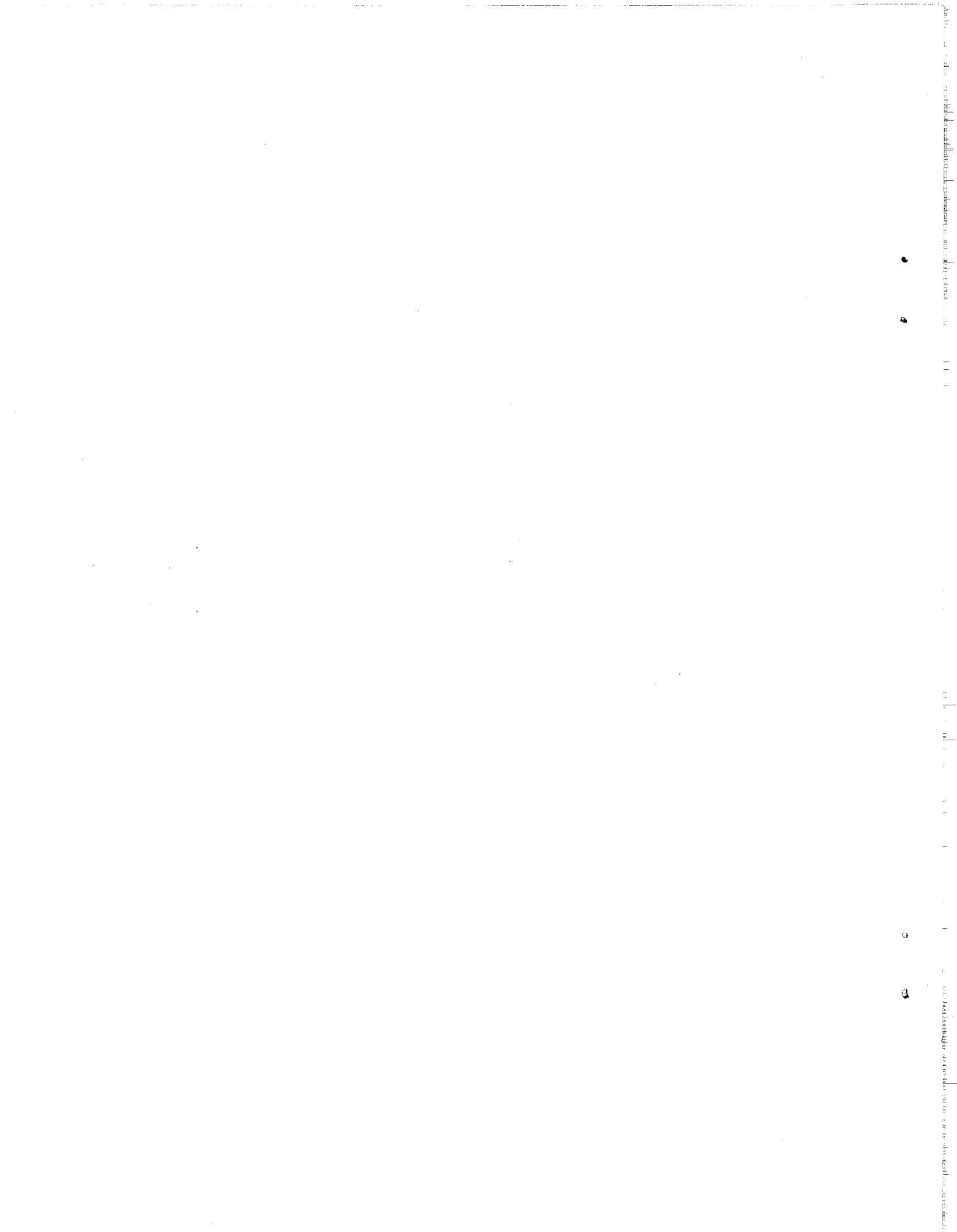E. Schneider
(Ph.D. Thesis)

November 1985

Applications of High Resolution NMR to Geochemistry:

Crystalline, Glass, and Molten Silicates

Erika Schneider

Lawrence Berkeley Laboratory
University of California
Berkeley, California 94720

November 1985

APPLICATIONS OF HIGH RESOLUTION NMR TO GEOCHEMISTRY:
CRYSTALLINE, GLASS, AND MOLTEN SILICATES

ERIKA SCHNEIDER

ABSTRACT

In the last fifteen years, Nuclear Magnetic Resonance (NMR) techniques have been developed which allow investigation of the properties of polycrystalline solids, amorphous materials, and sensitive biological samples in addition to expanding the capabilities of liquid state spectroscopy. This thesis describes some recent applications of solid state and high temperature NMR spectroscopy to the investigation of molecular structure and dynamics of molten, glass, and crystalline aluminosilicates.

The nuclear spin interactions and the associated quantum mechanical dynamics which are present in solid state NMR are introduced. A brief overview of aluminosilicate structure is presented and crystalline structure is then reviewed, with emphasis on the contributions made by ^{29}Si NMR spectroscopy. The local structure of glass aluminosilicates as observed by NMR, is presented with analysis of the information content of ^{29}Si spectra.

A high temperature (to 1300°C) NMR spectroscopic investigation of the local environment and dynamics of molecular motion in molten aluminosilicates is described. A comparison is made of silicate liquid, glass, and crystalline local structure. The atomic and molecular motions present in a melt are investigated through relax-

ation time (T_1 and T_2) measurements as a function of composition and temperature for ^{23}Na and ^{29}Si.

In Appendix A, magic angle spinning is reviewed, with emphasis on the interpretation of spinning sidebands. Appendix B contains computer simulations which are capable of predicting the effects of multiple pulse sequences in solid systems. The effect of several composite pulse sequences which compensate for magnetic dipole-dipole and electric quadrupole couplings in solids are shown by comparison of theoretical predictions and experimental results. The novel high temperature, high resolution NMR apparatus is described in Appendix C.

To my parents.

ACKNOWLEDGEMENTS

To mention everyone who has contributed to my stay at Berkeley would be impossible. First, I would like to thank my research director, Alex Pines, for his enthusiasm and encouragement, and for setting standards of excellence which are often taken for granted. Second, this thesis would have never occurred without the energy, patience, and knowledge of Jonathan Stebbins. Jonathan has guided me through the world of geochemistry and motivated the work within this volume.

The Pines group is an entity unto itself. The experiments I have performed rely on equipment and skills passed on to me from previous generations. In particular, many thanks are due to: Rob Tycko, for an understanding of spin system manipulations; Kurt Zilm, for enlightening my approach to probe building; Jim Murdoch, for introducing me to simulations of spin space and Jonathan Stebbins, and, for his indefatiguable sense of humor; Tony Bielecki, for his friendship and knowledge of electronics; and Jean Baum, Paul Jonsen, Miriam Gochin and Dave Shykind for passing along "tricks of the NMR trade."

The intellectual atmosphere inside the Chemistry Department has not precluded many enjoyable hours spent with chemists, and I wish to especially thank everyone on D-level and those involved with the many afternoon softball games. Also, the technical staff deserve a long list of praises, notably Don Wilkinson and Yau-Man Chan of the Electronics Shop.

Also, I wish to acknowledge the continual support and encouragement I have received from my parents and brother throughout my graduate school career. And, in the last final weeks of thesis preparation, many thanks are due to Dave Shykind, Ken Laughlin, Jonathan Stebbins, Shang-Bin Liu, Vicky Shannon and Dione Carmichael.

APPLICATIONS OF HIGH RESOLUTION NMR TO GEOCHEMISTRY:

CRYSTALLINE, GLASS, AND MOLTEN SILICATES

Table of Figures:

Table of Figures, continued

Table of Figures, continued

Table of Figures, continued

Table of Tables

CHAPTER I:

INTRODUCTION

In the past fifteen years Nuclear Magnetic Resonance (NMR) spectroscopy has evolved into a powerful technique capable of probing the magnetic and electronic interactions present in a wide variety of materials. In this thesis, the capabilities of NMR have been utilized to explore the high temperature properties of molten aluminosilicates and the local structure in glass and crystalline minerals.

The chemical and physical interactions of aluminosilicates are of interest in many industries, as well as in the geochemistry community. Ceramics, glass products, insulation, and catalysts are a few products encountered in daily life which are composed of silicate materials. For the geologist, however, silicates are the building materials of the earth. The interactions and physical properties of aluminosilicate minerals are investigated to better understand the formation, weathering and subsequent decomposition of the planetary crust. Furthermore, because mineral structure is strongly dependent upon the thermal history of the material as well as minor variations in the chemical composition, detailed studies of these minerals can be used to understand magmatic processes.

NMR is one of the most powerful techniques available for the investigation of materials which lack long range order. Polymers, glasses, resins, surface immobilized species, and liquid crystals are some of the materials which do not have crystalline order and cannot be investigated using diffraction techniques. Crystalline alumino-silicates can undergo high temperature and/or high pressure phase transitions which cause the reorientation of a material which has long range order to become a highly twinned crystal with multiple

defect sites. These phase transitions can cause some crystalline materials to have regularly spaced regions of short range order, and from an x-ray pattern, the material will appear to be disordered. NMR, however, can identify the different regions with local ordering and can provide quantitative information about defect sites.

^{29}Si MAS NMR spectroscopy has proven invaluable in the determination of silicon-aluminum local ordering. X-ray diffraction techniques have difficulty, even in single crystals, distinguishing aluminum atoms from silicon atoms because their atomic radii are almost identical and they can occupy the same structural positions. The only differentiating feature is that trivalent aluminum atoms have slightly shorter Al-O bond lengths than tetravalent silicon-oxygen bond lengths. The difference in Al-O distance is not possible to distinguish in many important geologic crystal structures because complex rotations, displacements, and twinnings occur relatively easily at the high temperature formation conditions. The sensitivity of ^{29}Si NMR to irregularities in crystalline silicate structure is presented in Chapter IV.

Properties of aluminosilicate glasses have been investigated by geochemists in an attempt to understand more about these materials in the high temperature molten states (in magmas, for example). A glass is presumed to be the quenched equivalent of a melt. That is, the structure of the melts at the glass transition temperature is retained in the glass state, except that the molecular motions are no longer present. However, the validity of this presumption has never been directly tested. Thermodynamically, a melt is substantially

different from the glass because of the dynamics present in the molten state. No technique, other than NMR, is capable of probing the electronic structure of all three phases: crystalline, glass, and molten state. In Chapter V, the local ordering and the effect of the network modifying cations on glass structure is presented. In Chapter VI, results from a high temperature (to 1300°C), high resolution NMR experiment on several aluminosilicate composition melts are compared to the structure found in the glass and crystalline states.

The dynamics present in molten aluminosilicates may also be investigated by NMR. Two types of techniques are available to detect and characterize molecular motions. One class of techniques, including NMR as well as neutron scattering and dielectric measurements (of molecules with a permanent dipole moment), is able to directly detect motions of molecules. Other techniques, such as x-ray diffraction and heat capacity measurements, are not sensitive to the motion, but instead measure the disorder introduced by molecular motions.[4] Thus, static and dynamic disorders cannot be distinguished using the second type of technique. The two types of experiments are complementary, together they are capable of characterizing the molecular motions present in most materials. Chapter VI compares the melt dynamics as investigated by NMR, to the macroscopic properties of the molten state.

CHAPTER II:

SPIN INTERACTIONS

II.1. Nuclear Spin Interaction Hamiltonians

Nuclear Magnetic Resonance (NMR) spectroscopy investigates the electronic and magnetic interactions of nuclear spin systems. The underlying power of NMR spectroscopy stems from the fact that over $\approx$ 90% of the known nuclei possess nonzero nuclear magnetic moments which allow for interaction with magnetic fields. The magnetic moment $\underline{\mu}$ is proportional to the nuclear spin angular momentum vector $\underline{I}$

$$\underline{\mu} = \gamma \hbar \underline{I} \tag{1}$$

where γ is the gyromagnetic ratio. The value of γ is characteristic for each nucleus.

II.1.i. Zeeman Interaction

Application of a magnetic field $\underline{H}_0$ produces an interaction energy for nuclei with nonzero spin angular momentum. The laboratory reference frame Hamiltonian which governs this situation is

$$\mathcal{H}_{Lab} = - \underline{\mu} \cdot \underline{H}_0 . \tag{2}$$

In the presence of a magnetic field, the spins precess about the direction of $\underline{H}_0$. In a large static magnetic field, the spin interactions (the wavefunctions) are time dependent. However, the Hamiltonian remains time independent in the Schroedinger representation.

In addition to interactions with the static external magnetic field, interactions of the spin with other spins may also be present within the system. Examples of these internal spin interactions, $\mathcal{H}_{int}$, include coupling of the spin magnetic moment to the electrons

orbiting the nucleus (chemical shielding), coupling of one magnetic moment to another (magnetic dipole-dipole and scalar coupling), and interaction of the nuclear quadrupole moment with the electric field gradient present at the nuclear site. All the $\mathcal{H}_{int}$ interactions contribute to the appearance of the NMR spectrum. The relative strengths of the internal interactions are located in Table 1 and compared to the Zeeman interaction strength.

In a solid sample, some of the internal spin interactions are anisotropic functions of orientation in the external magnetic field. For liquid or solution samples, the anisotropies of $\mathcal{H}_{int}$ are averaged by random molecular tumbling which occurs on a much faster timescale (< 10 nsec) than observable by NMR. In solid or oriented systems, isotropic motion usually does not occur, hence the spin interactions cause the spectral features to be dependent upon orientation of the external magnetic field with respect to molecular or crystal axes.

If $|H_o| \gg |\mathcal{H}_{int}|$ (the high field approximation), then the Zeeman Hamiltonian dominates the spectral appearance and in angular frequency terms, is given by[1,2,6]

$$\mathcal{H}_z = - \gamma \underline{H}_o \cdot \underline{I} = - \gamma H_o I_z = - \omega_o I_z \, . \qquad (3)$$

ω_o is the precession (or Larmour) frequency and is approximately 180 MHz and 362 MHz for protons (^1H) in the 42 kG and 85 kG, respectively, superconducting magnets which presently inhabit the Pines laboratory.

The eigenvalues for the Zeeman Hamiltonian are the eigenvalues of I_z, hence the $(2I + 1)$ allowed Zeeman energy levels are

Table 1: Relative Strengths of $\mathcal{H}$

Interaction	Strength (Hz)
Zeeman	$10^6 - 10^9$
Chemical Shift Anisotropy	$0 - 10^5$
Dipolar Coupling	$0 - 10^5$
Scalar Coupling	$0 - 10^4$
Quadrupolar Coupling	$0 - 10^9$

$$E = - \gamma \hbar H_O m \tag{4}$$

where $m = I, I-1, ..., -I$. The Zeeman eigenstates are equally spaced in energy, differing by

$$\Delta E = \gamma \hbar H_O = \hbar \omega_O . \tag{5}$$

ω_O is the nuclear Larmour frequency. The magnetic spin energy level splitting by a large external magnetic field is the strongest interaction which will be encountered in this thesis.

II.1.II. Radiofrequency Pulse Interactions

To observe the transitions between energy eigenstates, Fourier transform (FT) NMR techniques require application of an oscillating radiofrequency (rf) field orthogonal to the static field $\underline{H}_O$. The time dependent rf field $\underline{H}_1(t)$ is applied in square pulses of amplitude (Rabi frequency) ω_1 and phase ϕ. Setting $\hbar = 1$, and allowing the rf pulses to be given along the x axis, the representation of the laboratory frame Zeeman, rf and internal interaction Hamiltonian $\mathcal{H}_{int}$ is

$$\mathcal{H}_{Lab} = - \omega_O I_z + 2 \omega_1 I_x \cos(\omega t + \phi) + \mathcal{H}_{int} . \tag{6}$$

The $\mathcal{H}_{int}$ term contains all of the other interactions which are present in the nuclear spin system.

II.1.III. Rotating Reference Frame Transformation

In general, the interactions of interest in NMR spectroscopy are those which perturb the well characterized Zeeman energy levels. To emphasize $\mathcal{H}_{int}$, a transformation is made to a reference frame which

rotates at the Larmour frequency about the direction of the applied field $\underline{H}_o$. The transformation to the rotating reference frame partially removes the interaction with the static external field as well as causes the oscillatory time dependence of the applied rf field to vanish.[2] The transformation to the rotating reference frame (interaction representation) is given by

$$\mathcal{H}_{RF} = \mathcal{H}_{Rotating\ Frame} = U(t)\ \mathcal{H}_{Lab}\ U(t)^{-1} \qquad (7)$$

where the transformation $U(t) = \exp(-i\ \omega\ I_z\ t)$.

$$\mathcal{H}_{RF} = \exp(-i\ \omega\ I_z\ t)\ [-\omega_0\ I_z - \omega_1\ I_x\ \cos(\omega\ t + \phi)$$
$$+ \mathcal{H}_{int}]\ \exp(+i\ \omega\ I_z\ t) \qquad (8)$$

$$\mathcal{H}_{RF} = (\omega - \omega_0)\ I_z + 2\ \omega_1(t)\ [I_x\ \cos\ \omega t + I_y\ \sin\ \omega t]$$
$$\cdot\ \cos(\omega\ t + \phi) + U(t)\ \mathcal{H}_{int}\ U(t)^{-1} \qquad (9)$$

where $\omega - \omega_0 = \Delta\omega$ is the resonance frequency offset term. In the rotating frame, both the rf interaction and $U(t)\ \mathcal{H}_{int}\ U(t)^{-1}$ consist of a sum of terms, some of which are constant and others oscillate at multiples of ω. Since ω is much larger than ω_1 and $|\mathcal{H}_{int}|$, it is a good approximation to retain only the nonoscillatory terms of $\mathcal{H}_{RF}$. This truncation is known as the 'high field approximation' because the time dependent, nonsecular terms of the Hamiltonian will not perturb the energy levels to first order and can be ignored. Then,[1,2,6]

$$\mathcal{H}_{RF} = \Delta\omega\ I_z + \omega_1\ [I_x\cos\ \phi + I_y\sin\ \phi] + \mathcal{H}_{int}^{(0)} \qquad (10)$$

where $\mathcal{H}_{int} = \mathcal{H}_{int}^{(0)} + \mathcal{H}_{int}^{(1)}$,

$$[\mathcal{H}_{int}^{(0)}, I_z] = 0 \; ,$$

and $\qquad [\mathcal{H}_{int}^{(1)}, I_z] \neq 0.$

In NMR, spectrometers are configured such that measurements are made in the rotating frame. For this reason, $\mathcal{H}_{RF}$ will henceforth be refered to as $\mathcal{H}$ and the nuclear spin interactions present in $\mathcal{H}_{int}$ will be introduced in this interaction representation.

II.1.iv. Chemical Shielding Hamiltonian

Electrons in a molecule partially shield a nucleus from the effect of an applied external magnetic field. Local magnetic fields $\underline{H}_{local}$ are induced by the electron orbital currents and reflect the local electronic environment of the nucleus. Thus, the magnetic field at the nucleus is the sum of two terms

$$\underline{H}_{nucleus} = \underline{H}_o + \underline{H}_{local} \; . \tag{11}$$

The variations in local magnetic field cause chemically or crystallographically inequivalent nuclei to have different frequencies which satisfy the resonance condition.

If the nucleus is part of a molecule, the electrons are not able to freely precess about $\underline{H}_o$, and $\underline{H}_{local}$ is not necessarily parallel to $\underline{H}_o$. The chemical shielding in nonmetallic solids is represented by the anisotropic tensor $\underline{\underline{S}}$[1,6]

$$\mathcal{H}_{CS} = - \gamma \, \underline{H}_o \cdot \underline{\underline{S}} \cdot \underline{I} \; . \tag{12}$$

If the molecular motion present in liquids is isotropic and

occurs on a timescale much faster than NMR is able to detect (< 10 nsec), the screening tensor $\underline{\underline{S}}$ is averaged to an isotropic, dimensionless constant value S_{zz}. With $\underline{H}_0$ large (high field approximation) and in the z direction, then the liquid state chemical shielding Hamiltonian simplifies to

$$\mathcal{H}_{CS} = - \gamma \, H_0 \, S_{zz} \, I_z = - \sigma_{zz} \, I_z \, . \tag{13}$$

Incorporating the Zeeman interaction in the rotating frame

$$\mathcal{H}_0 = \mathcal{H}_{Z+CS} = [\, 1 - \sigma_{zz}] \, I_z \, , \tag{14}$$

as illustrated in Figure (1). Hence for positive values of σ_{zz}, the resonance is shifted to lower fields (lower frequencies). A low field shift implies that the nucleus is effectively screened from the constant applied magnetic field $\underline{H}_0$ by the surrounding electrons. If isotropic rearrangement in a sample is fast enough to average the anisotropic part of $\underline{\underline{\sigma}}$ to zero, then the isotropic chemical shift σ_z, is equal to σ_{iso}. In practice, measurements are made relative to σ_{iso} for some standard compound rather than a bare nucleus.

An NMR experiment measures the differences in chemical shielding between nuclear electronic environments. If the nucleus contains several chemically or crystallographically different sites, j, the liquid Hamiltonian becomes,

$$\mathcal{H}_0 = - \Sigma_j \, \sigma_{isoj} \, I_{zj} \, . \tag{15}$$

In a sample containing two chemically distinct types of nuclei and in

$$m_s = -1/2$$

$$\nu_0$$

$$+1/2$$

$$\nu_0 + \Delta\sigma$$

$$\underset{\sim}{H}_0$$

A

B
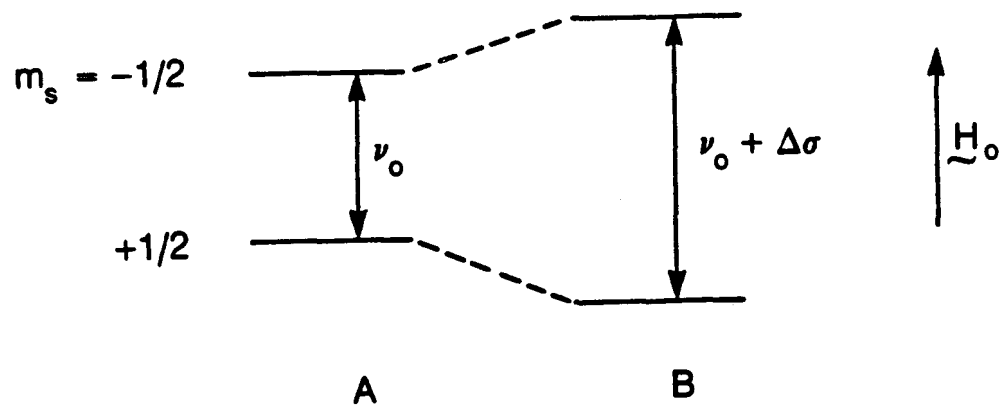
XBL 857-10630

<u>Figure 1</u>: Energy level diagram for a spin 1/2 nucleus in a strong static magnetic field. (A) The nuclear Zeeman energy levels. (B) Perturbation of the Zeeman levels by the chemical shielding term represented by $\Delta\sigma$.

the absence of any interactions between them, two resonance lines will be observed. The relative peak areas are indicative of the relative populations of the two sites, and the relative chemical shift, in frequency units, between nuclei 1 and 2 is given by

$$\omega_1 - \omega_2 = 2\pi \gamma \left[H_{1nuclear} - H_{2nuclear} \right]$$

$$= (\sigma_{iso1} - \sigma_{iso2}) \, 2\pi \gamma \, H_0$$

$$= (\sigma_{iso1} - \sigma_{iso2}) \, \omega_0 \, . \tag{16}$$

$H_{1nuclear}$ and $H_{2nuclear}$ are the magnetic fields influencing nuclei 1 and 2, respectively. The resonance frequency values are proportional to the strength of the constant magnetic field. Thus, all chemical shift differences (if measured in Hertz) increase if H_0 is increased. It is therefore usual (and useful) to report a field independent chemical shift difference measurement in parts per million (ppm). Relative to a standard reference the chemical shift of nucleus 1 is given by (the δ notation)

$$\delta(ppm) = \frac{\omega_1 - \omega_{ref}}{\omega_{ref}} \times 10^6 \, . \tag{17}$$

In a solid, molecular motion is slow and the magnetic shielding interaction is describable by a second rank tensor. The chemical shift anisotropy (CSA) tensor is dependent upon the molecular orientation with respect to the external magnetic field. From the CSA tensor, the three dimensional shielding of the nucleus by the surrounding electrons can be determined. The eigenvalues of the anisotropic chemical shift tensor $\underline{\underline{\sigma}}$ (σ_{11}, σ_{22}, σ_{33}), define several

experimentally measurable quantities. The isotropic chemical shift σ_{iso}, shielding anisotropy $\Delta\sigma$, and shielding asymmetry factor η are defined

$$\sigma_{iso} = 1/3 \ (\sigma_{11} + \sigma_{22} + \sigma_{33}) \ , \tag{18}$$

$$\Delta\sigma = \sigma_{33} - 1/2 \ (\sigma_{11} + \sigma_{22}) \ , \ \text{and} \tag{19}$$

$$\eta = (\sigma_{22} - \sigma_{11})/(\sigma_{33} - \sigma_{iso}) \ . \tag{20}$$

In a powdered sample, all possible orientations of crystallites are present and a resonance will be observed for each orientation of a particular nucleus in the external field, resulting in a broad peak. The spectral appearance of a powdered sample depends upon the shielding tensor principal axis elements, as illustrated in Figure 2.

II.1.v. Magnetic Dipole-Dipole Hamiltonian

The truncated magnetic dipolar interaction Hamiltonian in the rotating frame for homonuclear (I-I) nuclear spin pairs i and j in a solid is given by[1,2,6]

$$\mathcal{H}_{II} = \frac{1}{2} \sum_{i<j} \gamma_i^2 \ r_{ij}^{-3} \ (1 - 3\cos^2\theta_{ij})$$

$$\cdot [\ 3I_{zi}I_{zj} - \underline{I}_i \cdot \underline{I}_j \ ] \tag{21}$$

where r_{ij} is the internuclear distance, and θ_{ij} is the angle between $\underline{r}_{ij}$ and $\underline{H}_o$ the static magnetic field. Equation (21) is not the full dipolar Hamilitonian, terms which contribute to absorption frequencies near zero and $2\omega_o$ have been omitted because they correspond to second order perturbations of the Zeeman energy levels.

$\sigma_{11}=\sigma_{22}=\sigma_{\perp}$

A

σ_{22}

σ_{11}

σ_{iso}

σ_{33}

B

$\sigma_{33}=\sigma_{\parallel}$
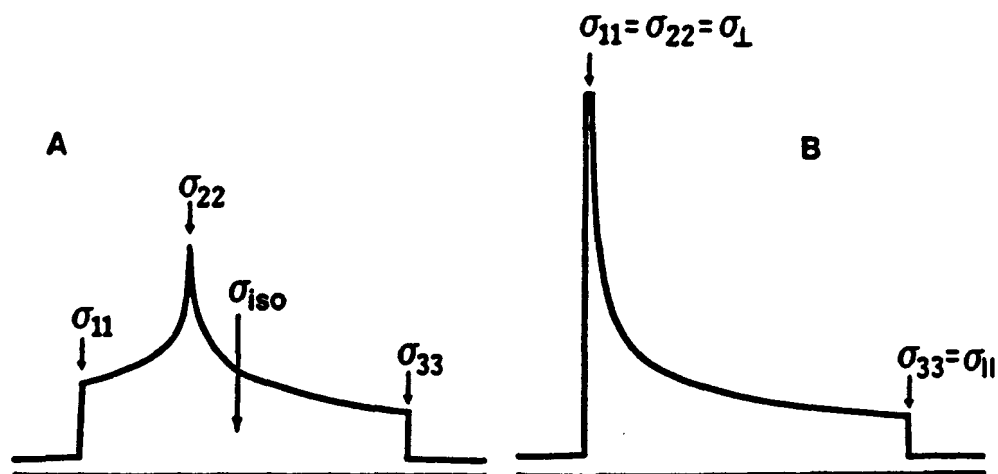
XBL 857-2987

Figure 2: Orientation dependent interactions, such as the CSA tensor, perturb the nuclear Zeeman energy levels and result in a characteristic pattern of line broadening. The chemical shift anisotropy patterns are affected by molecular motions. A nonaxially symmetric ($\eta > 0$) CSA tensor (A) can be averaged by pure rotations to give an axially symmetric ($\eta = 0$) pattern (B).

Dipole-dipole interactions are strongly dependent upon internuclear distance, r_{ij}, and are more important for nuclei in close proximity to each other. The average distance between isotopically dilute nuclei (e.g. natural abundance ^{29}Si and ^{13}C) is large enough such that the homonuclear dipolar coupling is unimportant. For heteronuclear dipolar interactions (between spins with different gyromagnetic ratios: γ_i, γ_j), the coupling is often strong but can be removed by multipulse 'decoupling' techniques. The truncated heteronuclear (I-S) magnetic dipole-dipole interaction Hamiltonian is given by[1,2,6]

$$\mathcal{H}_{IS} = \sum_{i<j} \gamma_i \gamma_j r_{ij}^{-3} (1 - 3\cos^2 \theta_{ij}) I_{zi} S_{zj} . \qquad (22)$$

(S_{zj} is the projection of the j nuclear spin angular momentum vector along the z axis.)

When molecular motions are present, the angle between the internuclear vector and the external field is averaged. If the motions are rapid and isotropic, as in a liquid sample, both of the dipolar interactions will be averaged to zero because the isotropic value of the term containing the angular dependence is $<\cos^2 \theta_{ij}> = 1/3$.

A scalar coupling, $\mathcal{H}_J$, often arises from the indirect coupling of a pair of nuclear spins i and j through the surrounding electrons. Homo- and heteronuclear spins may be coupled in this manner. $\mathcal{H}_J$ is field independent and usually much smaller than the other interactions present in $\mathcal{H}_{int}$.

II.1.vi. Electric Quadrupole Coupling Hamiltonian

In a molecule, the charges of surrounding valence electrons and other nuclei produce a large electric field gradient at each nucleus. A nucleus with spin greater than 1/2 has a nonspherical nuclear charge distribution, and as a consequence interacts with electric field gradients, even in the absence of an external magnetic field. In solids, the NMR spectra of quadrupolar nuclei are usually dominated by the nuclear quadrupole interactions.

The interaction energy between the nuclear quadrupole moment of spin I and the local electric field gradient can be described by the quadrupole Hamiltonian[1]

$$\mathcal{H}_Q = \underline{I} \cdot \underline{\underline{Q}}(t) \cdot \underline{I} . \tag{23}$$

$\underline{\underline{Q}}(t)$ is a tensor with elements proportional to the nuclear quadrupole moment Q and the electric field gradients ($\delta^2 V/\delta x^2$, $\delta^2 V/\delta x \delta y$, etc.)

$$\underline{\underline{Q}}(t) = \frac{eQ}{2I(2I - 1)} \underline{\underline{V}}(t) . \tag{24}$$

The components of $\underline{\underline{V}}(t)$, the electric field gradient (EFG) tensor, describe completely the orientation and magnitude of the EFG. In the principal axis coordinate system, $\underline{\underline{V}}(t)$ is a diagonal matrix with elements $V_{xx}(t)$, $V_{yy}(t)$, $V_{zz}(t)$ which uniquely describes the EFG in terms of the asymmetry parameter η and quadrupole coupling constant e^2qQ. If a nucleus is at a site of cubic symmetry, $V_{xx}=V_{yy}=V_{zz}$, the quadrupole coupling vanishes because the EFG's are all equal. Molecular rotations and diffusion cause changes in $\underline{\underline{V}}(t)$, and for

nuclei with spin greater than 1/2 (quadrupolar nuclei) this is often the dominant cause of relaxation. By convention, in the principal axis coordinate system of the EFG several definitions have been made[4]

$$|V_{zz}| \geqslant |V_{yy}| \geqslant |V_{xx}| \text{ and}$$

$$V_{zz} = eq \text{ , hence} \qquad (25)$$

$$\eta = (V_{xx} - V_{yy})/V_{zz} \text{ ,} \qquad \text{where } 0 \leqslant \eta \leqslant 1 \text{ .} \qquad (26)$$

In the principal axis system of the EFG tensor,

$$\mathcal{H}_Q = \frac{e^2 qQ}{4I(2I-1)} \left[3I_z^2 - I(I+1) + \frac{1}{2} \eta (I_+^2 + I_-^2) \right] \qquad (27)$$

I_+ and I_- are the quantum mechanical raising and lowering operators defined by

$$I_{\pm} = 2^{-1/2} \left[I_x \pm i I_y \right] \text{ .} \qquad (28)$$

$I_{\pm}$ connect the spin transitions (wavefunctions) of magnetic quantum number $\Delta m = \pm 1$.

Quadrupolar nuclei with noninteger spins (e.g. I=3/2: ^{11}B, ^{23}Na; and I=5/2: ^{17}O, ^{27}Al) are effected by quadrupole interactions differently than nuclei with integer spins. Because the investigation of aluminosilicate properties utilizes the properties of noninteger spin quadrupolar nuclei, their important properties are illustrated in Figures 3 through 5.
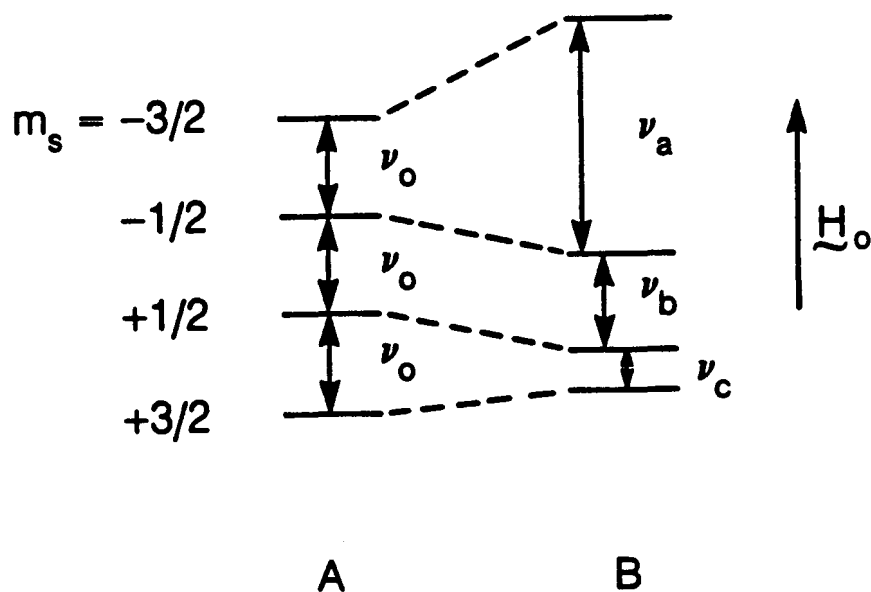
XBL 857-10629

Figure 3: The energy level diagram for a spin 3/2 nuclear magnetic dipole moment is shown interacting with a magnetic field. (A) In the absence of quadrupolar effects, four equally spaced energy levels with transition frequency ν_0 exist. (B) If a small electric quadrupole interaction (Q < Z) is present, the energy levels are shifted and three transitions are possible (ν_a, $\nu_b = \nu_0$, and ν_c).

Figure 4: A typical NMR spectrum of a polycrystalline or powdered
I=3/2 sample is shown. For most samples, only the central
(m = +1/2 to m = -1/2) transition is observed. For all
quadrupolar nuclei with nonintegral spins, the central
transition is not affected by first order quadrupolar
effects, but only by the much smaller second order effects.
The transition frequency is unaffected to first order
because the m = +1/2 to m = -1/2 levels are shifted by
the same amount.

Due to the randomly oriented crystallites, the inten-
sity of the 3/2 to 1/2 and the -1/2 to -3/2 transitions
are spread out over the entire range of possible frequen-
cies. The resonances of such transitions are normally too
broad to be observed in solid state NMR spectra unless the
quadrupolar interaction is very small. The solid state
spectrum depends on the value of the quadrupole coupling
constant and asymmetry parameter, and must be averaged
over the random nuclear orientations present in a polycry-
stalline sample. The change in transition frequency is
given by[4] $A_1 = (4 \ e^2qQ/h)^{-1}$.

XBL 857-10625

$$\nu_o - \frac{16}{9} A_2 \qquad\qquad \nu_o \qquad\qquad \nu_o + A_2$$
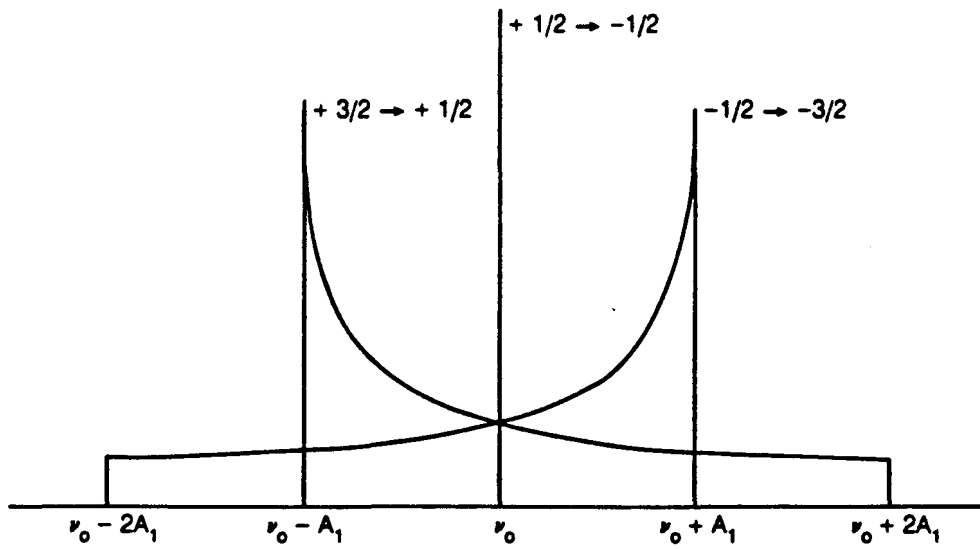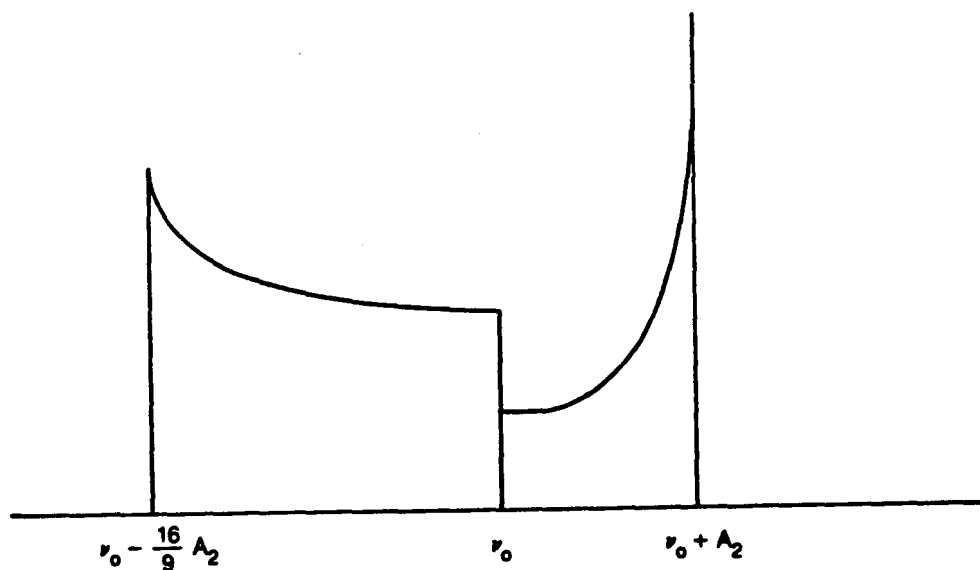
XBL 857-10628

Figure 5: An example of the second order nuclear quadrupole inter-
action is shown where the first order broadening (A_1) has
been removed by magic angle spinning (see Appendix A.3).
The central transition lineshape for spin 3/2 and $\eta = 0$
($V_{xx} = V_{yy}$, an axially symmetric EFG) is shown. If $\eta \neq 0$,
a more complicated (though still calculable) lineshape
will result. A_2 is the second order quadrupole broadening
and is defined by[4] $A_2 = \dfrac{3}{64} \dfrac{e^2 qQ}{\nu_o}$. The width of the second
order quadrupolar interaction is inversely proportional
to the magnetic field strength, hence the spectra of
quadrupolar nuclei will be much narrower at higher fields.

II.2. Density Matrix

The density matrix ρ and superoperator notation in Liouville space must be introduced before the coherent manipulations of spin space in Appendix B can be described.

II.2.i. Applicability of the Density Matrix

The basic tool of dynamic spin system quantum mechanics is the density matrix (density operator). This operator provides the connection between ensemble averaged statistical mechanics and finite spin system quantum mechanics. The statistical mixture of states present in a multispin system lends itself to this description.[5]

Initially the spin system is assumed to be in thermal equilibrium, and is described by the Boltzmann spin density operator[6]

$$\rho_B = \frac{\exp(-\beta \mathcal{H})}{Tr[\exp(-\beta \mathcal{H})]} \quad , \tag{30}$$

where $\beta = 1/kT$.

The initial state is often series expanded and truncated for $T > 1$ K, that is $\mathcal{H} << 1/\beta$. Accordingly, this truncation is called the high temperature approximation

$$\rho_B = \left\{ Tr[\exp(-\beta \mathcal{H})] \right\}^{-1} [1 - \beta \mathcal{H}] \quad . \tag{31}$$

In this limit, the partition function $Tr[\exp(-\beta \mathcal{H})]$ can undergo another series expansion and truncation to yield the number of states in the system. In a system which contains N spins of the same type I,

$$\text{Tr } [\exp(- \beta \mathcal{H})] = (2I + 1)^N .$$ (32)

In the laboratory frame, the Zeeman Hamiltonian $(- \omega_0 I_z)$ is usually the dominant term. Thus,

$$\rho_B = (2I + 1)^{-N} [\underline{1} + \omega_0 I_z/(kT)] .$$ (33)

Under a unitary transformation the unit matrix $\underline{1}$ does not evolve, and only contributes a constant factor to the NMR spectrum, hence it can be removed without affecting the spectral results. The laboratory reference frame reduced equilibrium density operator is written

$$\rho_0 = \frac{\omega_0}{(2I + 1)^N \, k \, T} I_z .$$ (34)

The form of ρ_0 is unchanged by rotation about the z axis (transformation to the rotating frame), hence the reduced equilibrium density operator in the rotating frame is also given by equation (34).

II.2.ii. Time Evolution and Pulsed NMR

Fourier transform NMR requires application of rf pulses as described in section II.1.ii. In equation (6), t is the pulse duration, hence ωt is the angle subtended by the magnetization due to a rf pulse along the x axis. In a shorthand notation, when $\omega t = \pi/2$, the pulse is known as a 90°_x (or $\pi/2_x$), where x is the axis in the rotating frame about which the pulse is given. If $\omega t = \pi$, then the pulse is an 180°_x.

After application of a $\pi/2$ pulse in the y direction of the rotating frame

$$\rho(t=0) = \frac{\omega_0}{(2I + 1)^N \, k \, T} \, I_x \, . \tag{35}$$

This state now evolves via the spin interactions present in $\mathcal{H}_{int}(t)$ according to the Liouville-von Neumann equation

$$\frac{d}{dt} \rho(t) = -i \, [\mathcal{H}_{int}(t), \rho(t)] \tag{36}$$

which has the solution

$$\rho(t) = U(t) \, \rho(0) \, U^+(t) \tag{38}$$

where

$$U(t) = T \exp [-i \int_0^t \mathcal{H}_{int}(t') \, dt' \, . \tag{39}$$

T is the Dyson time ordering operator[7] and $U^+(t)$ is the adjoint of $U(t)$ with $U^+(t) = U^{-1}(t)$, because $\mathcal{H}_{int}(t)$ is a Hermitian operator. Hence, evolution under $\mathcal{H}_{int}(t)$ is a unitary transformation of the density operator.

Experimental observation of the magnetization evolution and decay is made in the rotating frame along the x and y axis. The NMR observables are the amplitude and phase of the magnetization as a function of time. The magnetization at time t is proportional to $<I_x(t)>$ or $<I_y(t)>$, given by

$$<I_x(t)> = Tr [I_x \, \rho(t)] \, , \tag{40}$$

and similarly for $<I_y(t)>$. The free induction decay (FID, or the observed macroscopic magnetization decay) may be decomposed into two terms. Neglecting relaxation, the form of the FID is purely

sinusoidal, oscillating at the resonance offset frequency; in the presence of relaxation, the FID can be decomposed into a sinusoid term multiplied by an exponential decay term.

This technique of manipulating the spin system via the density matrix allows realistic numerical simulations of NMR experiments to be performed via matrix or irreducible tensor calculations.

CHAPTER III:

ALUMINOSILICATE STRUCTURE

III.1. Crystalline Silicates

Pure SiO_2 occurs in many forms, quartz, tridymite and crystobalite are three examples. In silica, the silicon atom is always tetrahedrally bound to four oxygen atoms, and the Si-O bonds have a considerable amount of ionic character.[30] Alkali metal carbonates may be fused with silica to drive off CO_2 and produce a range of alkali silicate compositions. Silicates which have a high alkali metal content (also known as alkali rich) are water soluble. With low alkali content, silicates can become very water insoluble. Most silicates are composed of silicon atoms tetrahedrally coordinated to four oxygen atoms, although a few 5- or 6-coordinated compounds are known to exist. The investigations presented in this thesis involve species which have tetrahedral silicon coordination.

III.1.i. Silicate Structure

The basic silicate structural unit is the SiO_4^{4-} tetrahedron. All units are known as Q-type (quaternary units), because each silicon atom is bound to four oxygen atoms. In crystalline silicate compounds the SiO_4^{4-} tetrahedra occur as individual structural units (orthosilicates, or nesosilicates), or bound via oxygen atoms shared with other tetrahedra. Condensation of silicate anions occurs through combining two or more tetrahedra by sharing oxygen atoms (or forming oxygen atom 'bridges') in pairs (sorosilicates), in small cyclic groups (cyclosilicates; Figure 6), in infinite chains (metasilicates, or ionosilicates; Figure 7), in infinite sheets (phyllosilicates; Figure 8), or in three dimensional structures (tectosilicates).

O = O

⊙ = Si
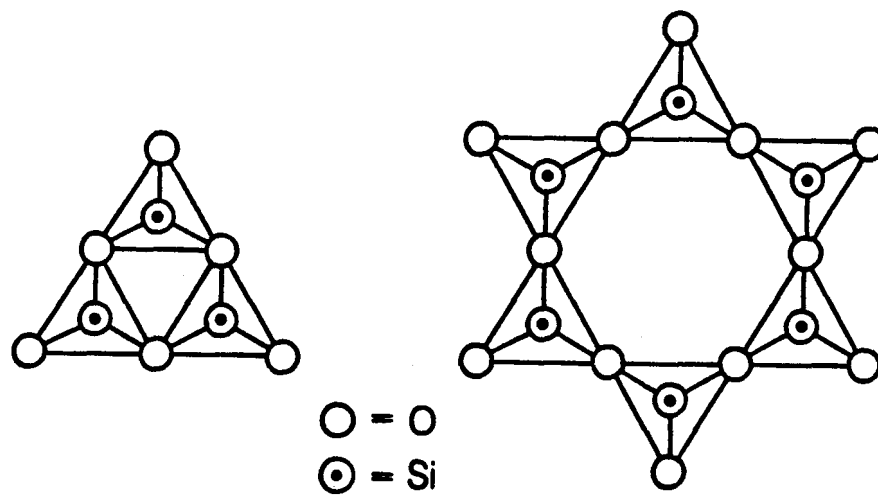
XBL 857-10631

Figure 6:   Examples of crystalline cyclosilicate units, a six mem-
bered ring and a three membered ring.   Oxygen atoms (sym-
bolized by a large, open circle) form "bridges" between
the silicon atoms (designated by a dot enclosed by a
circle).   The Si-O-Si bond angle and Si-O bond length can
differ for various silicate materials.
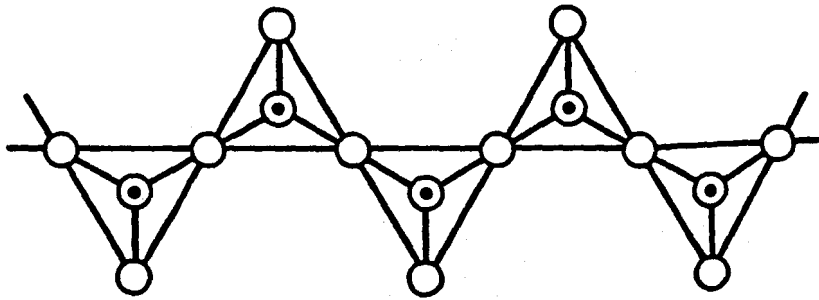
XBL 857-10626

Figure 7: A crystalline chain (meta- or iono-) silicate.
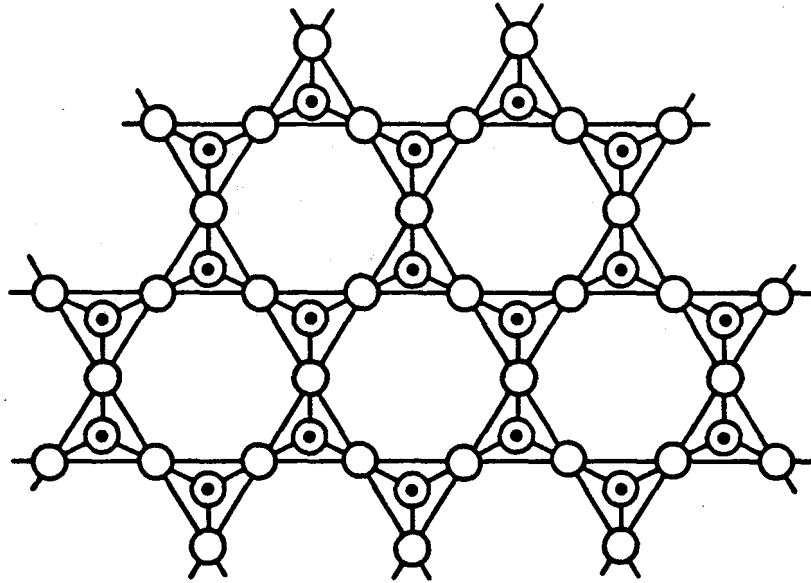
XBL 857-10627

Figure 8:   A crystalline sheet silicate (phyllosilicate) composed of
interconnected six membered rings.

Polymerization of silicate anions can produce a range of Si-O-Si bond angles and Si-O bond lengths. For example, in a sorosilicate, the Si-O-Si bond angle may range from $133°$ to $180°$.[29,74]

All silicate anions can be described in combinations of Q^n units, where the superscript n refers to the number of second coordination sphere silicon atoms (or other tetrahedral units) linked through oxygen bridges to the central silicon atom. Silicon in isolated silicate (SiO_4^{4-}) tetrahedra are known as Q^0 groups, pairs are Q^1, rings and chain end groups (Q^2), chain branching sites and sheet silicates (Q^3), and fully crosslinked three dimensional framework sites are Q^4 polymerization species.[96]

To balance the framework charge, cations, M^{n+}, are present and occupy intersitial sites. If all oxygen atoms are assumed to be coordinated with only one or two cations, then the degree of polymerization can, in general, be calculated from the composition of the silicate alone. Many sheet silicates (phyllosilicates) are bound together by the cations which lie between the layers. The cationic bonds between tetrahedrally coordinated silicate sheets are fairly weak. Examples of phyllosilicate structure are found in micas; these minerals are easily cleaved into thin sheets. In three dimensional silica polymorphs, every oxygen atom bridges between two silicon tetrahedra, and no cations are required for electroneutrality.

III.1.ii. Aluminosilicate Structure

Silicon tetrahedra may be replaced with aluminum tetrahedra (AlO_4^{5-}). The negative charge of the framework (equal to the number of constituent aluminum atoms) is balanced by cations M^{n+}, typically sodium, potassium, or calcium. In many aluminosilicates, tetrahedral coordination of aluminum atoms by four oxygen atoms will occur, although aluminum can also occupy a change a charge balancing or network modifying site. In a tectosilicate, each silicate or aluminate tetrahedron is linked, through oxygen bridges, to four other tetrahedra. However, Al-O-Al linkages are known to be thermodynamically less favorable than Al-O-Si or Si-O-Si bonds (Loewenstein's aluminum avoidance principle).[132] Other elements such as Ga, Ge, and B may substitute for Si and Al in the silicate framework if charge balancing cations are also included. Aluminosilicates are structurally diverse and are very valuable commercially as zeolites and ceramics.

A common property of zeolites is the presence of microscopic pores in a three dimensional framework (Figure 9). The wide variety of long range order possible in aluminosilicate structure makes the dimensions, configurations and properties of these pores vary considerably for different types of zeolites. Most pores, channels, or cavities are of molecular size and allow diffusion of various small molecules and water to occur. The diversity of pore configurations, combined with the selectivity and ease of synthesis or modification make zeolites useful as ion exchangers, molecular sieves, and catalysts.
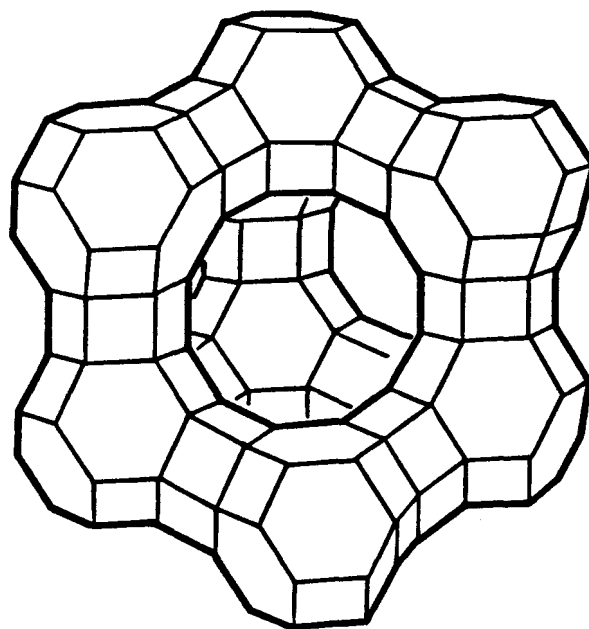
FAUJASITE

XBL 8511-4713

Figure 9: The structure of Na-Y, a faujasite zeolite. The vertices
of the three dimensional polyhedron are silicon atoms.
The lines connecting the vertices are composed of Si-O-Si
bonds. In most zeolites, large pores and cavities are
present.

III.2. Glass Silicate Structure

Silicate glasses are interesting not only due to their commercial importance, but also because they provide a snapshot view of the molten state. In a melt, the molecular and atomic motions that are most obvious in diffusion and viscous flow also contribute to the bulk properties such as entropy, heat capacity and density.[64-66] As a melt is quenched, the local liquid structure at the glass transition temperature (T_g) is preserved. The quenched in liquid structure has been observed in glasses by infrared and Raman spectroscopy,[54-57,60,68,70,101] x-ray and neutron scattering,[52,53,71] x-ray photoelectron spectroscopy[75,88] and ^{29}Si magic angle spinning (MAS) NMR spectroscopy.[17,35,62,63,85,89]

III.2.i. Glass Formation

The slow cooling of molten silica (SiO_2) will yield a glassy material. Different silicate compositions may or may not form a glass structure, dependent upon the rate of cooling from a molten state. Rapid cooling or quenching at the rate of thousands of degrees centigrade per second is often required to produce a homogeneous glass.

III.2.ii. Silicate Speciation

The dynamics and disorder present in a molten silicate cause the corresponding glass to have much less long range order, and much greater variations in Si-O-Si bond angles and Si-O bond lengths than are present in crystals. From Raman spectroscopic evidence, a range

of silicate species have been hypothesized to exist in a glass.[56,60,101]

For a disilicate (Q^3) glass such as $Na_2Si_2O_5$, the nature of silicate polymerization can be described by[76]

$$Si_2O_5^{2-} \rightleftharpoons SiO_3^{2-} + SiO_2 \tag{41}$$
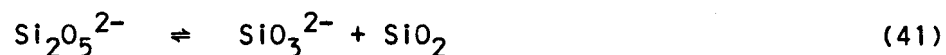
where $Si_2O_5^{2-}$, SiO_3^{2-}, and SiO_2 refer to structural units with sheet-like, chain-like, and three dimensional framework environments, respectively. For any Q^3 glass, Equation (41) can be rewritten in more general terms:

$$2\,Q^3 \rightleftharpoons Q^2 + Q^4 , \tag{42}$$

where only the relative number of bridging and nonbridging oxygen atoms are specified. For metasilicate glasses, equilibria such as

$$2\,Q^2 \rightleftharpoons Q^1 + Q^3 \quad \text{and} \tag{43}$$

$$2\,Q^2 \rightleftharpoons Q^0 + Q^4 \tag{44}$$

have been proposed as mechanisms to describe changes in polymerization state. In most silicate compositions, it is assumed that some of each species is present in glasses and melts. General polymerization state changes can be described using Q^n notation in the following equilibrium

$$2\,Q^n \rightleftharpoons Q^{n-1} + Q^{n+1} . \tag{45}$$

The type of equilibrium which can be affected by the identity of an alkali or alkaline earth cation now involves Si-Al distri-

butions instead of variations in Q^n populations. If Q^4[k Al] symbolizes a three dimensional framework silicate tetrahedra linked via oxygen atom bridges to k aluminate tetrahedra ($0 < k < 4$), then the proposed equilibrium expression describing the distribution of aluminum in a glass is[87]

$$2 Q^4 \text{ [k Al]} \rightleftharpoons Q^4 \text{ [(k+1) Al]} + Q^4 \text{ [(k-1) Al]} . \qquad (46)$$

Different network modifying cations are expected to shift these glass equilibria to the left or to the right. To the left implies the same type of silicate polymerization as found in the corresponding crystal, with an approximately even distribution of network modifying cations. An equilibrium shifted to the right implies a bunching of cations near those silicate units with extra nonbridging oxygens and a depletion of cations near silicate units with fewer nonbridging oxygen atoms. An inhomogeneous cation or aluminum atom distribution in the glass state implies that domains with different compositions, structures and electronic characteristics have formed.

CHAPTER IV:

NMR SPECTROSCOPY OF CRYSTALLINE SILICATES

The information obtainable using NMR spectroscopic techniques is complementary to data derived from other types of measurements. NMR is a sensitive probe of the local environment of nonzero spin nuclei, whereas x-ray diffraction, and neutron scattering examine the long range order of the entire sample, and Raman and IR spectroscopies are sensitive only to specific bonds.

^{29}Si NMR has proven to be a powerful technique for investigating the local structures of amorphous phases, glasses and various poly-crystalline materials such as clays and zeolites. These materials have local ordering which can not be readily determined by single crystal diffraction techniques. Quantitative information on the types of sites present and the extent of order or disorder present at a given site is easily (and quickly) obtained without loss or destruction of the sample. The acquired data (chemical shifts, chemical shielding anisotropy tensors, or electric field gradient tensors) can be interpreted in terms of types of chemical bonding (e.g. electron distribution, bond angles, and bond lengths). In addition, NMR may be used to determine the rates of motion, reorien- tation and chemical reaction of the various species present.

IV.1. ^{29}Si Chemical Shift

Silicon is second only to oxygen in weight percent of the earth's crust ($\approx$ 21%),[30,121] and is found in an enormous diversity of minerals. The local electronic environment surrounding silicon is conducive to investigation by NMR because ^{29}Si, the only naturally occuring NMR-active isotope of silicon, possesses a spin angular

momentum of 1/2. An isotopic abundance of 4.7% classifies [29]Si as a rare spin nucleus, hence most of the NMR techniques developed for use on natural abundance ^{13}C samples are directly applicable for investigation of silicon containing compounds.

IV.1.1. [29]Si Chemical Shifts in Aqueous Silicate Solutions

The full range of [29]Si chemical shifts is over 500 ppm,[4] but most compounds are found in a range of ≈ 120 ppm. Tetramethylsilane (TMS) is the accepted reference compound. The range of [29]Si chemical shift anisotropy is small[8] (< 200 ppm) and shows contributions from the bonding electrons in d orbitals and the fourth coordination sphere.[117] High resolution ^{29}Si NMR has been used to determine the structure of various silicate anions present in solutions. In silicate solutions the typical range of isotropic [29]Si chemical shifts is -60 to -120 ppm from TMS, this distribution is divided into ranges for silicon in various different polymerization states and aluminum coordination sites.[16,17]

The spectrum of an aqueous silicate solution changes dramatically as a function of pH and the sodium to silicon ratio. When this ratio is small, more polymeric silicate anions are present. As sodium or water (to change the pH) is added, the higher polymerized structures decrease in concentration until only the monosilicate anions remain.[47] R. Harris and coworkers have used isotopically labeled silicon and high field (99 MHz for [29]Si) two-dimensional NMR techniques to unequivocally assign individual resonance lines to specific silicate species based on the [29]Si-[29]Si scalar

couplings.[125-127]

IV.1.ii. [29]Si Chemical Shifts in Crystalline Silicates

In ^{29}Si NMR spectroscopy, isotropic chemical shifts vary systematically as a function of silicate structure. Lippmaa et al.[31] first observed the existence of distinct [29]Si chemical shift ranges for different types of silicate structural units in crystalline materials. The [29]Si nucleus becomes deshielded (δ, relative to a TMS standard, becomes less negative) as the number of Si-O-Si bridging oxygens decreases.[31] Also, silicon-29 chemical shifts are affected by the number of adjacent aluminate tetrahedra. In all aluminosilicates, silicon nuclei become deshielded (δ less negative) as the number of neighboring aluminate tetrahedra increases from zero to four. The reasonably good separation in these shift ranges has greatly facilitated the study of Si-Al ordering in zeolites.[9,32,67] In Table 2, the published isotropic [29]Si chemical shifts of crystalline silicates and aluminosilicates (non-zeolites) are presented.

^{29}Si NMR has proven to be particularly useful in mineralogy for structure determination, since data on the local silicon environments is very difficult (or impossible) to determine using other techniques. However, rigorous calculation of the NMR spectra of solids of known structure and composition is not yet possible. Due to the complexity of the effects of chemical bonding and electronic configuration on nuclear spins, spectral interpretation is limited to empirical [29]Si chemical shift correlations. Progress is being made, however, in the theoretical prediction of NMR chemical shifts.[128-130]

Table 2:   Isotropic ^{29}Si chemical shifts of crystalline silicates.

Composition (Mineral Name)	Spectral Assignment	Peak Position[+] (ppm from TMS)	Reference
NaH_3SiO_4	Q^0	−66.4	9
$Na_2H_2SiO_4 \cdot 8.5H_2O$	Q^0	−67.8	9
$(CaOH)CaHSiO_4$	Q^0	−72.5	9
$CaNaHSiO_4$	Q^0	−73.5	9
Li_4SiO_4	Q^0	−65*	91
Li_4SiO_4	Q^0	−64.9	89, 118
Mg_2SiO_4 (forsterite)	Q^0	−62	28
Mg_2SiO_4 (forsterite)	Q^0	−61.9	118
$Mg_2Fe_2SiO_4$ (olivine)	Q^0	−62	118
Ba_2SiO_4	Q^0	−70.3	118
$CaMgSiO_4$ (monticellite)	Q^0	−66	28
$\alpha-Ca_2SiO_4$	Q^0	−70.3	89, 118
$\beta-Ca_2SiO_4$	Q^0	−71.4	118
$\gamma-Ca_2SiO_4$	Q^0	−73.5	118
Al_2SiO_5 (kyanite)	Q^0	−82.9	118
Al_2SiO_5 (kyanite)	Q^0	−83	28
$Mg_5Si_2O_8 \cdot F \cdot H_2O$ (chondrodite)	Q^0	−60	118
Ca_3SiO_5	Q^0	−69 to −75[##]	118

Table 2, continued

Composition (Mineral Name)	Spectral Assignment	Peak Position[+] (ppm from TMS)	Reference
$BeSiO_4$ (phenacite)	Q^0	−74.2	118
$ZrSiO_4$ (zirkon)	Q^0	−81.6	118
Al_2SiO_5 (andalusite)	Q^0	−79.8	118
Al_2SiO_5 (andalusite)	Q^0	−80	28
$Al_2[F_2/SiO_4]$ (topaz)	Q^0	−85.6	118
Al_2SiO_5 (sillimanite)	Q^0	−87.1	118
Na_4SiO_4	Q^1 Q^0	−68.9 −65	89
$Ca_3Si_2O_7$ (rankinite)	Q^1	−74.5, −76.0	89, 118
$Ca_2Al_2SiO_7$ (gehlenite)	Q^1	−72	28
$Ca_2MgSi_2O_7$ (akermanite)	Q^1	−73	28
$CaAl_2Si_2O_7(OH)\cdot H_2O$ (lawsonite)	Q^1	−81	28
$Ca_6Si_2O_7(OH)_6$ (tricalcium silicate hydrate, TCSH)	Q^1	−84	122
$Zn_4(Si_2O_7)(OH)\cdot H_2O$ (hemimorphite)	Q^1	−80	28
$Zn_4(OH)_2-Si_2O_7\cdot H_2O$ (hemimorphite)	Q^1	−77.9	9
$Ca_6(OH)_6Si_2O_7$	Q^1	−82.6	9

Table 2, continued

Composition (Mineral Name)	Spectral Assignment[†]	Peak Position[+] (ppm from TMS)	Reference
$Sc_2Si_2O_7$ (thortveitite)	Q^1	-95.3	74, 118
$\beta-Y_2Si_2O_7$	Q^1	-92.9	74, 118
$In_2Si_2O_7$	Q^1	-87.7	74, 118
$\alpha-La_2Si_2O_7$	Q^1	-83.2	74, 118
$Ca_3Si_2O_7$	Q^1	-74.5	74
$Li_6Si_2O_7$	Q^1	-72.4	74
$Li_6Si_2O_7$	Q^1 Q^1 $Q^0?Q^1$	-74.6 -72.4 -65.5	89
$Na_6Si_2O_7$	Q^1	-68.4	74
$Na_6Si_2O_7$	Q^2 Q^1	-77.0 -68.4	89, 118
$Al_{13}(OH, F)_{16}-F_2Si_5O_{20}/Cl$ (zunyite)	Q^{1**}	-96.7	74
Li_2SiO_3	Q^2	-80*	91
Li_2SiO_3	Q^2	-75	90
Li_2SiO_3	Q^2	-74.5	89, 118
Na_2SiO_3	Q^2	-76.8	89, 118
$BaTiSi_3O_9$ (benitoite)	Q^2	-94.2	118
$BaTiSi_3O_9$ (benitoite)	Q^2	-93	90
$K_4H_4Si_4O_{12}$ (potassium cyclo-tetrasilicate, KCTS)	Q^2	-88	31
$(Me_4N)_8Si_8O_{20}$ (tetramethylammonium silicate hydrate, TMAS)	Q^{2**}	-99	122

Table 2, continued

Composition (Mineral Name)	Spectral Assignment	Peak Position[+] (ppm from TMS)	Reference
$MgSiO_3$ (enstatite)	Q^2	-81, -83	28
$MgSiO_3$ (clinoenstatite)	Q^2	-81, -83.5	17
$Mg_2Si_2O_6$ (orthoenstatite)	Q^2	-82	118
Mg_2SiO_4	Q^2	-62	13
$CaMgSi_2O_6$ (diopside)	Q^2	-84	28
$CaMgSi_2O_6$ (diopside)	Q^2	-82	63
$CaMgSi_2O_6$ (diopside)	Q^2	-84	118
$CaSiO_3$ (wollastonite)	Q^2	-89	28
$CaSiO_3$ (wollastonite)	Q^2	-88.5	17
$CaSiO_3$ (wollastonite)	Q^2	-88.0	9
α-$Ca_3Si_3O_9$ (psuedowollastonite)	Q^2	-83.5	118
β-$Ca_3Si_3O_9$ (β-wollastonite)	Q^2	-89.0	118
$CaMgSiO_3$	Q^2	-84	17
$SrSiO_3$	Q^2	-85	28
$BaSiO_3$	Q^2	-80	28
$Ca_2SiO_3 \cdot (OH)_2$ (hillebrandite)	Q^2	-86.3	89, 118
$Ca_2SiO_3 \cdot (OH)_2$ (hillebrandite)	Q^2	-86.3	9

Table 2, continued

Composition (Mineral Name)	Spectral Assignment	Peak Position[+] (ppm from TMS)	Reference
$Ca_2NaHSi_3O_9$ (pectolite)	Q^2	-86.3	118
$Ca_2NaHSi_3O_9$ (pectolite)	Q^2	-86.3	9
$Ca_4(OH)_2Si_3O_9$ (foshagite)	Q^2‡	-84.8, -86.4	9
$Ca_4Si_3O_9(OH)_2$ (foshagite)	Q^2‡	-84.8, -86.4	118
$Ca_6Si_6O_{17}(OH)_2$ (xonotlite)	Q^2 Q^3	-86.8 -97.6, -98.1	118
$Ca_6(OH)_2Si_6O_{17}$ (xonotlite)	Q^2 Q^3	-86.8 -97.8	9
$Ca_2Mg_5(Si_4O_{11})_2-$ $(OH)_2$ (fibrous tremolite)	Q^{2}†† Q^{3}††	-87.8 -92.2	118
$Ca_2Mg_5Si_8O_{22}(OH)_2$ (tremolite)	Q^2	-91, -88	28
$LiAl[Si_2O_6]$ (spodumene)	Q^2	-91.6	118
$LiAl[Si_2O_6]$ (spodueme)	Q^2	-92	28
$NaAl[Si_2O_6]$ (jadeite)	Q^2	-91.8	118
$Al_2Be_3Si_6O_{18}$ (beryl)	Q^2	-102.6	118
Al_2SiO_5 (sillimanite)	Q^2	-87	28
$K_4H_4Si_4O_{12}$	Q^2	-87.5	9
$(Li_2O)_{0.4}(SiO_2)_{0.6}$	Q^2 Q^3 Q^4	-75* -90* -110*	91

Table 2, continued

Composition (Mineral Name)	Spectral Assignment	Peak Position[+] (ppm from TMS)	Reference
$Al_{13}O_4(OH, F)_{16}F_2^-$ $[Si_5O_{16}]Cl$ (zunyite)	Q_2^{2**} Q_4^{4**}	-91.3, -96.7 -128.2	29
$(Li_2O)_{0.33}(SiO_2)_{0.67}$	Q^3	-85[*]	91
$Li_2Si_2O_5$	Q^3	-92.5	17
$Li_2Si_2O_5$	Q^3	-93	28
$Na_2Si_2O_5$	Q^3	-94.5	17
$Na_2Si_2O_5$	Q^3	-95	28
$\alpha-Na_2Si_2O_5$	Q^3	-94.4	89
$K_2Si_2O_5$	Q^3	-91.5, -93, -94.5	17
$BaSi_2O_5$	Q^3	-93.5	17
$KCa_4[Si_4O_{10}/F]$ $\cdot 8\ H_2O$ (apophyllite)	Q^3	-92	89
$KCa_4(Si_4O_{10})_2^-$ $\cdot F \cdot 8H_2O$ (apophyllite)	Q^3	-92.0	118
$Mg_3Si_4O_{10}(OH)_2$ (talc)	Q^3	-98	28
$Mg_3(OH)_2Si_4O_{10}$ (talc)	Q^3	-98.1	9
$Mg_3Si_4O_{10}(OH)_2$ (talc)	Q^3	-97	122
$Mg_3Si_4O_{10}(OH)_2$ (talc)	Q^3	-98.1	31, 118
saponite	Q^3	-95	31
lectorite	Q^3	-95	31
llano vermiculite	Q^3	-92	31

Table 2, continued

Composition (Mineral Name)	Spectral Assignment	Peak Position[+] (ppm from TMS)	Reference
$Al_2Si_4O_{10}(OH)_2$ (pyrophyllite)	$Q^3[0\ Al]$	-95	28
$Al_2[Si_4O_{10}](OH)_2$ (pyrophyllite)	$Q^3[0\ Al]$	-95.0	118
$Al_2Si_4O_{10}(OH)_2$ (pyrophyllite)	$Q^3[0\ Al]$	-94	122
$Mg_8Si_{12}O_{30}$ $(OH_2)_4(OH)_4 \cdot 8H_2O$ (sepiolite)	Q^3	-92, -95, -98.5	143
$Mg_2Al_2Si_8O_{20}$ $(OH_2)_4(OH)_2 \cdot 4H_2O$ (palygorskite)	$Q^3[0\ Al]$	-92, -98	143
$(Al, Mg)_8-$ $(Si_4O_{10})_3(OH)_{10} \cdot 12H_2O$ (montmorillonite)	Q^3	-93	28
$CaBSiO_4(OH)$ (datalite)	Q^3	-83	28
$CaAl_2[Al_2Si_2O_{10}]-$ $(OH)_2$ (margarite)	$Q^3[3\ Al]$	-75.5	118
$CaAl_2[Al_2Si_2O_{10}]-$ $(OH)_2$ (margarite)	$Q^3[3\ Al]$	-73	122
$LiAl[Si_4O_{10}]$ (petalite)	Q^3	-87	118
$KMgAl[Si_3O_{10}]$ (phlogopite P8)	$Q^3[0\ Al]$ $Q^3[1\ Al]$	-91 -86	122
$KMgAl[Si_3O_{10}]$ $(F; OH)_2$ (phlogopite)	$Q^3[1\ Al]$	-84	118
$KAl_2[AlSi_3O_{10}]-$ $(OH)_2$ (muscovite)	$Q^3[\ Al][+]$	-86	118

Table 2, continued

Composition (Mineral Name)	Spectral Assignment	Peak Position[+] (ppm from TMS)	Reference
$KAl_2[AlSi_3O_{10}]-$ $(OH)_2$ (muscovite)	$Q^3[0 \, Al]$ $Q^3[1 \, Al]$ $Q^3[2 \, Al]$	-89 -85 -81	122
$KLi_2Al[AlSi_3O_{10}]-$ $(F; OH)_2$ (lepidolite)	$Q^3[\, Al]^{[†]}$	-89	118
$(Me_4N)_8Si_8O_{20}$ (tetramethyl ammonium silicate hydrate, TMAS)	Q^{3**}	-99.3	9
$(Et_4N)_8Si_6O_{15}$	Q^3	-90.4	9
$Al_4[Si_4O_{10}](OH)_8$ (kaolinite)	Q^3	-91.5	118
$Al_4[Si_4O_{10}](OH)_4-$ $\cdot 4H_2O$ (endellite)	Q^3	-93.1	118
$Mg_6Si_4O_{10}(OH)_8$ (serpentine)	Q^3	-94.0	118
$\alpha-Na_4Si_4O_{10}$	Q^3	-94.4	118
vermiculite	$Q^3[0 \, Al]$ $Q^3[1 \, Al]$ $Q^3[2 \, Al]$	-92 -88 -83.5	122
SiO_2 (quartz)	Q^4	-107.4	31
SiO_2 (low quartz)	Q^4	-107.4	9
SiO_2 (α-quartz)	Q^4	-107.4	89
SiO_2 (quartz)	Q^4	-108	28
SiO_2 (coesite)	Q^4	-143.4, -152.8	13
SiO_2 (coesite)	Q^4	-108.1, -113.9	144

Table 2, continued

Composition (Mineral Name)	Spectral Assignment	Peak Position[+] (ppm from TMS)	Reference
SiO_2 (low cristobalite)	Q^4	-109.9	9
SiO_2 (cristobalite)	Q^4	-109.9	31
SiO_2 (tridymite)	Q^4	-109.3	13
SiO_2 (tridymite)	Q^4	-111	98
SiO_2	Q^4	-111	63
microcline perthite	$Q^4[1\ Al]$ $Q^4[2\ Al]$ $Q^4[4\ Al]$	-106.0, 101.8 -98.6 -96.0	93
cryptoperthite	$Q^4[1\ Al]$ $Q^4[2\ Al]$?	-103.5, -98.0 -96.0 -92.3	93
oligoclase	$Q^4[1\ Al]$ $Q^4[2\ Al]$ $Q^4[4\ Al]$	-105.3, -97.2 -93.2 -87	93
labradorite	$Q^4[1\ Al]$ $Q^4[2\ Al]$ $Q^4[3\ Al]$ $Q^4[4\ Al]$	-107, -101 -94 -88 -83	93
bytownite	$Q^4[1\ Al]$ $Q^4[2\ Al]$ $Q^4[4\ Al]$	-101 -95 -89, -84	93
$NaAlSi_3O_8$ (low albite)	$Q^4[1\ Al]$ $Q^4[2\ Al]$	-105, -97 -93	28
$NaAlSi_3O_8$ (low albite)	$Q^4[1\ Al]$ $Q^4[2\ Al]$	-96.3, -104.4 -92.2	93
$NaAlSi_3O_8$ (albite)	$Q^4[2\ Al]$ $Q^4[1\ Al]$	-93.0 -97.0, -105.0	17
$(K,Na)AlSi_3O_8$ (microcline)	$Q^4[1\ Al]$ $Q^4[2\ Al]$	-100, -97 -95	28

Table 2, continued

Composition (Mineral Name)	Spectral Assignment	Peak Position[+] (ppm from TMS)	Reference
$CaAl_2Si_2O_8$ (anorthite)	$Q^4[$ $Al]^{+}$	-83, -85, -90	28
$KAlSi_3O_8$ (K-feldspar)	$Q^4[2\ Al]$ $Q^4[1\ Al]$	-95.0 -98.0, -101.0	17
$NaAlSiO_4$	$Q^4[4\ Al]$ $Q^4[3\ Al]$ $Q^4[2\ Al]$	-85.0 -88.5 -92.5	17
$CaAl_2Si_2O_8$	$Q^4[4\ Al]$	-82.5, -84.5, -89.5	17
SiO_2 (stishovite)	Q^6	-191.3	119
SiO_2 (stishovite)	Q^6	-191.1	13
SiO_2 (stishovite)	Q^6	-191.1	
$CaB_2Si_2O_8$ (danburite)	$--^{t}$	-89	28
sandine	$--^{t}$	-101, -97	93
holdstite	$--^{t}$	-108.9, -115.0, -119.4	17
$64.2CaMgSiO_4:35.8SiO_2$		-71	63
$PbSiO_3$ (alamosite)	$--^{tt}$ $--^{tt}$ $--^{tt}$	-84.1 -86.5 -94.3	62

---

*   Interpolated from the spectrum.

+   The chemical shifts are reported to the precision given by the

       individual authors.

t   Not specified.

Table 2, continued

‡   2:1 ratio of line Intensities.

?   Occasionally, spectral assignments were not classified by the
    individual authors.

†† 1:1 ratio of line Intensities.

‡‡ 7 lines: -69.3 ppm (twice the intensity), -73.7 ppm (also twice
    the intensity), -72.0 ppm, -73.0 ppm, -73.9 ppm, -74.2 ppm and
    -74.8 ppm.

** Different spectral assignments by different authors:

    Q^3 versus Q^2 for $(Me_4N)_8Si_8O_{20}$, and Q^2 versus Q^1 for zunyite.

IV.2. Crystalline Silicate Structure

The primary impact of ^{29}Si NMR in solids has been in the deter-
mination of aluminosilicate structures (specifically, the silicon-
aluminum ordering in zeolites). Lippmaa and coworkers[31,32,116,118]
have shown that isotropic [29]Si chemical shifts in solid silicates
and in solutions are generally the same. The main influence on
chemical shift is clearly the degree of condensation of the silicate
tetrahedra. If all other variables are held constant, and the sili-
cate polymerization state is changed, δ([29]Si) will shift 10 to 15 ppm
lower in frequency for the formation of each additional oxygen atom
bridge as shown in Figure 10.[118] In solids the influence of the
cation type and degree of ionization can also been seen. [29]Si
chemical shifts are also capable of distinguishing crystallographic-
ally as well as chemically distinct silicate groups in polycrystal-
line and noncrystalline materials.

IV.2.i. Correlation of δ([29]Si) with Si-O Bonding

Isotropic [29]Si chemical shifts have been correlated with several
general crystalline structural parameters; δ([29]Si) becomes more neg-
ative when the Si-O bondlength decreases,[69,100,124] the total cation
oxygen bond strengths for all the oxygen atoms in the SiO_4 tetrahe-
dra increases,[28] and for an increase in the average Si-O-Si bond
angle.[13,18,72,73,98] In a series of sorosilicates with distinct
$Si_2O_7^{6-}$ anions, it was found that δ([29]Si) can change by as much as
25 ppm depending upon the Si-O-Si bond angle.[74]

Smith and Blackwell[13] have found strong correlations between

Q^0

Q^1 $Q^1(Si-O-Si = 180°)$

Q^2

Q^3

Q^4

-60 -70 -80 -90 -100 -110 -120

$\delta(^{29}Si)$ ppm from TMS
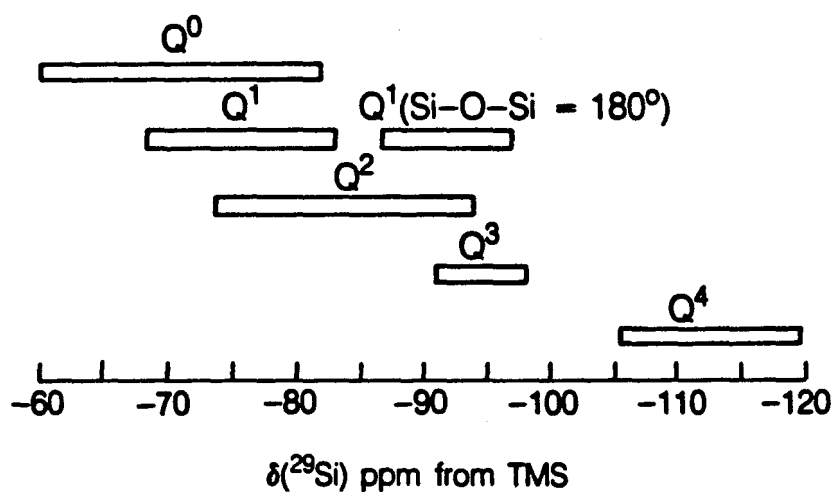
XBL 857-10633

Figure 10: The isotropic ^{29}Si chemical shift ranges for isolated silicate (SiO_4^{4-}) tetrahedra (Q^0), pairs and chain end groups (Q^1), rings and chains (Q^2), chain branching sites and sheet (Q^3), and three dimensional framework (Q^4) silicates. If all other variables are held constant and the silicate polymerization state is allowed to change, then $\delta(^{29}Si)$ will shift ≈ 10 to 15 ppm to lower frequencies for each additional oxygen atom bridge formed.

chemical shift and average Si-O-Si bond length, and the secant of the mean Si-O-Si bond angle, as well as a weak correlation with mean Si-O bond distance. Ramdas and Thomas[18] have confirmed that a quantitative correlation exists between ^{29}Si chemical shifts and Si-O-Si (or Si-O-Al) bond angles in zeolite frameworks. Engelhardt and Radeglia[98] found that different formulations could give slightly different correlations between $\delta(^{29}Si)$ and $\langle\alpha\rangle$, the average Si-O-Si (or Si-O-Al) bond angle. Thomas and coworkers found in general, $140° < \alpha < 160°$. Smith and Blackwell[13] found

$$\text{secant } \langle\alpha\rangle = -3.1571 - 0.017847 \; \delta(^{29}Si) \tag{47}$$

with residuals $\chi^2 = 0.9811$, and $\sigma = 0.0038$. Rearranged,

$$\delta(^{29}Si)^{13} = -48.61 \text{ sec } \langle\alpha\rangle - 168.04 \; . \tag{48}$$

Another investigation found

$$\delta(^{29}Si)^{72} = -0.6192 \langle\alpha\rangle - 18.68 \tag{49}$$

with $\chi^2 = 0.974$. Engelhardt and Radeglia[98] found the best fit to their data was

$$\delta(^{29}Si)^{98} = -247.05 \langle\rho\rangle + 2.19 \tag{50}$$

with $\chi^2 = 0.987$ and

$$\langle\rho\rangle = \cos \langle\alpha\rangle / (\cos \langle\alpha\rangle - 1) \; . \tag{51}$$

A correlation between $\delta(^{29}Si)$ (in ppm) and the mean value of the Si-O bondlength, $\langle d(Si-O)\rangle$ (in nm), valid for all types of silicates

$(Q^n$ units with $0 < n < 4)$, has been found by Grimmer and Radeglia[100]

$$\delta(^{29}Si)^{100} = -2014 + 1.187 \times 10^4 <d(Si-O)> . \qquad (51)$$

For Q^4 units only, Higgens and Woessner[124] derived the empirical relation

$$\delta(^{29}Si)^{124} = -2312 + 1.37 \times 10^4 <d(Si-O)> . \qquad (52)$$

Here, a decreasing mean Si-O bond length corresponds to more negative values of the isotropic silicon-29 chemical shift. In general, Si-O bondlengths influence $\delta(^{29}Si)$ much less than do Si-O-Si bond angles.

Five and six coordinated silicon compounds are rather uncommon. Octahedrally coordinated silicon occurs in a few minerals, stishovite (a high pressure phase of SiO_2) and thaumasite are two examples. The observed ^{29}Si chemical shifts for stishovite and thuamasite are -191.3 ± 0.2 ppm[9,13,119] and -179.5 ppm[15] (relative to TMS). As observed, octahedrally coordinated silicon, $Si(OSi)_6$, produces a substantially different chemical shift (≈ 80 ppm more negative) than tetrahedrally coordinated silicon.

IV.2.ii. Correlation of $\delta(^{29}Si)$ with Cation-Oxygen Bonding

^{29}Si chemical shifts are also dependent upon the cation-oxygen interaction strength.[28] Hence, interpretation of ^{29}Si MAS NMR spectra solely on the basis of chemical shift can lead to erroneous conclusions. An example is found in J.V. Smith et al.,[49] where, without prior knowledge of the continuity of $\delta(^{29}Si)$ across the albite-microcline series, incorrect spectral assignments would result.

Magi et al.[118] investigated the influence of cations and lattice geometry on the ^{29}Si chemical shifts in silicates. Both natural and synthetic mineral samples were compared, whenever possible, and differences in chemical shift were found not to exceed 1 ppm. In general, linewidths could differ by more than an order of magnitude because of homogeneous linebroadening in natural samples by paramagnetic impurities. Cation effects on $\delta(^{29}$Si) were found to parallel the electrostatic bond strengths and electronegativities, and have been interpreted in terms of the covalency of the cation-oxygen (M-O) bonds.[117,118]

IV.2.iii. Chemical Shielding Anisotropy in Crystalline Silicates

One of the most thorough ^{29}Si MAS NMR investigations of natural and synthetic crystalline silicates is presented in article by K.A. Smith et al.[28] Not only were ^{29}Si chemical shifts collected, but chemical shift tensor elements (σ_{11}, σ_{22}, σ_{33}), chemical shift anisotropies ($\Delta\sigma$), and asymmetry parameters (η) were also examined to gain further insight into the local structure of silicates. The framework (Q^4) silicates, hydrous sheet (Q^3) silicates, and hemimorphite all were found to have small CSA's and asymmetry parameters too small to measure. This result implies a relatively symmetric electron distribution around the silicon atoms. The anhydrous sheet (Q^3) silicates (Figure 11) cyclosilicates (Q^2), and a few other minerals have moderate to large CSA's and small η's, this indicates the electron distribution about the silicon atom has essentially axial symmetry. The remaining polymeric structures (most nesosilicates (Q^0), sorosili-
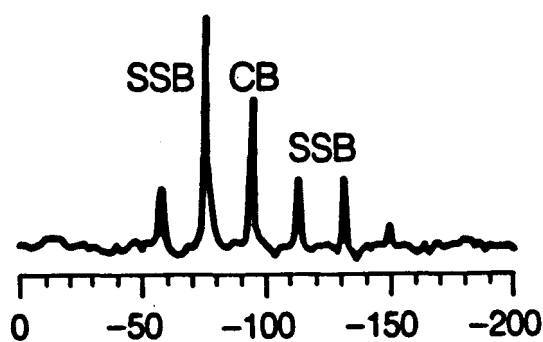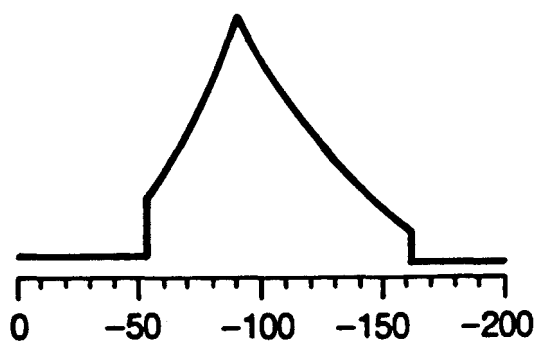
$\delta(^{29}Si)$ ppm from TMS

$Na_2Si_2O_5$ (crystalline)

Figure 11: ^{29}Si chemical shielding anisotropy lineshape of sodium disilicate. (Top) The pattern of a nonaxially symmetric CSA tensor in polycrystalline $Na_2Si_2O_5$ measured directly using standard static NMR techniques (σ_{11} = -52 ppm, σ_{22} = -89 ppm, and σ_{33} = -162 ppm).[28] (Bottom) The CSA tensor can also be determined from the spinning sidebands generated by magic angle spinning (see Appendix A). This figure was taken from reference 121.

cates (Q^1), and chain silicates (Q^2)) have large CSA's and large η's, which indicate a nonsymmetric electron distribution. Grimmer et al.[122] hypothesized that sorosilicates (Q^1 species) have axial symmetry, although Smith et al.[28] have subsequently shown that this is not the general case.

Large concentrations of paramagnetic impurities were found to cause serious difficulties in obtaining NMR spectra.[28] Not only do samples with large amounts of paramagnetism spin slowly and with difficulty, but smaller amounts of impurities cause extensive linebroadening and no signal is observed.

IV.3. Crystalline Aluminosilicate Structure

In the study of Si-Al structure in zeolites and silicate minerals, ^{29}Si MAS NMR gives distinct chemical shifts for $SiO_4{}^{4-}$ tetrahedra depending upon how many $AlO_4{}^{5-}$ tetrahedra they are linked to via oxygen bridges.[10] Aluminum in framework (Q^4) silicates, such as feldspar minerals and synthetic zeolites, cause a systematic deshielding at the ^{29}Si nucleus (a low field, high frequency, or paramagnetic shift) as shown in Figure 12. It was found that isotropic chemical shifts of ^{29}Si and ^{27}Al depend upon the nature of second neighbor cations (third and fourth nearest neighbors). A $\approx$ 5 to 6 ppm high frequency shift will occur with each additional aluminate neighbor tetrahedra. Using ^{29}Si MAS NMR it is possible to quantify the relative amount of the various Q^n [k Al] species (Figure 13).

^{27}Al MAS NMR spectra can also yield quantitative information about the coordination of aluminum in zeolites, since the ^{27}Al chem-

Si(4Al)

Si(3Al)

Si(2Al)

Si(1Al)

Si(0Al)

-80   -90   -100   -110   -120

$\delta(^{29}Si)$ ppm from TMS
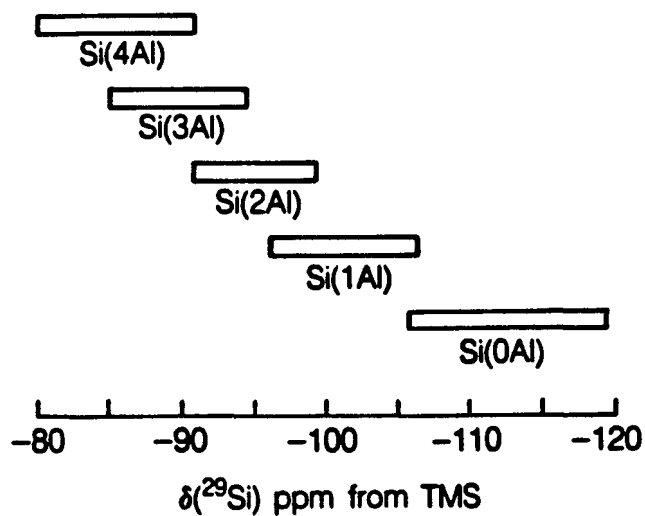
XBL 857-10634

Figure 12: The isotropic ^{29}Si chemical shift ranges for the five

possible Q^4 silicate species with next nearest neighbor

AlO_4^{5-} units. An $\approx$ 5 to 6 ppm shift to higher resonance

frequency will occur with each additional aluminate tetra-

hedra neighbor.

^{29}Si NMR in Na-Y Zeolite
Magic Angle Spinning 3.2 kHz

Si(2)

Si(1)

Si(3)

Si(0)

Si(4)

-82.9 -87.7 -93.2 -99.0 -103.4

Chemical shift (ppm)
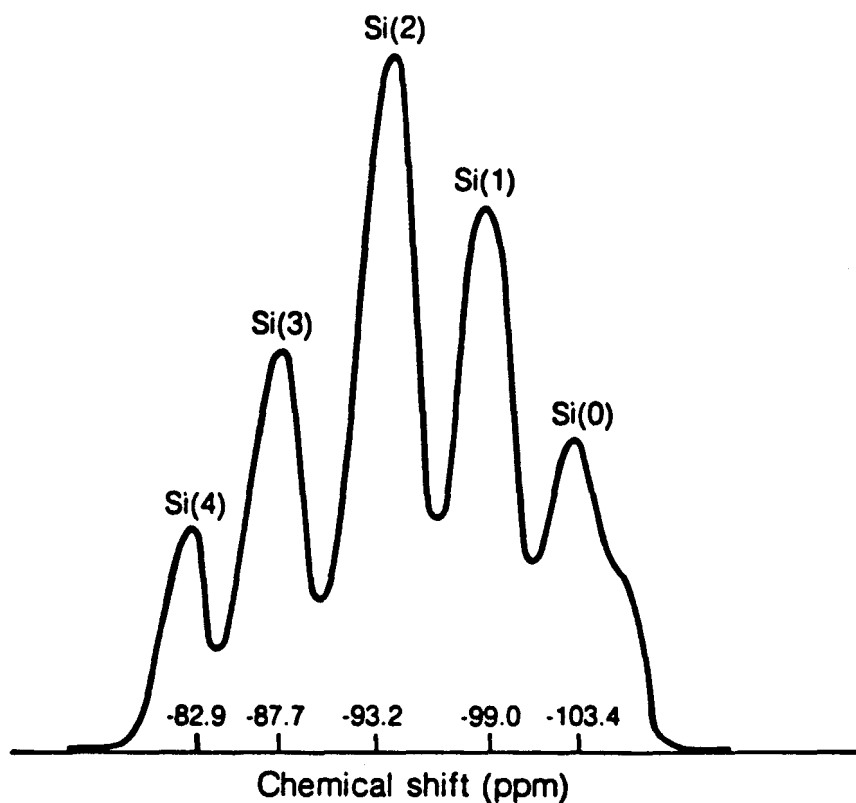
Figure 13: An example of ^{29}Si MAS NMR spectrum of zeolite Na-Y with all five possible aluminum-silicon coordination species present. A systematic $\delta(^{29}$Si) shift of ≈ 5-6 ppm occurs for each additional second coordination sphere aluminum present. The notation Si(0), Si(1), Si(2), Si(3), and Si(4) correspond to Q^4[0 Al], Q^4[1 Al], Q^4[2 Al], Q^4[3 Al], and Q^4[4 Al], respectively.

ical shifts corresponding to 4 and 6 coordination are widely separated from one another. However, acquiring [27]Al data is not only technically more difficult (because it is a quadrupolar nucleus), but analysis of the data is more laborious. Magic angle spinning of a quadrupolar nucleus will only remove the first order interactions, and the isotropic chemical shift may be determined via spectral simulations of the second order pattern (Figure 5). Recently, a quadrupolar echo technique has been combined with spectral "de-Paking" to allow quantitative species distributions to be obtained using non-integral spin (e.g. I=5/2, [27]Al) MAS NMR in amorphous materials.[120]

IV.3.i. Local Silicon-Aluminum Ordering

Analysis of the relative integrated [29]Si peak intensities for partially aluminated zeolites yield tetrahedral Si-Al distributions (determined from the framework Si/Al ratio)--this quantity is not measureable by any other means. Wet chemical analysis does not discriminate between framework Al and occluded, aluminous (nonframework) cations present (as network modifying or charge balancing cations) or residual aluminum impurities (from zeolite dealumination procedures). Also, neither x-ray fluorescence or neutron activation analysis can discriminate between framework and other possible chemically occuring aluminum. The ability of ^{29}Si NMR to differentiate between the various degrees of aluminum substitution for silicon in aluminosilicates has enabled the detailed distribution in the lattice to be determined. Using this technique, the validity of Loewenstein's aluminum avoidance principle[132] has been questioned on several occa-

sions in zeolites.[32,140-142]

Structural information other than the number of neighboring Al atoms may be inferred from the chemical shifts. It has been determined that bond angles and bond lengths[11-13], cation composition and location[17,28] all contribute to the ^{29}Si chemical shift. These influences cause the chemical shift ranges of silicate units to broaden significantly and to usually overlap with the shift range for different aluminosilicate units.

IV.3.ii. Crystallographically Inequivalent Sites

Any phase in which all silicon sites are crystallographically equivalent should exhibit a single ^{29}Si MAS NMR peak. Phases having nonequivalent silicon sites should exhibit as many peaks as there are sites, provided each site is caused by slightly different electronic environments around each type of site. K.A. Smith et al.[28] observed enstatite (Q^2, two sites at -81 and -83 ppm), tremolite (Q^2, also two sites at -88 and -91 ppm), and low albite (Q^4, three sites at -93, -97, and -105 ppm) to exhibit multiple peaks for crystallographically inequivalent sites (as determined by x-ray diffraction). However, kyanite and wollastonite, also show inequivalent x-ray sites but do not show multiple peaks in the corresponding ^{29}Si MAS NMR spectrum.[28]

^{29}Si NMR measures structural information directly, independent of the averaging effects of disorder and psuedosymmetry. The local order observed by NMR techniques may be quite different from the long range, average structures observed by x-ray diffraction.

Stebbins et al.[131] have used this property of ^{29}Si NMR spectroscopy to provide new data on several aspects of the overall crystal structure of common minerals of geologic importance. In particular, crystal structures have been observed by ^{29}Si MAS NMR which are composed of small domains, each of which has a high degree of short range order. If these domains are randomly arranged in the crystal, the materials may exhibit little or no long range order. Stebbins et al.[131] note that "Short range order can have major effects on thermodynamic properties: McConnell[130] has pointed out that entropy changes of many order-disorder phase transitions are often only half the value expected from complete disorder, because of short range effects. For example, in a tectosilicate with Si/Al = 1: a crystal with a truly random arrangement of silicon and aluminum atoms will contain a large number of high energy Al-O-Al bonds, and will behave thermodynamically quite differently from a phase with ordered domains. The energetic differences between the latter phase and a crystal with both long and short range order are due solely to the effects of the domain boundaries."

In the structurally simple minerals of the nepheline group, Stebbins et al.[131] used ^{29}Si NMR spectroscopy to provide new information, which complements x-ray diffraction data, on details of local Si-Al distribution, ordering, and on domain structure. In this mineral family, the Si/Al ratio is close to one, although some solid solution away from ideal stoichiometry occurs. Most compositions have multiple polymorphs, related by two types of phase transitions. A first order transition, involving Si-O-Si or Si-O-Al bond breaking

and reformation, is slow and the high temperature or high pressure phases can be quenched (the structure is preserved). Higher order transitions, involving bond bending and minor displacive structural shifts which lead to lower symmetry forms, are rapid and the high temperature phases are generally unquenchable. Many nepheline family minerals also undergo displacive transitions which produce low symmetry structures while cooling.

The spectra observed by Stebbins et al.[131] of the nepheline family minerals--natural nepheline from a plutonic environment, synthetic kalsilite (the low temperature form of $KAlSiO_4$), pure $NaAlSiO_4$ (nepheline), carnegieite (the high temperature-high pressure phase of nepheline), and orthorhombic (O_1) $KAlSiO_4$--were observed to show little or no evidence of short range aluminum-silicon disorder (Figures 14 and 15). The last three compounds are members of the highest temperature end of the $NaAlSiO_4$-$KAlSiO_4$ system, and might be expected to show such disorder if it could occur. Single crystal x-ray diffraction data has indicated a substantial degree of Al-Si disorder, of uncertain scale, in higher temperature, volcanic nephelines.[138] Based on the relative $Q^n[k\ Al]$ populations, Stebbins et al.[131] characterized and quantitated the disorder present in nepheline minerals. These conclusions are verified by the ^{29}Si NMR spectrum of crystalline volcanic nepheline from Mount Vesubius (Monte Somma Crater), Italy (Figure 16) indicates that some type of disorder is present because Q^4 [0 Al] (or Q^4 [1 Al] species) occur, and the resonance lines are broader than in the lower temperature materials (corresponding to a greater distribution in some structural

Figure 14: (upper) ^{29}Si MAS NMR spectrum of a natural, plutonic crystalline nepheline (16.6% Na_2O, 6.0% K_2O, 0.1% CaO, 33.8% Al_2O_3, 43.3% SiO_2). Four resonance lines were observed, -85.0, -88.4, -91.4, and -101.9 ppm, with relative peak areas of 60%, 21%, 16% and 3%, respectively. The spectral assignments are Q^4[4 Al] surrounded by two sodium atoms and one potassium atom, Q^4[4 Al] surrounded by three sodium atoms and Q^4[3 Al], for the three discrete peaks. The Q^4[3 Al] and the broad resonance are attributed to silicon present in quantities above the stoichiometric amount. (middle) ^{29}Si MAS NMR spectrum of synthetic crystalline nepheline (NaAlSiO$_4$). Three peaks were observed, -82.3, -86.0, and -91.0 ppm, with relative peak areas of 24%, 72%, and 4%, respectively. These peaks have the same assignments as in the upper figure, Q^4[4 Al] with 2 Na atoms and 1 K atom in the unit cell, Q^4[4 Al] with 3 Na atoms in the unit cell, and a Q^4 site associated with the presence of excess silicon. (lower) The ^{29}Si MAS NMR spectrum of crystalline carnegieite (stoichiometric composition) consists of one line located at -82.2 ppm (Q^4[4 Al]) relative to TMS. These spectra are from reference 131.

δ (^{29}Si), ppm from TMS
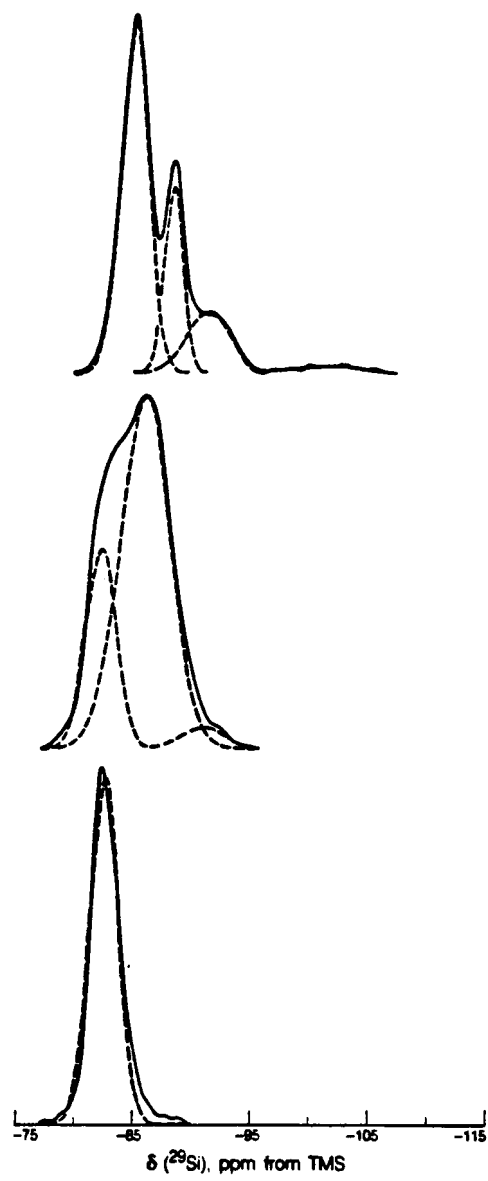
Figure 15: (A) ^{29}Si MAS NMR spectrum of crystalline kalsite

(0.6% Na_2O, 28.5% K_2O, 30.8% Al_2O_3, 40.9% SiO_2) formed

by potassium ion exchange from the synthetic nepheline

sample used in Figure 14. Two resonance lines were

observed at -88.8 and -94.2 ppm (relative peak areas

of 81% and 19%), and assigned to $Q^4[4\ Al]$ and $Q^4[3\ Al]$

sites, respectively. This kalsite sample contains silicon

present in greater than stoichiometric quantities, forming

a solid solution. The $Q^4[3\ Al]$ resonance is attributed

to this excess amount of silicon. (B) The ^{29}Si MAS NMR

spectrum of synthetic, crystalline $O_1-KAlSiO_4$ consists of

three peaks, -84.8, -88.5, and -93.9 ppm, of relative

area 33%, 60%, and 7%, respectively. (C) ^{29}Si MAS NMR

spectrum of crystalline $O_1-KAlSiO_4$, derived from the

natural nepheline sample by K ion exchange. The spectrum

consists of four resonance lines located at -85.4, -88.7,

-92.2, and -97.3 ppm with relative peak areas of 49%,

34%, 15%, and 2%. These spectra are from reference 131.

δ (^{29}Si), ppm from TMS

$$\delta \ (^{29}Si), \ \text{ppm relative to TMS}$$
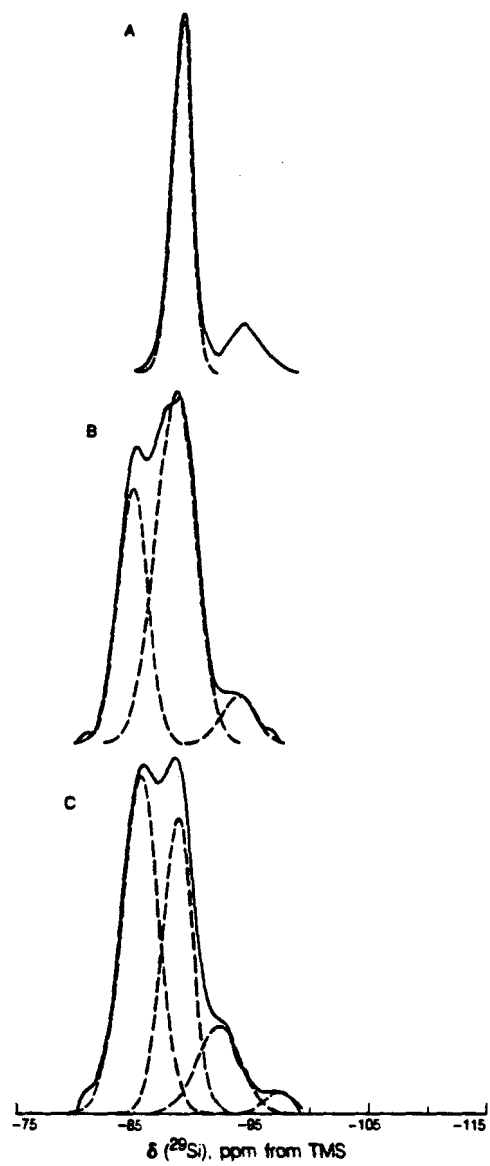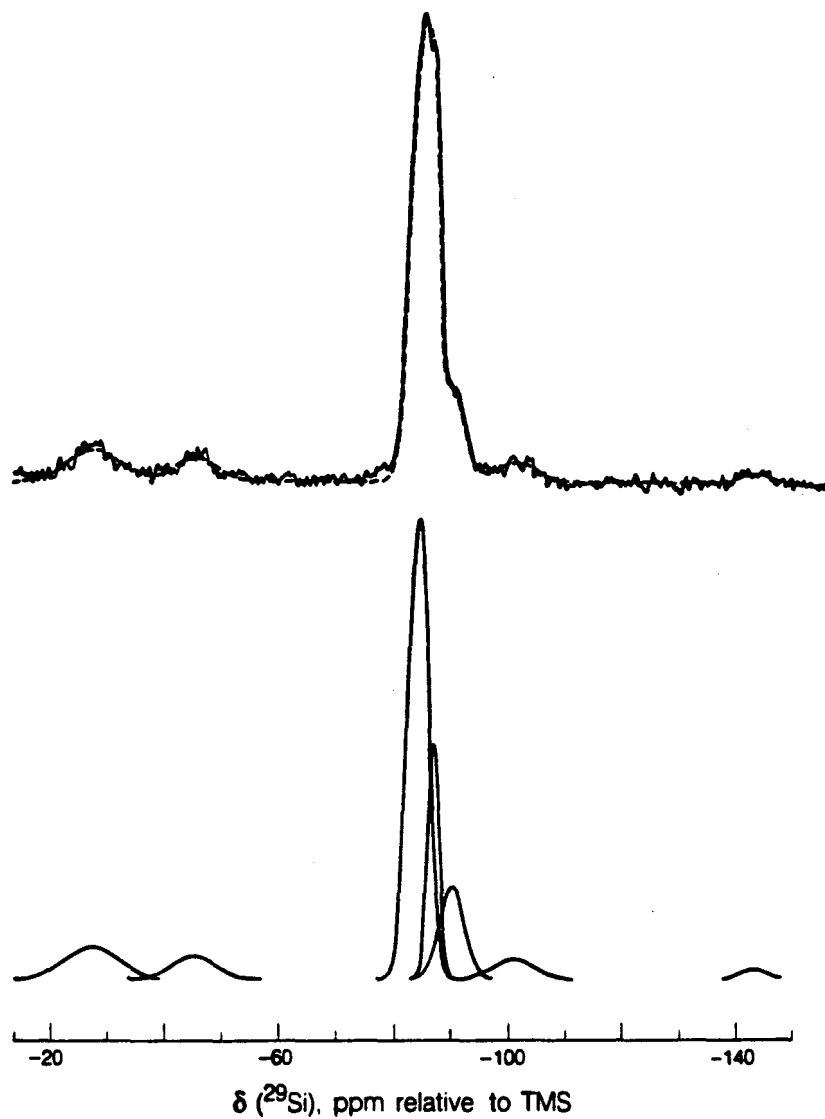
XBL 8511-11749

Figure 16: ^{29}Si MAS NMR spectrum of crystalline volcanic nepheline from the Monte Somma crater on Mount Vesubius, Italy (Smithsonian sample # 47068). This spectrum was taken with 4.2 kHz MAS, a recycle delay of 15 seconds and 3400 averages.

parameter). Hence, ^{29}Si NMR results on the high temperature members of the nepheline family of minerals suggests that the disorder observed by x-ray diffraction is long range only, and results from the mixing of small, but ordered, domains.

Domain models have often been proposed to account for Al-Si and other types of structural disorder in tectosilicates, but characterization of the size of domains and the structure of their boundaries has been difficult. Much information may be obtained about domain boundary orientation and density from those phases which are stable in the beam of a transmission electron microscope,[139] but the details of changes in Al-Si distribution and bond angles at boundaries can not generally be determined by this technique. Using ^{29}Si NMR, several conclusions about such details have been made by Stebbins et al.[131] In crystals with nonstoichiometric amounts of silicon (excess silicon), few or no silicon sites with 0 or 1 aluminum neighbors have been observed. This result indicates that the excess silicon is present primarily along domain boundaries between hexagonal ring layers (stacking faults perpendicular to the c-axis). The density of such boundaries can therefore be estimated, and can be very large, with as many as one boundary per 10 ring layers.[131]

Domain boundaries across which only bond angles change should be detectable by NMR if these sites are abundant enough and the distortions are large enough. No direct evidence of these types of boundaries were observed. Hence, Stebbins et al.[131] concluded this type of domain boundary is less abundant, by at least a factor of 5 to 10, than those which are related to the presence of excess silicon. If

the distorted silicon sites are presumed to have a chemical shift greater than 1-2 ppm from the main NMR peak, then the abundances of such sites can be estimated to be much less than about 1-2% in most samples.

IV.3.iii. Cation Influences

Sanz and Serratosa[122] examined polycrystalline phylloaluminosilicates with ^{29}Si and ^{27}Al MAS NMR. The influence of second neighbor cations located in the three different structural sites (tetrahedral, ocatahedral, and interlayer) were investigated. From ^{29}Si spectra it was observed that Loewenstein's rule is obeyed in these naturally occuring minerals. ^{27}Al spectra, however, gave poor quantitative agreement with mineralogical formulas when experimentally determined Al(tetrahedral)/Al(octahedral) ratios were compared. The observed differences were presumed to be a consequence of second order quadrupole effects.

CHAPTER V:

NMR CONTRIBUTIONS TO THE DETERMINATION OF GLASS SILICATE STRUCTURE

NMR spectroscopy has proven to be extremely sensitive to the local electronic environment of silicon-29 nuclei. In a glass, the same trends are followed[17,35,62,63,89-93] as in aqueous solutions,[96] and in crystalline silicates.[31] Isotropic ^{29}Si chemical shifts systematically move to higher frequencies (less negative values; less shielding of the nucleus by surrounding electrons) with decreasing silica content. Because both silicate speciation and geometric factors (such as Si-O-Si bond angle[73,74,97,99] and Si-O bond lengths[100]) influence ^{29}Si chemical shifts, NMR is potentially useful for characterizing the local structure of silicate glasses. NMR techniques are capable of answering several important issues in glass chemistry. Questions of silicate speciation distribution, the effect of different network modifying cations on the equilibrium expressions presented in Section III.2.ii., and aluminum ordering in glasses can be determined by ^{29}Si solid state NMR methods. Despite the sensitivity of this technique, relatively few NMR experiments have been performed on silicate glasses. [17,35,62,63,85,89-9,115]

In a glass, a much broader range of local silicate environments exists than in the corresponding crystalline material. This range is demonstrated by comparison of crystalline $MgSiO_3$ (enstatite, composed of single chain Q^2 tetrahedra) and enstatite glass (Figure 17). Results from techniques other than NMR have allowed spectroscopists to hypothesize that the difference in peak widths may arise from a range of silicate polymerization species as well as variations in Si-O-Si bond angles and Si-O bond lengths, which are related to the lack of long range order found in glasses.[55,56,60,68,89,91,101]

MgSiO$_3$

δ_{Si} (ppm)
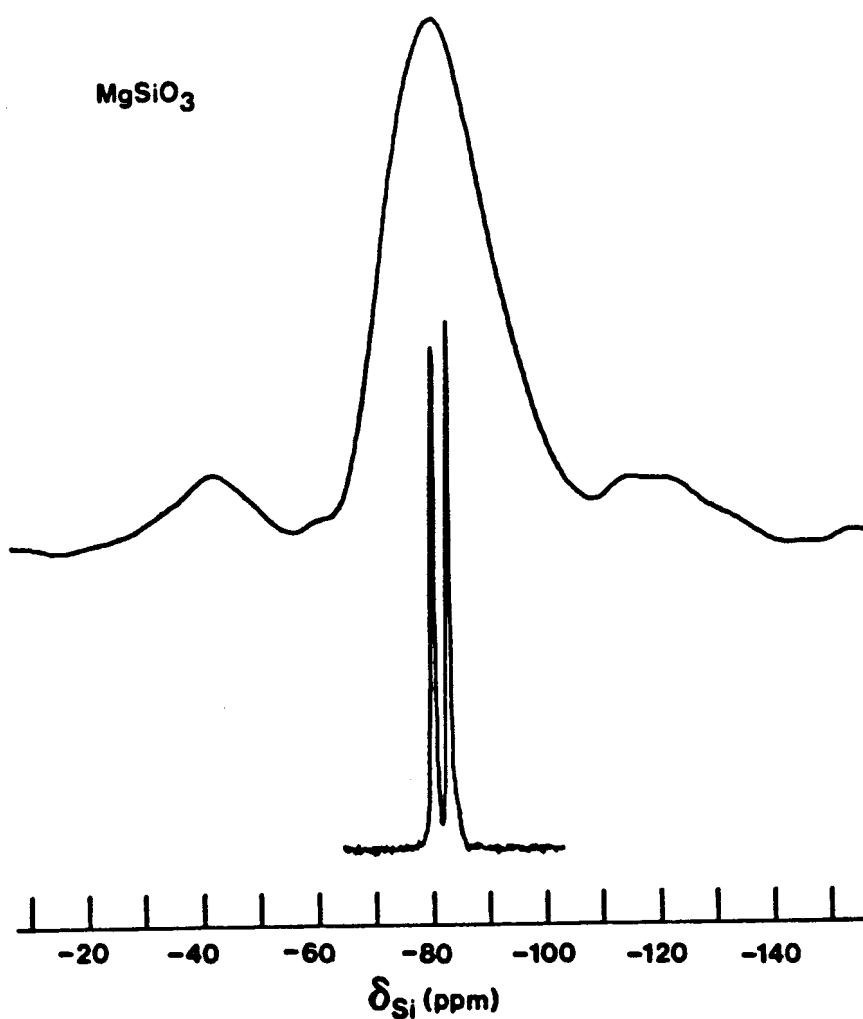
Figure 17: ^{29}Si MAS NMR spectrum of glass (top spectra) and crystal-line (bottom spectrum) MgSiO$_3$ (enstatite). The full width at half maximum (FWHM) for the upper and lower spectra are 22.7 and 0.8 ppm, respectively. The two resonance lines in the lower spectrum correspond to two crystallographically inequivalent silicon sites.[113] The two broad peaks on either side of the main peak (upper spectrum) are spinning sidebands. These spectra are from reference 17.

However, what the ranges of structural parameters (e.g. bond angle, bond length) are and whether or not the distribution is continuous have not been determined. The published [29]Si isotropic chemical shifts and linewidths of various glass silicates are summarized in Table 3.

V.1. Vitreous Silica

On the basis of radial distribution function analysis[51] and Raman spectroscopy,[81] silica glass is believed to consist primarily of interconnected six-membered rings of SiO_4^{4-} tetrahedra. Additional Raman evidence for four-membered rings exists,[82] although every silicon is expected to be in a Q^4 tetrahedron with a distribution of Si-O-Si bond angles. As described in the previous Chapter, ^{29}Si MAS NMR can determine the range and distribution of Si-O-Si bond angles present on the basis of the [29]Si isotropic chemical shift.

Murdoch et al.[17] examined the distribution of Si-O-Si bond angles in SiO_2 glass. The [29]Si spectrum consists of a single, broad (13.2 ppm full width at half maximum or FWHM), symmetric peak with maximum at -110.9 ppm (Figure 18). The [29]Si resonance covers the chemical shift range from -103.8 to -117.0 ppm, which can be converted to a range of Si-O-Si bond angles using the empirical formulas in Section IV.2.I.B. The corresponding range of bond angles ≈ 135° to 160° is in qualitative agreement with the molecular dynamics calculations of Mitra[83] and of Gaskell and Tarrant.[84] The angle corresponding to the NMR peak maximum is 148°, which compares well

Table 3: Isotropic peak positions and linewidths of the ^{29}Si MAS NMR spectra of silicate glasses.

Composition	Compositional <Speciation>	Peak Position (ppm from TMS)	Linewidth FWHM (Hz)	Reference
$CaSiO_3$	Q^1	-81.5	1100[†]	17
$CaMgSi_2O_6$	Q^1	-82.0	1300[†]	17
$MgSiO_3$	Q^1	-81.5	1600[†]	17
$K_2Si_2O_5$	Q^2	-90.5	950[†]	17
$Na_2Si_2O_5$	Q^2	-88.5	940[†]	17
$Li_2Si_2O_5$	Q^2	-90.5	1350[†]	17
$BaSi_2O_5$	Q^2	-92.5	1270[†]	17
$SrSi_2O_5$	Q^2	-92.5	1530[†]	17
$(Na_2O)_{0.6}(SiO_2)_{0.4}$	Q^2	-76	240	89
$(Na_2O)_{0.52}(SiO_2)_{0.48}$	Q^2	-76	390	89
$(Na_2O)_{0.4}(SiO_2)_{0.6}$	Q^3 Q^2	-87 -78	380 380	89
$(Na_2O)_{0.4}(SiO_2)_{0.6}$	Q^2 Q^3	-76.3 -86.5	547 705	115
$(Na_2O)_{0.35}(SiO_2)_{0.65}$	Q^3	-88	390	89
$(Na_2O)_{0.33}(SiO_2)_{0.67}$	Q^3	-90	390	89
$(Na_2O)_{0.25}(SiO_2)_{0.75}$	Q^4 Q^3	-106 -92	400 400	89
$(Na_2O)_{0.15}(SiO_2)_{0.85}$	Q^4 Q^3	-108 -94	500 500	89
$(Li_2O)_{0.4}(SiO_2)_{0.6}$	Q^3 Q^2	-88 -80	500 500	89
$(CaO)_{0.4}(SiO_2)_{0.6}$	$-$[††]	-85.8	1430	115

Table 3, continued

Composition	Compositional <Speciation>	Peak Position (ppm from TMS)	Linewidth FWHM (Hz)	Reference
$(Li_2O)_{0.35}(SiO_2)_{0.65}$	$-^{\dagger\dagger}$	$-96^{\dagger}$	asymmetric††	91
$(Li_2O)_{0.33}(SiO_2)_{0.67}$	Q^3	$-91^{\ddagger\ddagger}$	520	89
$(Li_2O)_{0.26}(SiO_2)_{0.74}$	Q^3 Q^4	-96^{*} -108^{*}	$---^{\dagger\dagger}$ $---^{\dagger\dagger}$	91
$(Li_2O)_{0.25}(SiO_2)_{0.75}$	Q^4 Q^3	$-107^{\ddagger}$ -91	500 500	89
$(Li_2O)_{.175}(SiO_2)_{.825}$	Q^3 Q^4	-92^{*} -107^{*}	$---^{\dagger\dagger}$ $---^{\dagger\dagger}$	91
$(Li_2O)_{0.15}(SiO_2)_{0.85}$	Q^4 Q^3	-108 -92	500 500	89
$Na_2Si_4O_9$	Q^3 Q^4	-92.0 -104.9	856 820	115
$K_2Si_4O_9$	Q^3 Q^4	-94.2 -105.5	849 690	115
SiO_2 (cristobalite)	Q^4	-110.9	$1530^{\dagger}$	17
SiO_2	Q^4	-109^{*}	1500^{*}	85
$KAlSi_3O_8$ (K-feldspar)	Q^4	-99	$1250^{\dagger}$	17
$NaAlSi_3O_8$ (albite)	Q^4	-97.8	$1300^{\dagger}$	17
$NaAlSi_3O_8$ (albite)	Q^4	-98	$---^{\dagger\dagger}$	93
$NaAlSi_2O_6$	Q^4	-92.8	$1320^{\dagger}$	17
$NaAlSiO_4$	Q^4 [4 Al]	-86.0	$960^{\dagger}$	17
$CaAl_2Si_{12}O_{28}$	Q^4	-107.1	$1390^{\dagger}$	17
$CaAl_2Si_6O_{16}$ (anorthite)	Q^4	-101.0	$1600^{\dagger}$	17

Table 3, continued

Composition	Compositional <Speciation>	Peak Position (ppm from TMS)	Linewidth FWHM (Hz)	Reference
$CaAl_2Si_6O_{16}$ (anorthite)	Q^4	-870	--[tt]	93
$CaAl_2Si_4O_{12}$	Q^4	-95.6	1530[t]	17
$CaAl_2Si_2O_8$	Q^4 (4 Al)	-86.5	1230[t]	17
$CaAl_2SiO_6$	Q^4	-82.3	1000[t]	17
$PbSiO_3$	-[tt]	-85.2	720	62
Pb_2SiO_4	-[tt]	-80	---[tt]	62
Pb_4SiO_6	-[tt]	-76	---[tt]	62

---

[t]   Integrated linewidths (calculated as the area under a center peak divided by its height), are a more sensitive measure of variations in peak shape than the full width at half maximum, particularly with the occurence of small shoulders.

[tt]   Not specified.

[*]   Interpolated from the spectrum.

[‡]   This peak is actually a shoulder.

[‡‡]   A small Q^4 shoulder was also observed.
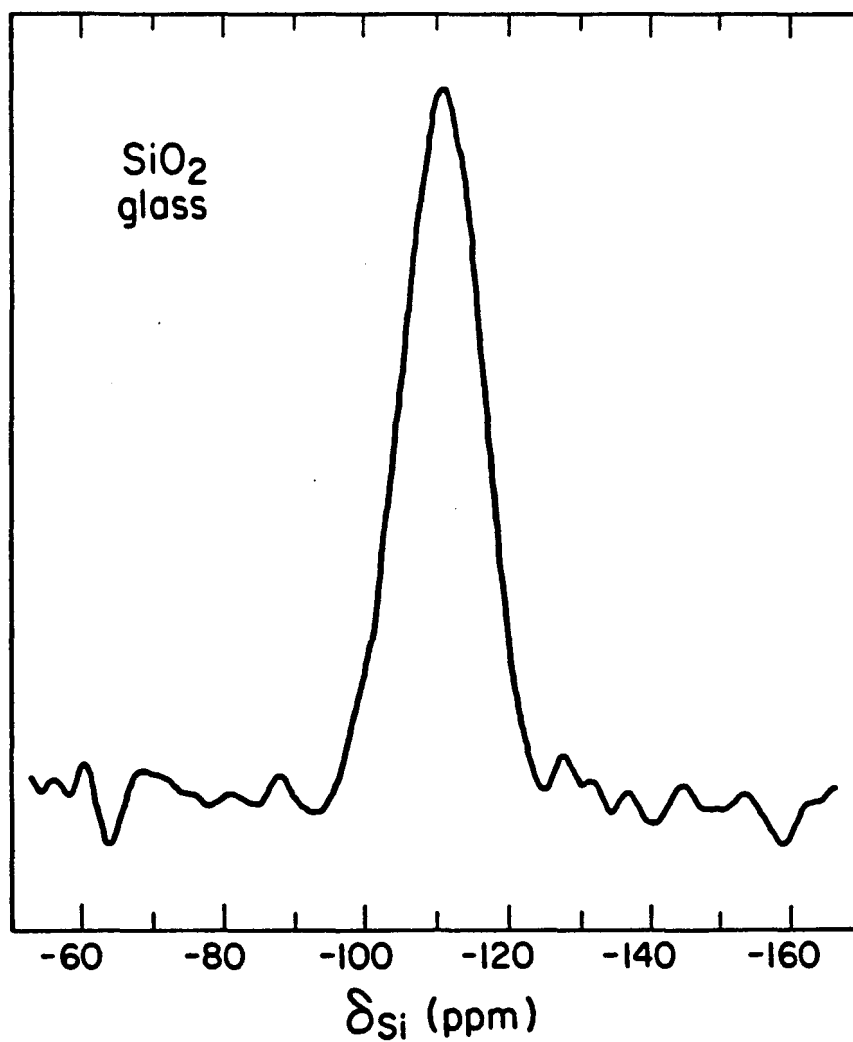
Figure 18: ^{29}Si MAS NMR spectrum of silica glass, obtained by averaging 433 free induction decays. The signal to noise ratio is relatively poor because a long silicon spin lattice relaxation time (T_1) limited the rate at which successive free induction decays could be collected. Radiofrequency pulses with a flip angle of ≈ 15° degrees were spaced at 6 minute intervals.

with the mean Si-0-Si bond angle derived from radial distribution functions (150°)[51] as well as the molecular dynamics value (153°).[83]

Dupree and Pettifer[85] have presented a detailed analysis of the Si-0-Si bond angle distribution associated with the ^{29}Si MAS spectrum of vitreous silica. The ^{29}Si NMR peak maximum at -109 ppm, corresponds to an average angle of 145.5°. One asymmetric line was observed, the steeper slope being on the more negative chemical shift side. The lineshape is presumed to arise from a distribution of inter-tetrahedral angles. The best fit range of bond angles is 140° to 155°, with roughly equal probability.

V.2. Silicate Glasses

Isotropic silicon chemical shifts have been used to investigate the range of silicon environments in glasses. The effects of alkali and alkaline earth cations on the network polymerization structure of binary glasses[17,62,63,89,91,92,115] is reviewed in this Chapter. Also, a critical overview is given of the interpretation limits for the ^{29}Si MAS NMR on glass structure.[115]

Schramm et al.[91] have observed asymmetric and two peaked ^{29}Si NMR spectra of several lithium silicate glasses with nonintegral mean Q^n number. Interpretation of the spectra was based on modelling the equilibrium in Equation (45). Each of the observed glass ^{29}Si MAS spectra was deconvoluted into Gaussian lineshapes corresponding to the five possible local silicate polymerization states (Q^0, Q^1, Q^2, Q^3, and Q^4) with peak positions chosen by comparison with crystalline spectra. From the deconvoluted spectra, distributions of the

polymerization states of lithium silicate glasses were derived and a linear relationship which describes the dependence of Q^n composition on mole percent Li_2O was obtained. Unfortunately, not only are the results of the deconvolutions model dependent, but the analysis has included spectra of glasses which are not optically clear. The presence of optical sized particles, which scatter light, indicate that some of the glasses investigated are not homogeneous and single phased.

In a ^{29}Si MAS NMR investigation of Na_2O-Si_2O and Li_2O-Si_2O binary glasses, Grimmer et al.[89] concluded that a statistical distribution of Q^n units does not exist. That is, in glasses of composition Q^n where n is an integer, only one ^{29}Si peak was observed, hence only one type of species exists---the one found in the crystalline form. In glasses of composition where n is a noninteger, two peaks were observed and it was concluded that only two types of silicate units are present---the neighboring integer composition Q^n units. The authors[89] maintain that the breadth of the glass peak arises from distorted SiO_4 units (of nontetrahedral symmetry) which are statistically distributed around a well defined average geometry. Because crystalline silicates and their corresponding glasses are observed to have very similar isotropic ^{29}Si chemical shifts, the authors assumed that the average SiO_4^{4-} geometry present in glasses is very similar or identical to the known geometry of the silicate units in the corresponding crystalline alkali silicates.[89] However, in this investigation glass preparation techniques were such that two glass phases from metastable liquid-liquid immiscibility possibly

resulted in the high silica content glasses.

Kirkpatrick et al.[63,92] used ^{29}Si and ^{17}O MAS NMR to examine low silica composition glasses in the ternary system CaO-MgO-SiO. Only abstracts in conference proceedings have been published to date by the Oldfield-Kirkpatrick group, although it is known that a substantial amount of NMR work on silicate glasses has been accomplished in the past three years. Broad, single peak ^{29}Si spectra were obtained, and the linewidth was attributed to a range of silicate structural sites in the glasses. ^{17}O MAS NMR glass spectra were similar to those of the corresponding crystalline material, with a small amount of broadening.

Lippmaa et al.[62] observed the ^{29}Si MAS NMR spectra of three different composition lead silicate glasses. Each spectrum consisted of one fairly broad peak. As the lead content of the glass is increased, the isotropic chemical shift moves to higher frequency (the nucleus is less shielded). The influence of thermal treatment was also investigated. It was found that $PbSiO_3$ glass crystallizes to yield a structure identical to that of the mineral alamosite. The ^{29}Si NMR spectrum of alamosite consists of three lines, in agreement with the x-ray diffraction results.

V.3. Speciation in Binary Alkali Silicate Glasses

One motivation for additional study of silicate glasses of simple composition is to carefully define the amount of information available in ^{29}Si spectra. This cautious approach is necessary to evaluate whether the various structural models can be distinguished.

The second motivation is more practical: because glass structure is very often the only basis for hypotheses about liquid silicate structure, it is essential that glasses chosen for analysis be as representative of the liquid state as possible. In particular, it is desirable to study glasses which are physically single phases, as is a homogeneous liquid. In several of the studies mentioned in section V.2., some of the glasses investigated showed signs of not being single phased.

Opalescence is an indication of the presence of two glass phases which resulted from metastable liquid-liquid immiscibility. Phase separation is promoted by annealing of $Na_2O:SiO_2$ and $Li_2O:SiO_2$ glasses which have high silica contents. All of the glasses described in depth in this thesis were quenched rapidly, and are optically clear. The absence of optical scattering implies that any separated phase has few domains larger than several hundred nm. Although in general, a good correlation has been observed[79,95] between the lack of observed optical scattering and the absence of smaller domains (detectable only by small angle x-ray scattering), this relationship may not be true in every case. In the potassium system ($K_2O:SiO_2$), abundant evidence exists that phase separation does not occur in glasses, even with annealing.[95]

In glasses of low silica content, the nucleation and growth of crystals of submicroscopic dimensions may also be a problem. Powder x-ray diffraction measurements ensured that the glasses used in the present investigation were free of crystals down to the sensitivity limit of this technique, or 1-2 nm (in silicates, this is usually one

to five unit cell lengths).

Binary alkali silicate single phase glasses of integral and non-integral mean Q^n number were synthesized in approximately one gram batches from reagent grade oxides and carbonates.[115] A 95% isotopically enriched ^{29}Si sample of glass $Na_2{}^{29}Si_4O_9$ (average speciation $Q^{3.5}$) was prepared to obtain high signal-to-noise spectra. The oxide-carbonate mixtures were heated in a sealed platinum tube in a Deltech furnace to about 100^oC above their liquidus temperatures. Sample tubes were water quenched to retain single phase glasses. To create more homogeneous samples, the glasses were subsequently ground, remelted, and requenched.

V.3.1. Glasses of Integral Mean Q^n Composition

Murdoch et al.[17] specified the degree of polymerization in di-silicate and metasilicate glasses using ^{29}Si MAS NMR. For the stoichiometric glasses (Q^n, with n an integer) observed, the ^{29}Si MAS NMR spectrum yielded only one peak, with no distinctive separation for each Q^n species. Metasilicate glasses $CaSiO_3$, $CaMgSi_2O_6$, $MgSiO_3$ (Figure 19), and disilicate glasses $K_2Si_2O_5$, $Na_2Si_2O_5$, $Li_2Si_2O_5$ (Figure 20), $BaSi_2O_5$, $SrSi_2O_5$ (Figure 21) were observed. Only $Li_2Si_2O_5$ and $Na_2Si_2O_5$ have noticeable shoulders. The position of the peak maximum indicates that the primary silicate species present in the glass is the same one found in the corresponding crystalline material ---Q^3 in disilicates and Q^2 in metasilicates. This finding is consistent with previous ^{29}Si MAS NMR results,[63] with Raman spectroscopy work,[54,55,57] with a radial distribution function measurement on

MgSiO₃

CaMgSi₂O₆

CaSiO₃

δ_{Si} (ppm)
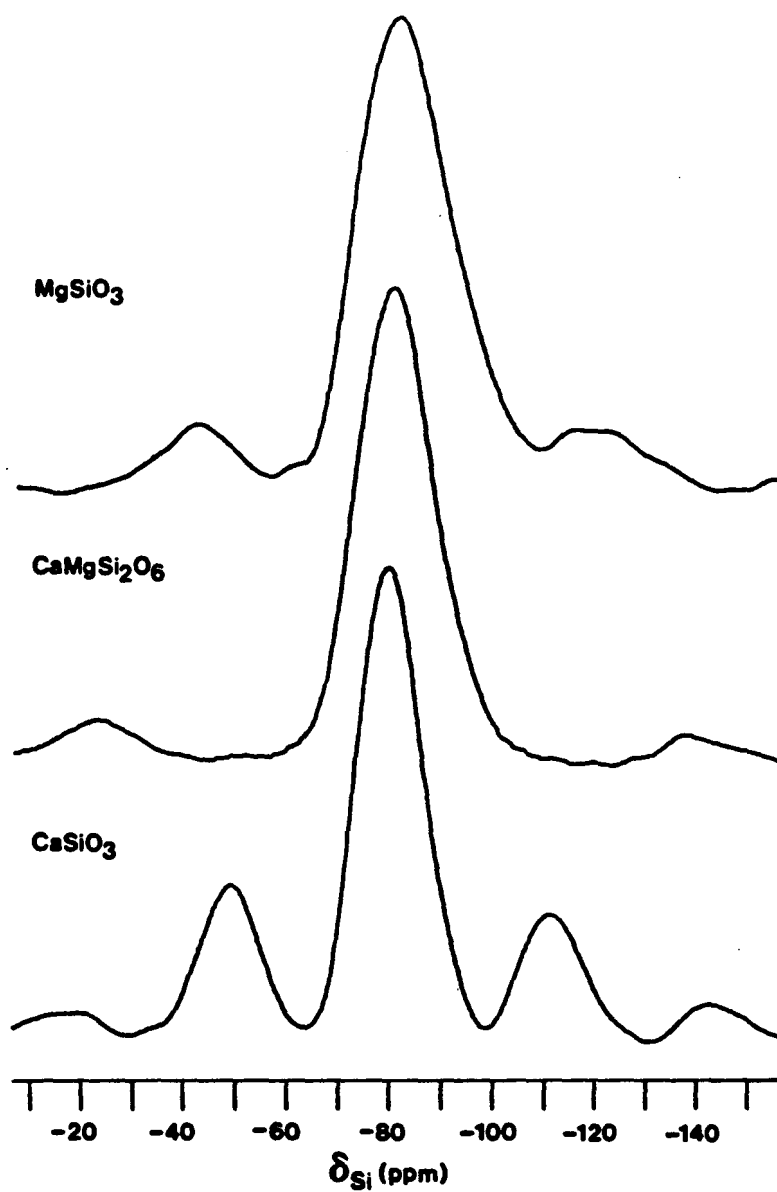
XBL 8312-2503

Figure 19: ^{29}Si MAS NMR spectra of alkaline earth metasilicate (CaSiO₃, CaMgSi₂O₆, and MgSiO₃) glasses. Peak heights are normalized in this and subsequent figures. These spectra are from reference 17.
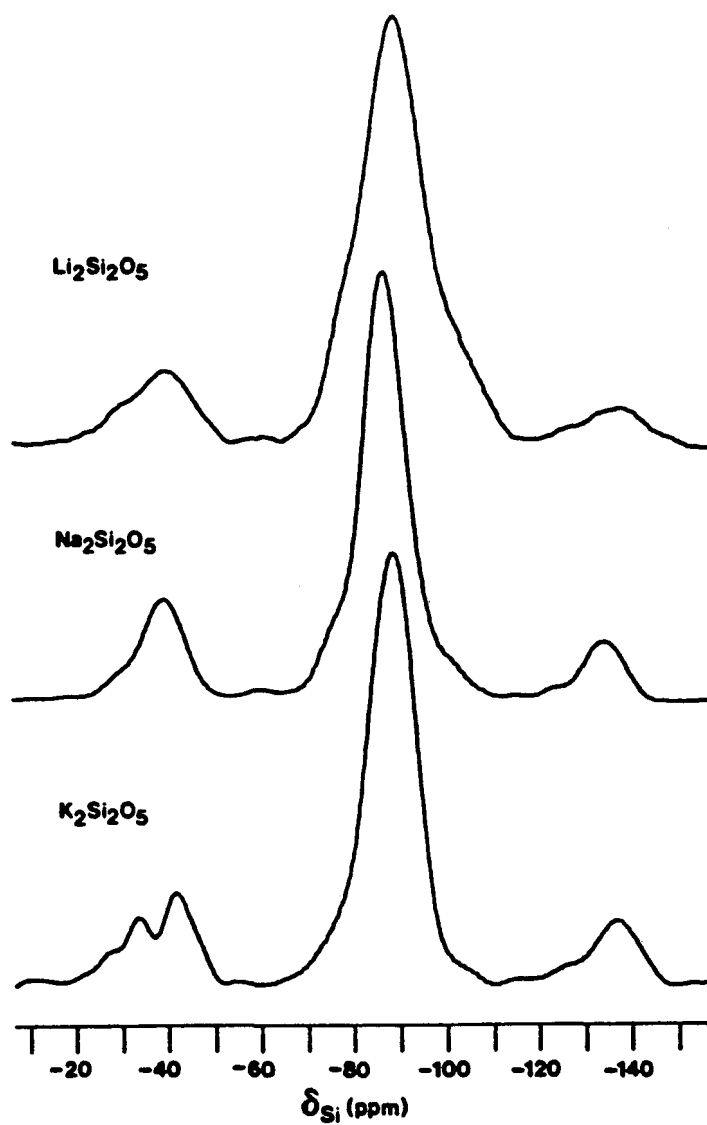
Figure 20: ^{29}Si MAS NMR spectra of alkali metal disilicate ($K_2Si_2O_5$, $Na_2Si_2O_5$, and $Li_2Si_2O_5$) glasses. The dip in the left spinning sideband of potassium disilicate is an artifact. These spectra are from reference 17.

SrSi$_2$O$_5$

BaSi$_2$O$_5$

-20   -40   -60   -80   -100   -120   -140

δ_{Si} (ppm)
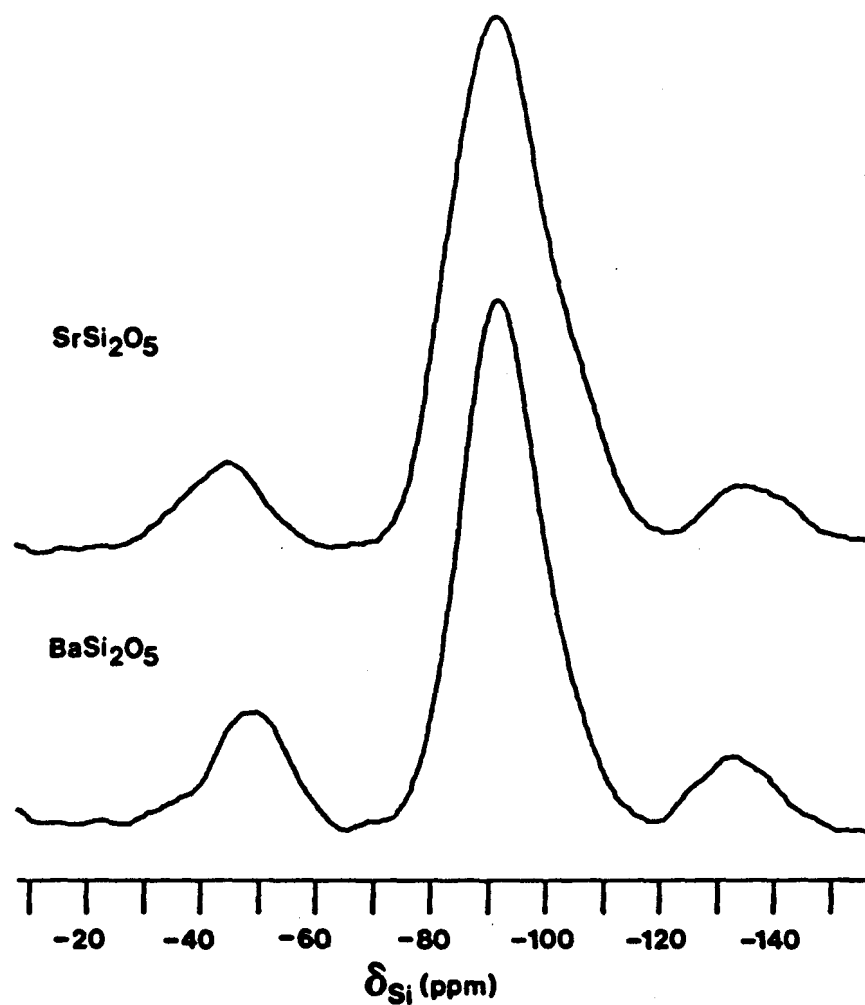
XBL 8312-2502

Figure 21: ^{29}Si MAS NMR spectra of alkaline earth disilicate

(BaSi$_2$O$_5$ and SrSi$_2$O$_5$) glasses. These spectra are from

reference 17.

$Na_2Si_2O_5$ glass[77] and with the results of Si K-β x-ray spectroscopy.[50]

The chemical shift range encompassed by the glass silicon resonance increases as the size of the cation decreases and as charge increases.[17] This trend suggests that the larger the ionic potential (charge/radius) of a network modifying cation is, the more the cation will disrupt a silicate structure. The equilibrium in Equation (45) is shifted to the right, localizing the negative charge associated with nonbridging oxygen atoms and creating a broader range of silicate species. This result again agrees with Raman spectroscopic conclusions,[54-57] and the interpretation of silicate liquid speciation is consistent with work on the effect of cation substitution on chemical activity of SiO_2 in binary melts.[78] A complementary description, in accord with CNDO/2 molecular orbital calculations[50] is that smaller cations prefer to cluster together. An example is that the creation of silicate units with multiple M-O linkages tends to be energetically favorable for M = Li^+, but not so for M = K^+.

For both disilicates and metasilicates, a trend toward a wider Q^n distribution is observed in glasses with smaller, more highly charged cations.[17] This trend is apparent from a graph of integrated linewidth (area under peak divided by peak height) as a function of ionic potential (or polarizing power, i.e. ionic charge divided by the ionic radius in nm) of the network modifying cation (Figure 22). Several other cation properties such as ionization potential, field strength, and molecular orbital mixing coefficient could have been used to obtain the same qualitative result.[17]

A difference in linewidth exists between $CaSiO_3$ (much narrower)
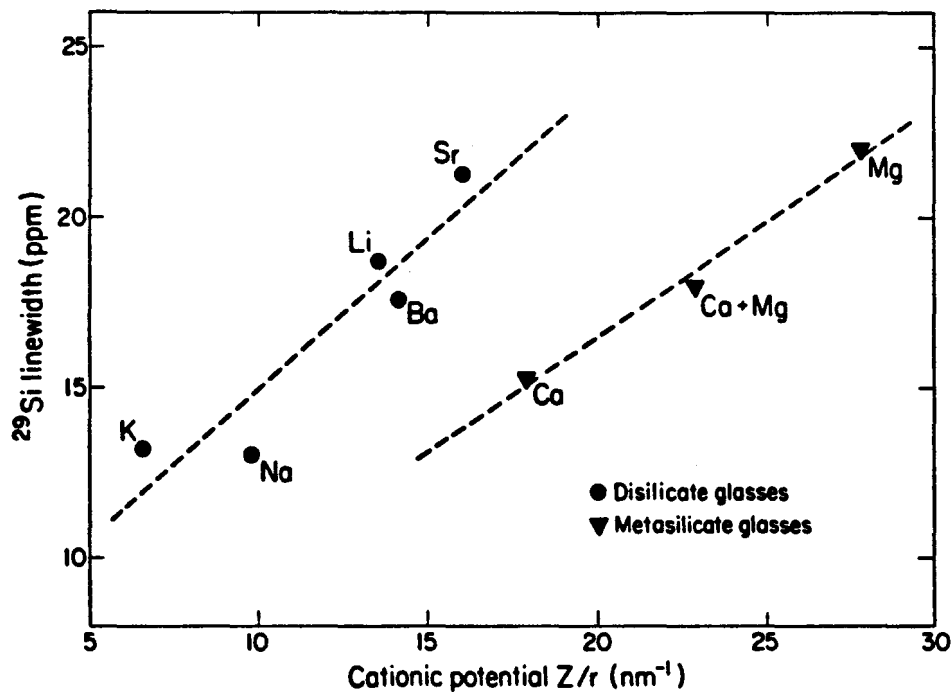
Figure 22: Integrated linewidths (peak area/height) of disilicate and metasilicate glasses as a function of the ionic potential (charge/ radius) of the network modifying cation. Ionic radii are those of Shannon and Prewitt.[114] For $CaMgSi_2O_6$, the cationic potential was assumed to be the average of the values for Ca and Mg. This figure is from reference 17.

and $SrSi_2O_5$ (broader) glass. This difference arises from the separation in ^{29}Si chemical shift between Q^4 and Q^3 species, this separation is larger than between Q^3 and Q^2, Q^2 and Q^1, or Q^1 and Q^0. Due to the higher overall level of polymerization in the disilicate, there are generally more Q^4 tetrahedra in disilicate glasses than in metasilicate glasses. The higher concentration of Q^4 silicons gives rise to extra broadening of the disilicate MAS resonances. The differences in disilicate and metasilicate glass linewidths may additionally reflect a larger equilibrium constant for Equation (42) than for Equations (43) or (44).

The pronounced shoulders in $Li_2Si_2O_5$ glass imply the existence of more clearly defined Q^n units than in other glass samples. A deconvolution of the lineshape into three Gaussians lineshapes yield peaks at -78.5, -90.5 and -105 ppm with relative intensities of 8:81:11, for silicate units Q^2, Q^3, and Q^4 respectively. These three peaks could also come from regions of higher and lower lithium content.[79]

The glass $Na_2Si_2O_5$ spectrum was also deconvoluted into 3 gaussian peaks at -77, -88.5, and -99.5 ppm (Q^2, Q^3, and Q^4 units) with relative intensities of 8:84:8. A small bump at -62.5 ppm is possibly a real feature and could be ascribed to isolated SiO_4^{4-} tetrahedra (Q^0 units). Its intensity is 0.4% of the main peak and may be present in the $Li_2Si_2O_5$ glass spectrum as well.

In most of the spectra observed by Murdoch et al.,[17] the glass peak maximum is within a few ppm of the corresponding crystalline peak(s). One exception is $CaSiO_3$, for which the glass maximum appears

at -81.5 ppm, whereas the spectrum of crystalline $CaSiO_3$ features one fairly broad peak at -88.5 ppm. In comparison, peak maxima for crystalline and glassy samples of both $CaMgSi_2O_6$ and $MgSiO_3$ lie between -81 and -84 ppm. This difference suggests that crystalline $CaSiO_3$ with its peculiar silicate chain repeat length of three tetrahedral units,[80] relaxes in a glass to chain structure more like that of the pyroxenes $CaMgSiO_3$ and $MgSiO_3$.[17]

V.3.ii. Glasses of Non-Integral Mean Q^n Composition

In 95% enriched $Na_2Si_4O_9$ glass, two broad, overlapping ^{29}Si lines are observed (Figure 23). These peaks are ascribed to a Q^3 and a Q^4 silicate species on the basis of ^{29}Si isotropic chemical shifts similar to those of crystalline sodium silicates $Na_2Si_2O_5$ (-95 ppm) and SiO_2 (-108 ppm), respectively. Many sidebands (2-5) are observed for the Q^3 silicate species even at moderate spinning speeds (1.1-2.4 kHz), hence it can be concluded that this silicon site is asymmetric (as in crystalline $Na_2Si_2O_5$). However, the Q^4 silicon site is fairly symmetric, as indicated by the lack of observable spinning sidebands.[14,23,24] Highly symmetric Q^4 sites are generally observed in crystalline silicates.[28] The room temperature ^{29}Si MAS NMR spectrum of the isotopically enriched $Na_2Si_4O_9$ glass (-92.0, -104.5 ppm for Q^3 and Q^4 sites, respectively) is identical to that obtained with the unenriched sample, and is similar to the melt spectrum. (Static ^{29}Si NMR spectra of molten sodium tetrasilicate at temperatures near T_g contain two resonance lines.[106-109])

To ascertain whether the two resonance lines observed in sodium

Figure 23: ^{29}Si NMR spectra of 95% isotopically enriched $Na_2Si_4O_9$

glass. (Top) A nonspinning (static) spectrum obtained

using the sequences 90_x - τ_y - sample and 90_{-x} - τ -

sample, with alternating addition and subtraction of the

subsequent FIDs. The optimum value for the spin locking

time, τ_y, was found to be 20 μseconds. 600 averages and

a recycle delay time of 60 seconds were used to obtain

this spectrum. (Middle) MAS spectrum at a moderate (2.42

kHz) spinning speed. Superposed on the spectrum (solid

line) is the fit spectrum (dashed lines). The individual

peak deconvolutions are shown immediately beneath the or-

iginal and fit spectrum. The estimated error of decon-

volution is a maximum of 5% for peak location and height,

and 20% for FWHM intensity and hence also 20% for peak

area. Central peak widths agree with spinning sideband

values. A "rolling baseline" could not be removed with

various spectral manipulations, therefore the outer spin-

ning sidebands have inaccurate deconvolutions. (Bottom)

MAS spectrum obtained at a slower spinning speed (1.41

kHz). The spectral deconvolution is as previously des-

cribed. The spectra were averaged 20 times, using a 90°

pulse length of 9.0 μsec, and a repeat time of 60 sec.

The Argonne National Laboratory spectral deconvo-

lution subroutine va02a was used to fit the spectra.

Gaussian lineshapes were chosen on the assumption that

in these samples, the broad spectral lines are due to a
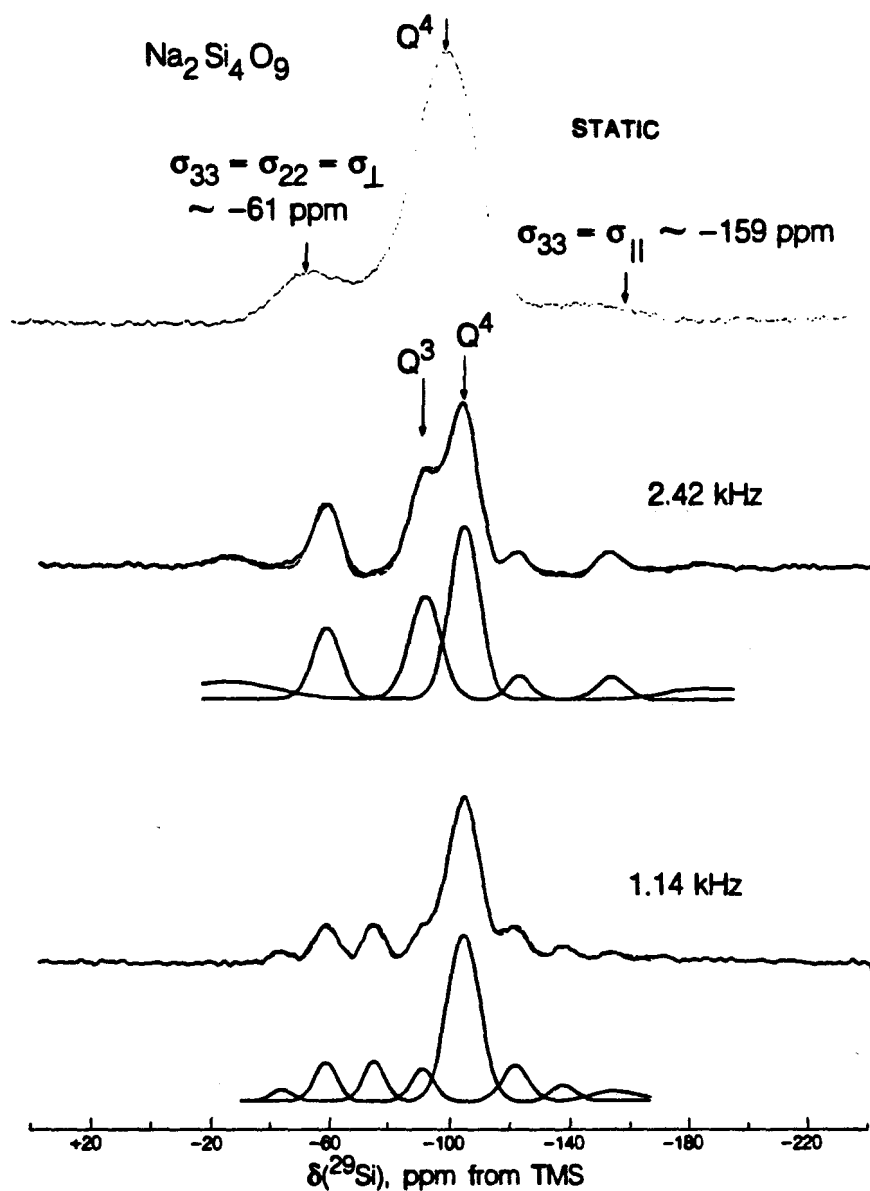
Figure 23, continued

statistical distribution of some structural parameter. The number of peaks for a given fit was chosen as the number of obvious spectral features (such as clearly resolved peaks and shoulders). To determine the mathematical stability of a fit, several deconvolutions were obtained using different initial conditions (peak location, width, and relative intensity).

tetrasilicate glass are caused by two species in a homogeneous, single phase glass and not to suboptical scale phase separation, experiments must be performed which are able to differentiate between randomly mixed and clustered Q^3 and Q^4 silicate species (although clustering does not necessarily imply the existance of a thermodynamic phase boundary). In the binary $Na_2O:SiO_2$ system, the shape and position of the metastable solvus are such that if phase separation did occur, only a small portion of the Q^4 rich phase could be present in the compositions studied. However, the deconvoluted areas of the two resonances are approximately the same, indicating that equal quantities of Q^3-type and Q^4-type silicate polymerization species are present.

Utilizing FID sampling synchronized with the rotor period,[110] two dimensional COSY and NOESY type[107-109] NMR experiments did not yield cross peaks (indicating no coherence transfer). This result is inconclusive because Si-Si connectivity is very weak in silicates due to large ^{29}Si-^{29}Si internuclear distances (even in a 95% isotopically enriched sample) and the low gyromagnetic moment possessed by ^{29}Si. More success in studying coherence transfer from one site to another could possibly be had by utilizing an approach such as magic angle hopping (which allows evolution of the spin system under the high field dipolar Hamiltonian),[111] or multiple pulse excitation of dipolar coherence during the evolution period while under magic angle spinning conditions.[112]

A relaxation time approach has also been taken. In amorphous samples where distinct speciation domains may exist, spin coherence

between the domains may not be exchanged efficiently, and the spectral lines would exhibit different relaxation times. If the lines have the same relaxation times, then spin diffusion occurs and the two species may be mixed on a molecular level. On the basis of varying the pulse recycle delay, both peaks in the ^{29}Si MAS NMR spectrum of $Na_2{}^{29}Si_4O_9$ were found to have approximately the same spin lattice relaxation time (T_1) of ≈ 25 ± 1 seconds. However, the relaxation time data are better fit using two exponential functions of temperature. A short T_1 component, with an estimated 30% population of the spins, is present in the enriched glass. The short and long components of relaxation are very similar for both the Q^3 and Q^4 species, 1 and 4 seconds respectively (these are not statistically different) for the short T_1 and ≈ 25 seconds for the long T_1. Both peaks in the ^{29}Si MAS NMR spectrum of the unenriched $Na_2Si_4O_9$ also have statistically the same value of T_1 (27 ± 7 sec and 35 ± 10, respectively), in accord with the isotopically enriched material. The static (nonspinning) value of T_1 was also measured for the enriched sodium tetrasilicate glass: the Q^4 species has a T_1 of ≈ 26 sec and the Q^3 species yielded T_1 ≈ 14 sec. Unfortunately, this data does not reveal the relative separation of the two silicate species. Further investigation is necessary in this single phase $Na_2Si_4O_9$ glass.

A further check on the role of phase separation is the spectrum of $K_2Si_4O_9$ glass (Figure 24). Phase separation of glasses in the binary system $K_2O:SiO_2$ is not known to occur and crystallization is very slow. The ^{29}Si MAS NMR spectrum again consists of two broad peaks which can be assigned to Q^3 and Q^4 species based on the isotrop-
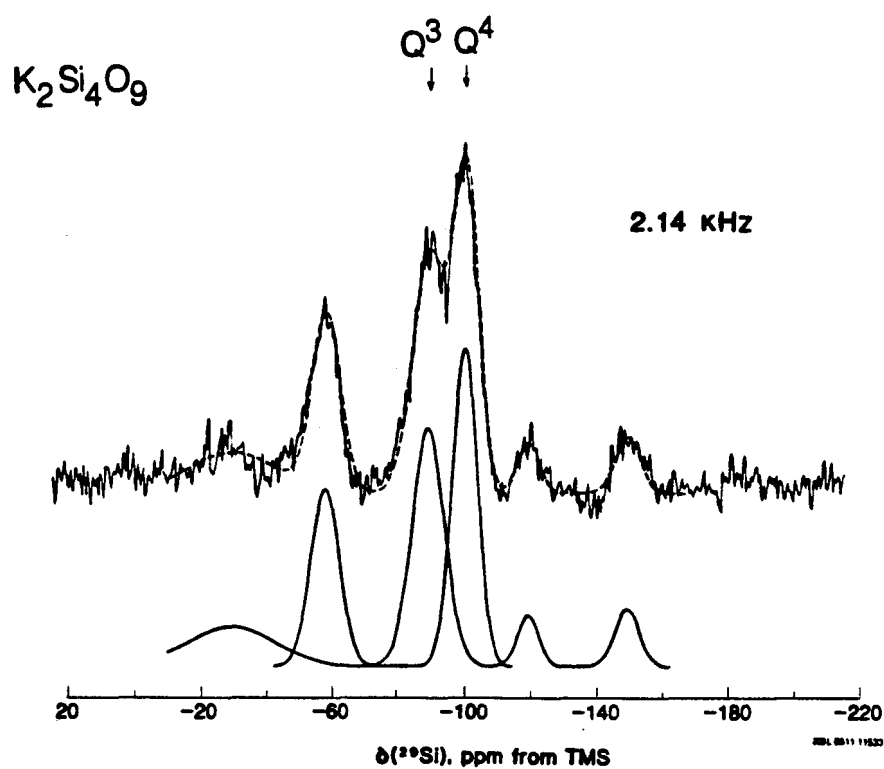
Figure 24: ^{29}Si MAS NMR spectra of $K_2Si_4O_9$ glass. A spinning speed of 3.58 kHz, a repeat time of 60 seconds and 1200 averages were used to acquire this spectrum. The deconvoluted spectrum is shown as previously described.

ic chemical shifts. Within the uncertainties of the deconvolution procedure, the linewidth of the Q^3 species is ≈ 2.5 ppm broader in the potassium compared to the sodium glasses. However, the linewidth of the Q^4 species decreases by 2.5 ppm in potassium tetrasilicate glass.

To examine the effects of large differences in cationic field strength, the ^{29}Si MAS NMR spectrum of a sodium and calcium glass were compared. The high liquidus temperatures and stable liquid immiscibility in the $CaO:SiO_2$ binary system necessitated that lower silica content glasses be prepared. This also permitted the effect of different average Q number to be examined.

For $(Na_2O)_{0.4}(SiO_2)_{0.6}$ (with average $Q^{2.67}$ speciation), two ^{29}Si resonance peaks are observed and assigned to Q^2 and Q^3 silicate species (Figure 25). The isotropic ^{29}Si chemical shift of crystalline Na_2SiO_3 (Q^2) is -76.8 ppm.[89] The chemical shifts of the Q^2 and Q^3 silicate species are in agreement (Table 4) with those previously observed by Grimmer et al.[89] (-77.7 and -87.3 ppm, respectively). The linewidth of the Q^3 species in the 40% Na_2O composition glass is within experimental error of the ^{29}Si linewidth observed in the 20% glass ($Na_2Si_4O_9$). The Q^2 linewidth is narrower (≈ 7.6 ppm) than the Q^3 site. If other silicate species are present, their abundance is low. The quantity of additional silicate polymerization species cannot be estimated unless restrictive assumptions about peak shape, position, and width are made. The maximum amount is estimated to be < 5%.

$(CaO)_{0.4}(SiO_2)_{0.6}$ (mean $Q^{2.67}$ composition) was also studied. The ^{29}Si MAS NMR spectrum of this single phase glass is composed of

$(Na_2O)_{0.4}$ $(SiO_2)_{0.6}$ Q^2 Q^3 2.58 kHz

$\delta(^{29}Si)$, ppm from TMS

+20   -20   -60   -100   -140   -180   -220

XBL 850-8971
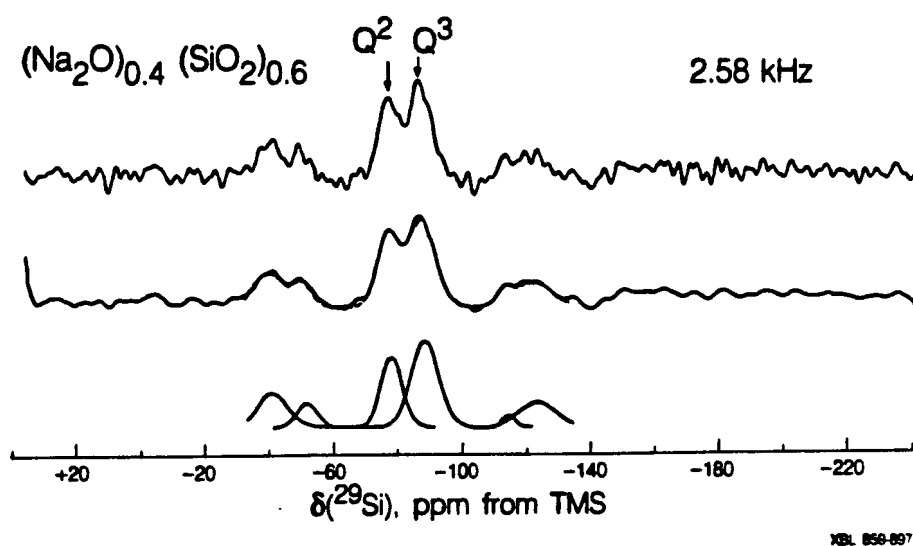
Figure 25: ^{29}Si MAS NMR spectra of $(Na_2O)_{0.4}(SiO_2)_{0.6}$ glass. A spinning speed of 2.58 kHz, a repeat time of 30 seconds, and 1200 averages were used to obtain this spectrum. The signal-to-noise was not sufficient to deconvolute the spectrum directly, hence a smoothing function was applied 20 times. The deconvolution of the averaged spectrum is shown, and was not substantially different before and after application of the smoothing function.

$(CaO)_{0.4} (SiO_2)_{0.6}$

~ 2 kHz

$\delta(^{29}Si)$, ppm from TMS

$+20 \quad -20 \quad -60 \quad -100 \quad -140 \quad -180 \quad -220$

XBL 859-8973
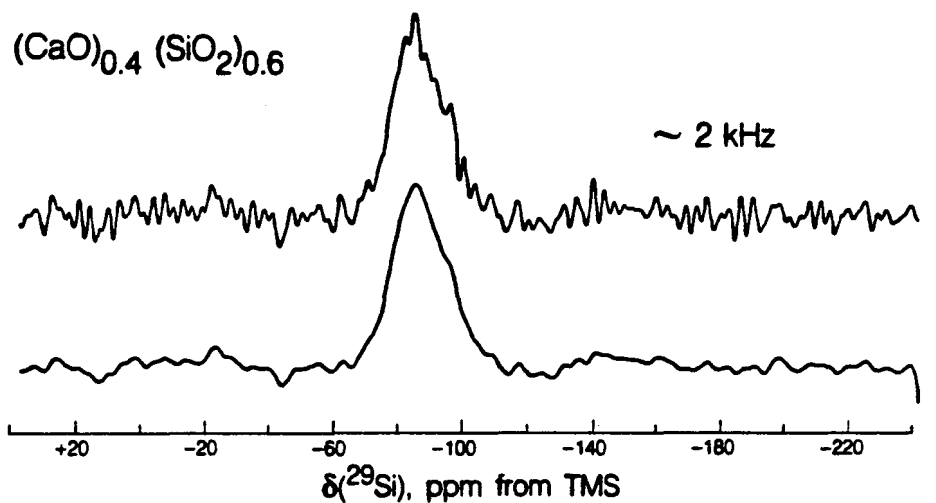
Figure 26: ^{29}Si MAS NMR spectra of $(CaO)_{0.4}(SiO_2)_{0.6}$ glass. A spinning speed of ≈ 2 kHz, a repeat time of 30 seconds, and 1400 averages were used to acquire this spectrum. No spinning sidebands were observed for the one broad, asymmetric peak. In the bottom spectrum, a smoothing function has been applied 20 times to reveal the possibility of a shoulder which might be the cause of the observed peak asymmetry. This smoothed spectrum illustrates that caution must be used when spectral manipulations are performed, especially on glass spectra.

only one very broad, asymmetric line, possibly with a minor shoulder at ~ -97 ppm (Figure 26). No unique deconvolution of this spectrum was possible without fixing peak positions or widths. If this 40% CaO glass spectrum is in fact composed of two overlapping peaks, with no species between the Q^2 and Q^3 sites, then the overall linewidth of the individual resonances must be much broader than for the 40% Na_2O analog.

A summary of isotropic $\delta(^{29}Si)$ and linewidths for the MAS NMR spectra of noninteger composition glasses is presented in Table 4.

V.3.iii. Chemical Shielding Anisotropy Analysis

The areas of central lines and spinning sidebands derived from deconvolution of the ^{29}Si spectra have been used to quantify some aspects of glass structure. In particular, the chemical shielding anisotropy (CSA) can be studied, perhaps more easily than by examining the static spectra with overlapping resonances. Other techniques, such as two-dimensional multiple pulse experiments exist for the separation of the CSA pattern as a function of isotropic ^{29}Si chemical shift.[111,112]

Glass spectra were obtained at several magic angle spinning speeds in an attempt to quantify the CSA. Using the method of Herzfeld and Berger,[22] described in Appendix A.4., the CSA tensor may be derived from the relative intensities of just a few spinning sidebands. Uncertainities arise because the sidebands overlap with the broad central peaks at some rotor speeds. Large errors can also result from the insensitivity of this technique to variations in

certain ranges of input data (especially for these glass spectra). The most precise quantity is the relative value, $\mu \propto \sigma_{33}-\sigma_{11}$ (Figure 47). However, the uncertainity in the ρ dimension (a measure of axial symmetry) is too large for small values of μ, to allow computation of the CSA tensor eigenvalues by this technique. In Table 4, $\sigma_{33}-\sigma_{11}$ values are presented for the noninteger composition silicate glass spectra. Errors were estimated based on the comparison of data from several spectra for each glass. Within these errors, $\sigma_{33}-\sigma_{11}$ for both Q^2 and Q^3 sites in the sodium glasses are approximately equal, and for the Q^4 species, the values are ≈ 0. Both of the $\sigma_{33}-\sigma_{11}$ values are similar to the results reported for crystalline $Na_2Si_2O_5$ (Q^3: $\sigma_{33}-\sigma_{11} = -107$ ppm and $\eta = 0.24$) and crystalline SiO_2 (quartz, Q^4: $\sigma_{33}-\sigma_{11}$ was estimated to be 0-20 ppm and η was not measurable).[26] No CSA analysis has been reported for potassium Q^3 or sodium Q^2 containing crystalline silicates.

A static ^{29}Si NMR spectrum of the 95% ^{29}Si isotopically enriched $Na_2Si_4O_9$ glass was also obtained (Figure 23). As anticipated, the Q^3 and Q^4 resonances overlap, but it is still possible to distinguish individual CSA tensor patterns. The Q^3 site has approximately axial symmetry with $\Delta\sigma \approx 98$ ppm (approximately 11.5 ppm of broadening was observed on the CSA pattern). The Q^4 site is observed to have very little or no asymmetry observable in the static ^{29}Si NMR spectrum, as anticipated. Because an isotopically enriched ^{29}Si sample was used, $^{29}Si-^{29}Si$ dipole-dipole couplings broaden the lines by ≈ 130 Hz.

TABLE 4 - ^{29}Si Chemical Shielding In Glass Alkali Silicates[*]

Composition	$\langle Q^n \rangle$	Relative Peak Areas			Overall FWHM	Silicate Species	σ_{iso}	Glass[e] $\sigma_{33}-\sigma_{11}$	FWHM (ppm)
		Ratio	Expected	Measured					
$(Na_2O)_{0.4}(SiO_2)_{0.6}$	$Q^{2.67}$	Q^2/Q^3	0.74[g]	0.70	20.4	Q^2	-76.3	112 ± 10	7.6
						Q^3	-86.5	113 ± 5	9.8
$(CaO)_{0.4}(SiO_2)_{0.6}$	$Q^{2.67}$	Q^2/Q^3	0.5	---[f]	19.9[c]	---[f]	-85.8[b]	---[f]	---[f]
$K_2Si_4O_9$	$Q^{3.5}$	Q^3/Q^4	0.97[g]	2.05	16.1	Q^3	-95.3	133 ± 15	11.5
						Q^4	-104.8	---[d]	8.9
$Na_2{}^{29}Si_4O_9$	$Q^{3.5}$	Q^3/Q^4	1.0	1.03[a]	24.5	Q^3	-92.2	109 ± 10	10.3
						Q^4	-106.4	---[d]	11.7
$Na_2Si_4O_9$	$Q^{3.5}$	Q^3/Q^4	1.07[g]	1.27	21.5	Q^3	-93.0	112 ± 5	9.8
						Q^4	-105.9	---[d]	11.5

---

[*] all frequency units are given In terms of ppm from TMS

[a] assuming area for the first Q^3 spinning sideband, and removing from Q^4 peak

[b] peak maximum, position uncertainity ± 0.5 ppm

[c] FWHM, uncertainity ± 1.5 ppm

[d] symmetry of ^{29}Si site Is very high, hence no spinning sidebands were observed. K.A. Smith et al.[26] estimate $\Delta\sigma$ = 0-20 ppm for Q^4 [0 All In crystalline minerals.

[e] uncertainity of deconvoluted peak position ± 0.2 ppm; and FWHM ± 0.3 ppm

[f] nonunique deconvolution

[g] anticipated relative peak area based on alkali compositional analysis of sample. $(Na_2O)_{0.4}(SiO_2)$ Is 42.41 wt% Na_2O. $K_2Si_4O_9$ Is 27.80 wt% K_2O. $(Na_2O)_{0.4}(SiO_2)_{0.6}$ Is 21.02 wt% Na_2O.

V.3.iv. Population Distribution

The area under an NMR absorbance line is directly proportional to the number of nuclei resonating at that frequency, and in principle, accurate spectral deconvolution should give a precise distribution of species as well as details of structure. For crystalline materials much information has been obtained, but problems may arise for the broad, overlapping peaks in glass spectra. In particular, certain lineshape assumptions may not be reasonable because of the number of structural features which effect the chemical shift. Nonetheless, relative areas of the two resonances observed for the enriched sodium containing glass is within error of what would be expected simply from the mean composition (Table 4). This information can not be taken as evidence that species other than the two major ones are absent, only that they are in low abundance (estimated to be less than 5%). These results are consistent with Raman spectroscopy on similar materials which suggest the presence of a statistical distribution of at least three species in most compositions.

In the $K_2Si_4O_9$ glass and to a lesser degree, in the natural abundance $Na_2Si_4O_9$ glass, the Q^4 peak area is much smaller than is expected from the chemical composition. The discrepancy in relative peak area and the difference in Q^3 and Q^4 spin-lattice relaxation times indicates that the Q^4 species might not have completely relaxed during the time between rf pulses. It is also possible that the Q^4 peak in potassium tetrasilicate glass is skewed towards less negative chemical shifts (lower Q^n species), instead of having a Gaussian form. An asymmetric Q^4 lineshape has also been observed by by Dupree and

Petifer[85] in SiO_2 glass.

V.3.v. Conclusions

Murdoch et al.[17] were the first to make a careful, quantitative comparison of alkali versus alkaline earth silicate glass structure using ^{29}Si MAS NMR. This work has been extended in this report to include glasses of nonintegral mean Q^n composition.[115] For homogeneous, single phase glasses of integral mean Q^n polymerization state, only one broad resonance is observed. However, two discrete resonances are observed in the ^{29}Si MAS NMR spectra of alkali silicate glasses of nonintegral mean Q^n composition.

As assumed in several previous reports,[17,89] two partially resolved peaks are interpreted as corresponding to two structural sites and the single broad resonance is presumed to be caused by the presence of one silicate species. However, similar broad, single peaks are also observed for alkaline earth glasses (or at least those containing Mg and Ca) with nonintegral mean Q^n composition. The single broad peaks could be partially due to a continuum in the Q^n speciation sites: If the distinction between "bridging" and "non-bridging" oxygen atoms begins to blur as the field strength of the "network modifying" cation increases, then this could be the case. However, Raman spectroscopic data on silicate glasses[56,68] show partially resolved peaks which have been attributed to Si-O stretching motions of distinct Q^n sites with integral values of n. Hence, the presence of a range of noninteger composition Q^n species in glasses with higher field strength cations can not be used to explain trends

in glass ^{29}Si NMR linewidths.

When comparisons can be made, the isotropic ^{29}Si chemical shift is comparable in glasses and the corresponding crystalline compounds. From the location of the isotropic chemical shifts, it is known that the same bonding coordination of the oxygen atoms around the silicon atoms occurs in the glass as well as in the crystalline material.

Data on ^{29}Si chemical shielding anisotropy will yield important information on site local electronic symmetry, although the best approach to obtaining this type of data on glasses is to use both static and magic angle spinning NMR techniques. As in crystalline framework silicates, the chemical shielding anisotropy is small or unmeasurable for Q^4 species in glasses regardless of composition.[115] The small $\Delta\sigma$ value implies that a highly symmetric electron distribution exists in glasses as well as crystalline solids. This is possible only if tetrahedral Si-O bonding occurs, hence the Q^4 tetrahedra are not found to be distorted in glasses (in accord with McMillan's interpretation of Raman data).[56,68] In the alkali silicate glasses examined,[115] the Q^3 species is present in an axially symmetric environment--that is with three equivalent Si-O bonds occuring. The Q^2 site in $(Na_2O)_{0.4}(SiO_2)_{0.6}$ also appears to have axial symmetry. Additionally, all the Q^2 and Q^3 sites investigated appear to have approximately the same chemical shielding anisotropy $(\Delta\sigma)$.

^{29}Si NMR spectra indicate that the four Si-O bonds as well as the average number (and most probable number) of Si-O-Si bonds remain intact in the glass phase. NMR spectroscopy also shows that the local environment for Q^3 silicate species is less symmetric in the

crystalline form than in the glass state. In most of the crystalline silicate compounds investigated by K.A. Smith et al.,[28] silicate polymerization species (other than Q^4) have asymmetric CSA tensors. This result implies that the SiO_4^{4-} tetrahedra are composed of inequivalent Si-O bonds which cause a nonuniform electronic environment to be observed due to the long range order imposed by the crystal structure. These distorted SiO_4^{4-} units are in higher energy bonding configurations than a tetrahedrally symmetric species would be. The lower bonding energy, more symmetric local environments observed in glass silicate species must be caused by relaxation of the strained silicate units in the molten phase. Removal of the bonding strain in the glass state is possible due to the lack of long range order constraints.

As observed by ^{29}Si NMR, symmetric Si-O-Si bonding configurations exist in a homogeneous, single phase silicate glass. Because the ^{29}Si-^{29}Si coherence transfer experiments were unsuccessful, the proximity of the two sites found in $Na_2Si_4O_9$ glass remains unknown. It is known from the optical clarity of the glass that structural domains are suboptical in size. Using powder x-ray diffraction, the maximum crystallite size is known to be ≈ 20 Å (or 5 to 10 unit cells) because no sharp lines appear in the broad powder pattern. Hence mixing of the two species may occur on a molecular level. Unfortunately, the data obtained does not allow further restraints to be placed on the relative proximity of the silicate species.

Based on the relative peak areas of the Q^3 and Q^4 species in $K_2Si_4O_9$ and $Na_2Si_4O_9$ (and assuming symmetric lineshapes), the Q^4

species in $K_2Si_4O_9$ appears to have a much longer T_1 than does the Q^3 species. A possible explanation for the differences in relaxation times could be that the predominant source of relaxation in natural abundance silicate glasses is via the CSA interaction and by dipole-dipole coupling to the quadrupolar charge balancing cation. This mechanism is possible because the potassium glass is relaxing more slowly than the sodium glass. Potassium has a much smaller gyromagnetic ratio than sodium ($\gamma_{Na}/\gamma_K \approx 1/6$), hence the coupling would be one sixth as strong. Since the Q^3 species appears to relax more slowly than the Q^4 species in $K_2Si_4O_9$ glass and dipole-dipole coupling to potassium is assumed to be part of the relaxation mechanism, it can be concluded that the Q^3 silicon species are closer to K^+ than the Q^4 silicon atoms. An additional fact which supports this premise: in SiO_2 glass, the spin-lattice relaxtion time is very long (on the order of 10 minutes). The only mechanism for relaxation in vitreous SiO_2 are $^{29}Si-^{29}Si$ dipole-dipole coupling (very weak), and the CSA of a Q^4 silicon species (very small), and whatever paramagnetic impurities may be present. Few relaxation time measurements have been made for crystalline silicates,[160,161] and none have been previously published on glasses.[115] However, in general, ^{29}Si spin-lattice relaxation times are known to be very long (4 to 5000 seconds) in silicate minerals.

The predominant silicate species found in glasses is the same Q^n polymerization state, if the glass is of integral mean Q^n composition. Or, if the glass is of noninteger composition, then the adjacent integral Q^n polymerization species are the primary sites present

In the glass state---In the same quantity as predicted by the glass composition. The ^{29}Si NMR spectra do not eliminate the possibility of other integer composition species being present in the glass phase; however, the spectra do limit the quantity of these species to an estimated maximum of 5%.

The glass ^{29}Si NMR spectral analysis, however, does not explain the breadth of the glass MAS spectral lines. The large linewidth of glass ^{29}Si spectra must be due to finite ranges of several interrelated structural parameters, such as bond angle and bond length. Examination of the ^{29}Si spectrum of vitreous SiO_2 lends credence to this conclusion--SiO_2 glass contains no network modifying cations to change the distribution of Q^n species and yet has a linewidth of 13.2 ppm (contrasted to the 0.4 ppm linewidth observed for the crystalline material). The MAS linewidth reflects a range of Si-O-Si bond angles from $\approx 135°$ to $\approx 160°$, a result which is in good agreement with radial distribution function and molecular dynamics calculations.[51,83,84] Most structural parameters are assumed to take on a larger range of values as the interaction of cations with both bridging and nonbridging oxygen atoms increases. This result is verified by the increase of the ^{29}Si MAS NMR linewidth of alkali and alkaline earth silicate glasses as a function of the incease in polarizing power of the network modifying cation.[17]

Because of the many influences on ^{29}Si chemical shifts, it is difficult to uniquely constrain any one structural variable from the spectra of glasses. However, the sensitivity to geometrical changes and the one-to-one correspondance between signal intensity and number

of resonating nuclei will allow ^{29}Si glass NMR spectra to be very valuable for verifying specific, detailed, structural models. For quantitative work, all nuclei must relax completely or at least equally, and spinning sidebands must be included if present. Accurate empirical or theoretical relationships between structural parameters and chemical shifts are of course needed.

V.4. Aluminosilicate Glass Structure

Tectosilicate glasses have been examined by several investigators[17,90,92,131] in which aluminum is believed to act as a network forming cation, substituting for Q^4 silicon atoms in tetrahedral units rather than changing the degree of polymerization in the role of an octahedrally coordinated network modifier.[55,86]

V.4.i. Aluminosilicate Speciation

De Jong et al.[90] have used ^{29}Si MAS NMR to compare nucleation properties of two glasses prepared from naturally occuring minerals, albite (NaAlSi$_3$O$_8$, Q^4[1 Al]) and anorthite (CaAl$_2$Si$_2$O$_8$, Q^4[4 Al]). One broad peak was observed for both glasses. Each spectrum was deconvoluted by a technique similar to that used by Schramm et al.,[91] however the equilibrium expression in Equation (46) was used as a model. The authors[90] conclude that all five possible silicate species are present in these two aluminosilicate glasses.

Kirkpatrick et al.[92] also examined albite and anorthite glass using MAS NMR. The ^{29}Si, ^{27}Al, and ^{23}Na NMR spectra of these glasses consist of broad peaks, much wider than the corresponding spectra of

crystalline albite and anorthite (except the [27]Al spectrum of anor-
thite glass). The broad Al and Na glass linewidths are attributed to
silicon atoms occupying a distribution of sites, each with a differ-
ent quadrupole coupling constant, asymmetry parameter and/or chemical
shift. The [29]Si linewidth has been interpreted,[92] in a manner similar
to de Jong et al.,[90] to be caused by chemical shifts from the five
possible Q^4[k Al] species, all of which are presumed to be present in
the glass state. In anorthite glass, the [29]Si resonance is asymmetric
and the authors[92] attribute this to a nonuniform distribution of
silicon polymerization species (more Q^4[4 Al] are present than
Q^4[0 Al]). [29]Si chemical shifts for the peak maximum of albite glass
(-98 ppm) and anorthite glass (-87 ppm) agree with the results of
de Jong et al.[90] De Jong et al.[110] also used ^{27}Al MAS NMR to inves-
tigate aluminum coordination in crystalline and amorphous aluminosil-
icates. In all the glasses observed (albite, potassium feldspar,
anorthite, lithium feldspar, jadeite, spodumene, nepheline, cordier-
ite, and calcium aluminate), the aluminum was 4-coordinate (even in
jadeite glass, in which Al was found to be 6-coordinate in the crys-
talline phase).

V.4.ii. Effect of Cations on Aluminosilicate Speciation

In analogy to the results obtained for metasilicate and disili-
cate glasses, Murdoch et al.[17] found strongly polarizing cations
shift the equilibrium in Equation (46) to the right. This shift
causes cations to cluster near the aluminate tetrahedra linked to
Q^4[(k+1) Al] silicate species and gives rise to a larger distribution

of the number of aluminate neighbors around different silicon atoms. Raman spectra reported by McMillan et al.[87] support this mechanism.

The trend for smaller, more highly charged cations to cause a broader distribution of sites is apparent in the ^{29}Si MAS NMR spectra of aluminosilicate glasses with a Si/Al ratio of 3:1.[17] The ^{29}Si spectra of potassium feldspar ($KAlSi_3O_8$), albite ($NaAlSi_3O_8$), and $Ca_{0.5}AlSi_3O_8$ are shown in Figure 27. The glass peaks grow broader as the cation polarizing power increases from K^+ to Na^+ to Ca^{2+}, reflecting a larger distribution of $Q^4[k$ Al] species and probably a wider range of Si-O-T bond angles (where T = Si or Al).

Radial distribution function measurements of $NaAlSi_3O_8$ and $KAlSi_3O_8$ glasses suggest the presence of six membered rings containing alkali cations in the center (a "stuffed trydimite" type of structure).[52] But the Raman spectrum of $Ca_{0.5}AlSi_3O_8$ has been interpreted in terms of both six membered SiO_2 rings and four membered $Al_2Si_2O_8$ (feldspar-like) rings.[81] The existence of two different sized rings for the calcium glass would be expected to result in a wider range of tetrahedral angles, and hence a broader ^{29}Si line would be observed.

Figure 28 compares the ^{29}Si spectra of two tectoaluminosilicate glasses with a Si/Al ratio of one: $NaAlSiO_4$ (nepheline) and $CaAl_2Si_2O_8$ (anorthite). Integrated linewidths for both sets of glasses are plotted as a function of cation polarizing power in Figure 29. Inspection of Figure 28 or 29 reveals that the width of the anorthite glass peak exceeds that of nepheline glass. One cause for this difference might again be a greater range of bond angles in
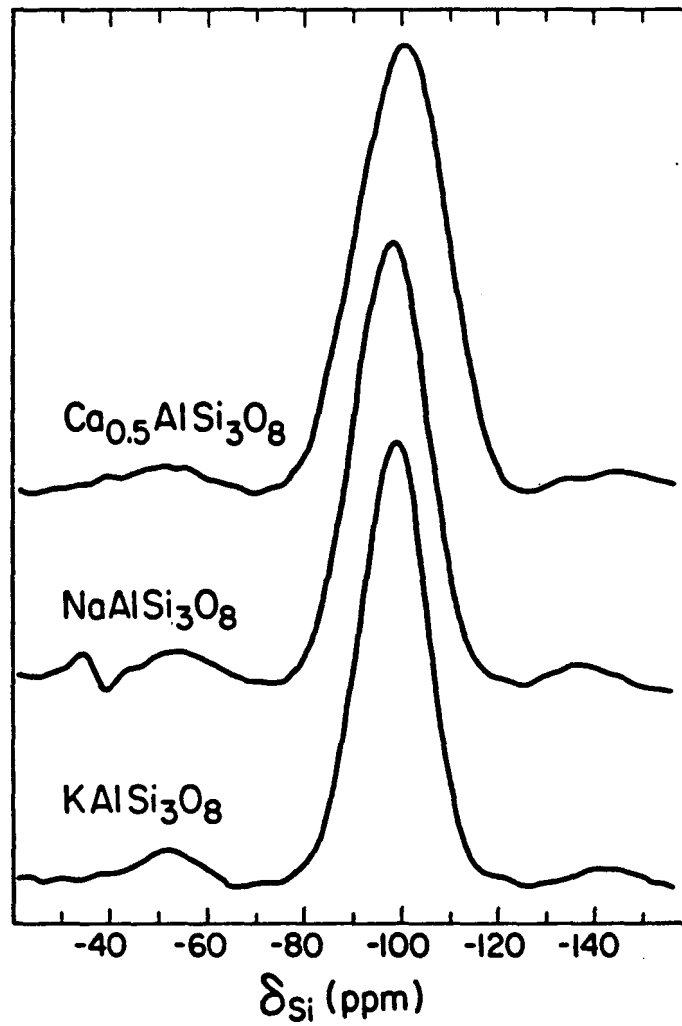
Figure 27: ^{29}Si MAS NMR spectrum of tectosilicate glasses with a Si/Al ratio of 3 ($KAlSi_3O_8$, K-feldspar; $NaAlSi_3O_8$, albite; and $Ca_{0.5}AlSi_3O_8$). The dip to the left of the albite peak is a spectral artifact. These spectra are from reference 17.
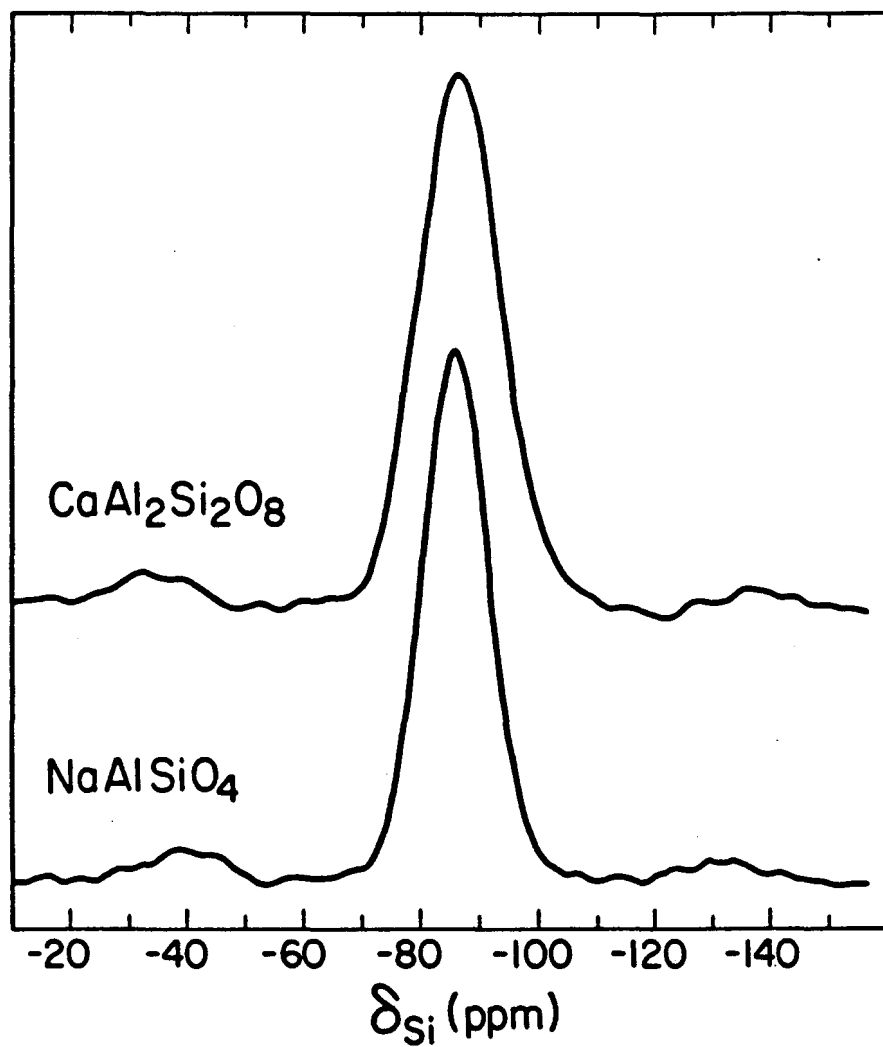
Figure 28: ^{29}Si MAS NMR spectrum of tectosilicate glasses with a Si/Al ratio of 1 ($CaAl_2Si_2O_8$, anorthite; and $NaAlSiO_4$, nepheline). These spectra are from reference 17.
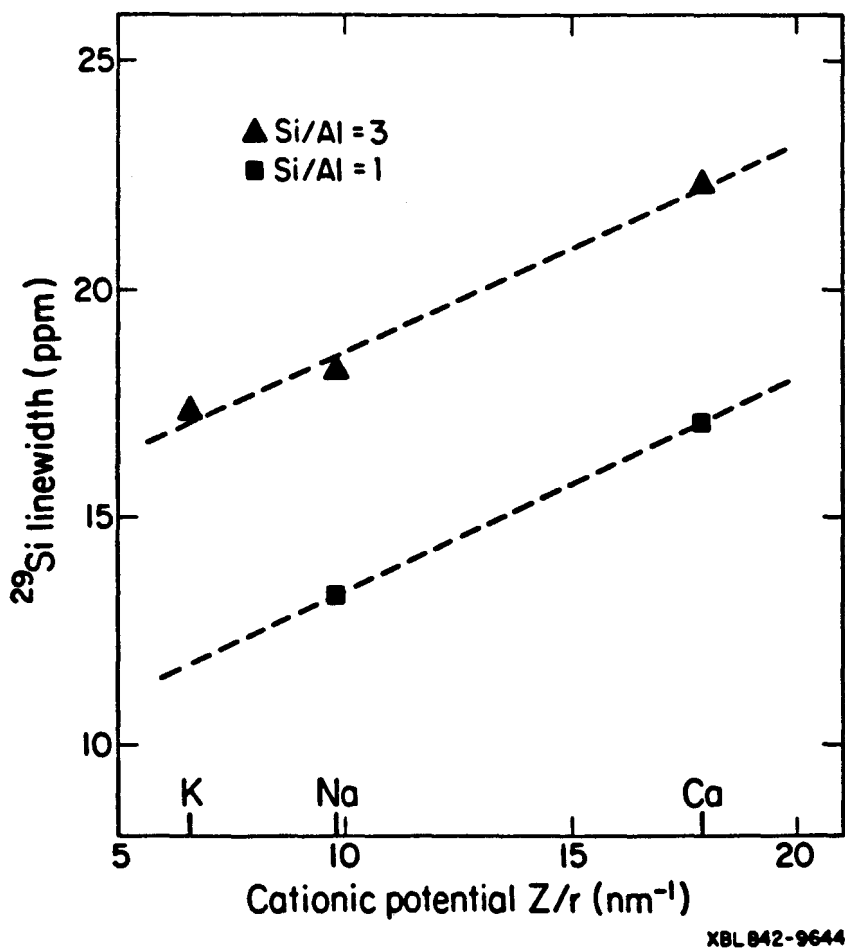
Figure 29: Integrated linewidths of tectosilicate glasses as a function of cationic potential for different Si/Al ratios. The ^{29}Si linewidth is observed to increase with increasing cation polarizing power. This figure is from reference 17.

the anorthite glass. Radial distribution function measurements[52,53] indicate that the two glasses have markedly different structures: six membered, "stuffed tridymite" rings in nepheline glass, and four membered feldspar-like rings in anorthite glass. The smaller rings may well entail more variety in bond angles. Additionally, on the basis of Raman data, Seifert et al.[81] postulated the existence of a small quantity of six membered rings in addition to the four membered rings in $CaAl_2Si_2O_8$ glass. This variation in structure would be expected to create a wider range of bond angles.

V.4.iii. Silicon-Aluminum Ordering

In crystalline nepheline and anorthite, silicon and aluminum cations alternate in the tetrahedral framework---each silicon atom is surrounded by four aluminum atoms and _vice versa_. The alternating arrangement of Al and Si is a manifestation of Loewenstein's aluminum avoidance rule,[132] which states that Al-O-Al linkages between aluminate tetrahedra are energetically unfavorable. If this principle holds in glasses as well, then equilibria such as Equation (46) are not important in Si/Al = 1 compositions since every silicate tetrahedron must be a Q^4[4 Al] unit.

Sharma et al.[86] have seen evidence in their Raman spectra of Si-Al disorder in anorthite glass. So, another possible interpretation of the increased [29]Si linewidth in anorthite is the greater polarizing power of calcium induces a breakdown in aluminum avoidance. However, when examined as a function of Si/Al ratio (Figure 30), the linewidths of Figure 27 and 28 are consistent with substan-

XBL848-9860
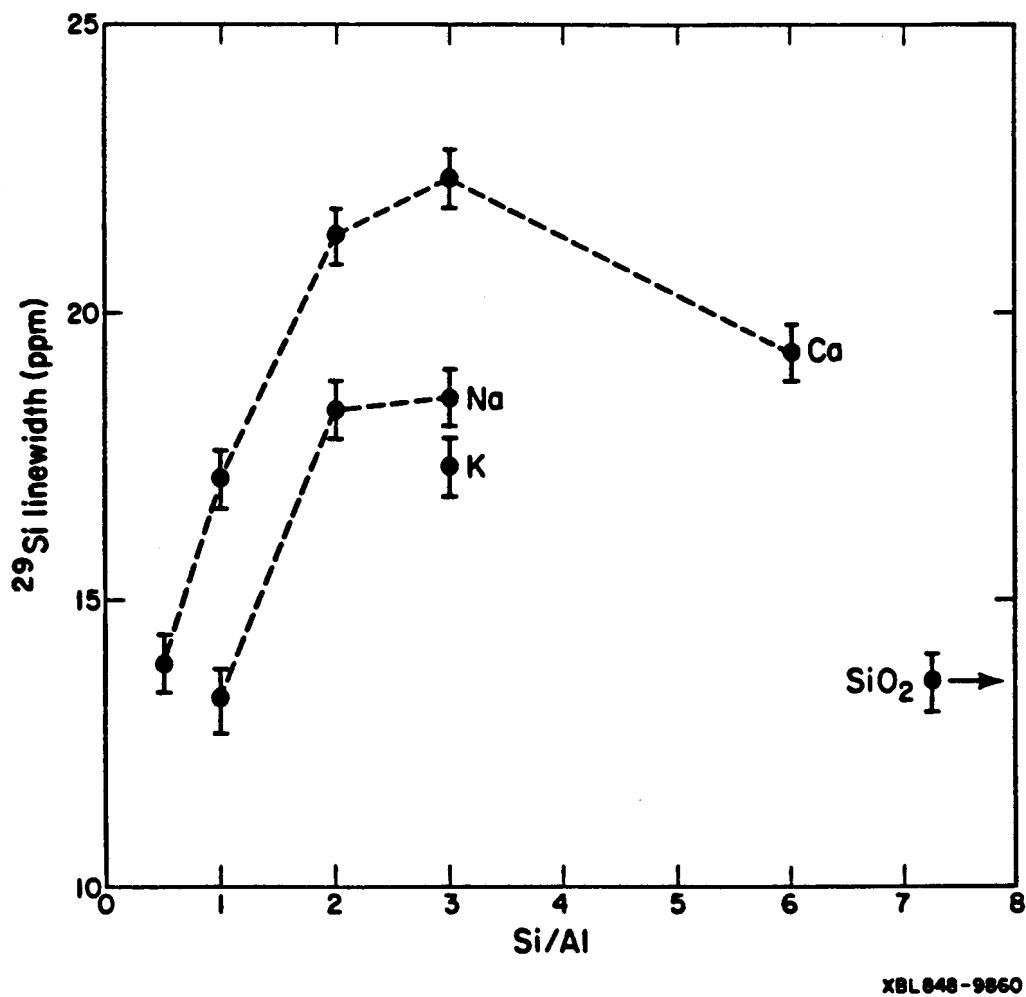
Figure 30: Integrated linewidths of tectosilicate glasses as a func-
tion of Si/Al ratio for different charge balancing cat-
ions. This figure is taken from reference 17.

tial adherence to Loewenstein's rule. Specifically, the width of the albite glass peak is 4.9 ppm greater than that of nepheline glass, and the width of the $Ca_{0.5}AlSi_3O_8$ glass peak is 5.2 ppm greater than that of anorthite glass. In short, glasses for which substantial rearrangement of Si and Al cations is possible without creating Al-O-Al linkages have broader linewidths than those for which compliance with the aluminum avoidance principle imposes a rigid ordering scheme.

Murdoch et al.[17] considered a statistical model for silicon aluminum ordering, with and without the aluminum avoidance constraint. Without the restrictions of aluminum avoidance, the relative occurrence of a Q^4[k Al] silicate tetrahedron is given by the probability of choosing k aluminum neighbors and (4-k) silicon neighbors. The average number of aluminum neighbors (which governs the location of the ^{29}Si peak maximum) is given by[17]

$$\langle k \rangle = \frac{4}{(R + 1)} \quad , \tag{53}$$

where R is the Si/Al ratio in a three dimensional framework glass. (The peak maximum corresponds to the average value of k only for a symmetric lineshape, but the difference between $\langle k \rangle$ and its most probable value is not important here.) The variance in the number of aluminum neighbors (which contribute to the NMR linewidth) is given by[17]

$$\sigma^2 = \langle k^2 \rangle - \langle k \rangle^2 = \frac{4R}{(R + 1)^2} \quad . \tag{54}$$

The variance is a maximum ($\sigma^2 = 1$) when R = 1 (i.e., for a composition like that of anorthite or nepheline). For R = 3 (as in albite glass), $\sigma^2 = 0.75$.

In contrast, the imposition of aluminum avoidance requires four Si-O-Al linkages for each aluminum atom present. The relative occurrence of each $Q^4[k \, Al]$ silicate tetrahedron has been determined by Klinowski et al.[67] Using this distribution, $\langle k \rangle = 4/R$ and

$$\sigma^2 = \langle k^2 \rangle - \langle k \rangle^2 = 4 \, (R - 1) \, / \, R^2 \,. \tag{55}$$

In this case, the variance is zero (no disorder) for R = 1, and achieves its maximum value of 1.00 for R = 2, and falls to 0.89 for R = 3.

As noted above, the variance of k contributes at least in part to the NMR linewidth of aluminosilicate glasses. To explore this effect, ^{29}Si spectra were acquired for jadeite ($NaAlSi_2O_6$) glass and a series of glasses of the formula $CaAl_2O_4 \cdot n \, SiO_2$ (n = 1, 2, 4, 6 and 12). Results are included in Figure 30, and are clearly more consistent with an aluminum avoidance effect than with its absence. However, linewidth maxima for both Na and Ca glasses occur near R = 3, not R = 2. This result, perhaps indicates that Si-O-T bond angles also increase with the Si/Al ratio. Such a conclusion is supported by the molecular orbital calculations of Geisinger et al.,[133] which suggest that as the Si-O-T (where T = Si or Al) angle varies from its most stable value, energies increase more rapidly for Si-O-Al than for Si-O-Si.

V.4.iv. Natural Composition Glasses

To investigate the usefulness of ^{29}Si MAS NMR in the analysis of magmas, Murdoch et al.[17] observed three glasses made experimentally from iron-poor silicic lavas collected at Mono Craters (A), Mount Lassen (B), and Mount Shasta (C), California. All three were remelted under reducing conditions in graphite crucibles; calculations[134] indicate that > 99% of the iron present is Fe^{2+}. Rhyolitic glass A can be represented by an approximately one third silica glass, one third albite glass, and one third potassium feldspar glass. In going to glasses B and C, the K-feldspar component is partially replaced by anorthite, and the number of nonbridging oxygen atoms increases. The decrease in the number of Si-O-Si bonds causes a decrease in the average degree of polymerization. Nevertheless, all three glasses are expected to have predominantly three dimensional framework structures (i.e., mostly Q^4 tetrahedra are present).

The ^{29}Si NMR spectra of the natural composition glasses are displayed in Figure 31. The most obvious trend is the increase in spinning sideband intensity between glass A and B and C. This change is not related to a massive increase in chemical shielding anisotropy but rather to an increase in concentration of paramagnetic Fe^{2+} ions. Magnetic dipole-dipole ccoupling between the rapidly relaxing unpaired electrons on the iron and nearby silicon-29 nuclei induces a paramagnetic shift in the NMR spectra of these nuclei. The form of this largely inhomogeneous shift is similar to that of a chemical shift, but the magnitude can be much greater.[136] As the concentration of iron increases, the number of silicon nuclei affected by

XBL 848-3383
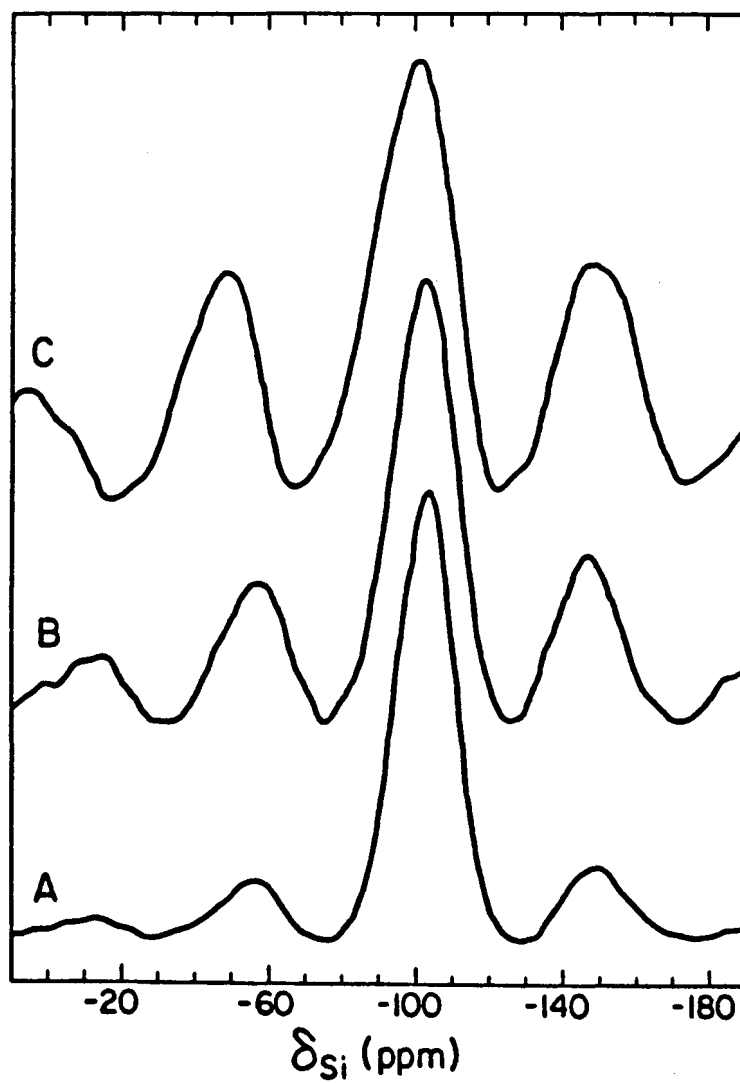
Figure 31: ^{29}Si MAS NMR spectrum of glasses made from lava collected at (A) Mono Crater, (B) Mount Lassen, and (C) Mount Shasta, California. All three central peaks are normalized to the same height, but the weight percent of silicon and, hence the measured signal intensity decrease going from glass A to B to C. The spectra are from reference 17.

paramagnetic shifts rises; as a result, spinning sidebands cover a wider range of frequencies and become more intense. Oldfield et al.[135] reported a similar effect in minerals caused by ferromagnetic inclusions, but such inclusions were not observed microscopically in these glasses.

The overall spectral intensity (including sidebands) also drops from glass A to B to C; the relative values are 1.00:0.70:0.37. This drop also is a function of increasing paramagnetic content. Those silicon nuclei that are located very near unpaired electrons not only experience a large shift but also relax rapidly.[6] Both effects can cause such severe broadening that these perturbed silicon atoms are not seen at all in the spectrum.

The linewidths and chemical shifts of the three center peaks are tabulated in Table 5. An unambiguous analysis is difficult because in going from glass A to B to C, two factors---the decrease in the Si/Al ratio, and the increase in the number of nonbridging oxygen atoms would be expected to broaden the peak and shift its maximum to less negative values of the chemical shift. Moreover, additional broadening is caused by the paramagnetic ions present, as found by Grimmer et al.[137] in a study of Fe, Mg substitution in synthetic olivines.

The location of the peak maximum, however, is largely dependent on the Si/Al ratio. Consulting Table 3, the average chemical shift for alkali feldspar glasses is found to be approximately -98.5 ppm and the average number of aluminum neighbors per silicate tetrahedron is 4/3 = 1.33. In comparison, the silica glass NMR peak lies at -111 ppm

Table 5: Isotropic ^{29}Si chemical shifts, linewidths, and Si/Al ratio of the natural composition glasses investigated by ^{29}Si MAS NMR.[17]

Glass	Location	Si/Al ratio	$\delta(^{29}Si)$ (ppm)	FWHM (ppm)
A	Mono Crater	5.17	-103.5	19.0
B	Mount Lassen	3.96	-101.8	21.7
C	Mount Shasta	3.13	-99.8	24.8

and $\langle k \rangle$ = 0. From these two data pairs, the following linear relationship is obtained

$$\delta(ppm) = -111 + 9.4 \langle k \rangle$$

$$= -111 + 37.5 / R \ . \tag{56}$$

Using values for R (Si/Al ratio) calculated from electron microprobe analysis of the glass composition in Table 5, the peak maxima can be predicted to lie at -103.5, -101.5, and -99.0 ppm for samples A, B, and C respectively. These numbers are close to the experimental measurements.

V.4.v. Conclusions

In analogy to the results obtained for metasilicate and disilicate glasses, ^{29}Si MAS NMR spectra indicate that smaller, more highly charged network modifying cations shift the equilibrium in Equation (46) to the right. This shift causes cations to cluster near the aluminate tetrahedra linked to $Q^4[(k+1)$ Al] silicate species and gives rise to a larger distribution of the number of aluminate neighbors around different silicon atoms. Raman spectra reported by McMillan et al.[87] support this mechanism.

Murdoch et al.[17] observed that glasses in which substantial rearrangement of Si and Al cations is possible (without creating Al-O-Al linkages) have broader linewidths than those glasses where compliance with the aluminum avoidance principle imposes a rigid ordering scheme. This result indicates that any type of long range order restricts the distribution of structural variables (e.g. Si-O

and Al-O bond lengths, or Si-O-Si and Si-O-Al bond angles). The dependence of linewidth on the Si/Al ratio indicates, however, that the aluminum avoidance principle is obeyed.

Because the isotropic chemical shift is sensitive to a variety of structural features affecting a silicon-29 nucleus (the number of nonbridging oxygen atoms, the identity of neighboring tetrahedral cations, bond angle values, and the presence of nearby paramagnetic ions), the spectra of multicomponent glasses cannot be readily interpreted. Nonetheless, the location of peak maxima for the three natural composition glasses examined[17] have been correlated with a Si/Al ratio.

CHAPTER VI:

MOLTEN ALUMINOSILICATES

High temperature, high resolution ^{23}Na, ^{27}Al, and ^{29}Si NMR spectra were obtained in sodium aluminosilicate melts. The compositions investigated are: Na_2SiO_3; $Na_2Si_2O_5$ and $KNaSi_2O_5$; $Na_2Si_4O_9$; jadeite ($NaAlSi_2O_6$); and R-15 (an aluminosilicate with composition: 50 mole% SiO_2, 35 mole% Na_2O, and 15 mole% Al_2O_3).

Isotropic ^{29}Si and ^{23}Na chemical shifts can be obtained in a melt, due to the presence of motion, allowing for comparison of the local structure of crystalline, glass, and molten silicate compounds. At lower temperatures, the loss of motion causes line broadening. Relaxation times are measured to characterize the motions undergone by sodium and silicon atoms in liquid silicates. The high temperature, high resolution NMR apparatus required for this investigation is described in Appendix C.

VI.1. ^{29}Si Measurements

All high temperature ^{29}Si measurements required the use of isotopically enriched samples. The ^{29}Si NMR spectra of molten silicates usually consist of one narrow (60 - 200 Hz, or 1.5 - 6 ppm) symmetric, Lorentzian-shaped line (Figure 32) as observed in solution state NMR spectra. The lineshape indicates that rapid molecular motion and/or chemical exchange is present in silicate liquids, averaging the effects of internuclear dipole-dipole coupling ($\approx$ 130 Hz) and chemical shielding anisotropy (for $H_o \approx$ 42 kG, $\Delta\sigma \approx$ 3.5 kHz). As temperatures decrease, the melt viscosity increases, motions slow and line broadening occurs, as shown in Figure 33 for sodium tetrasilicate. The dynamics in silicate liquids may be composed of poly-
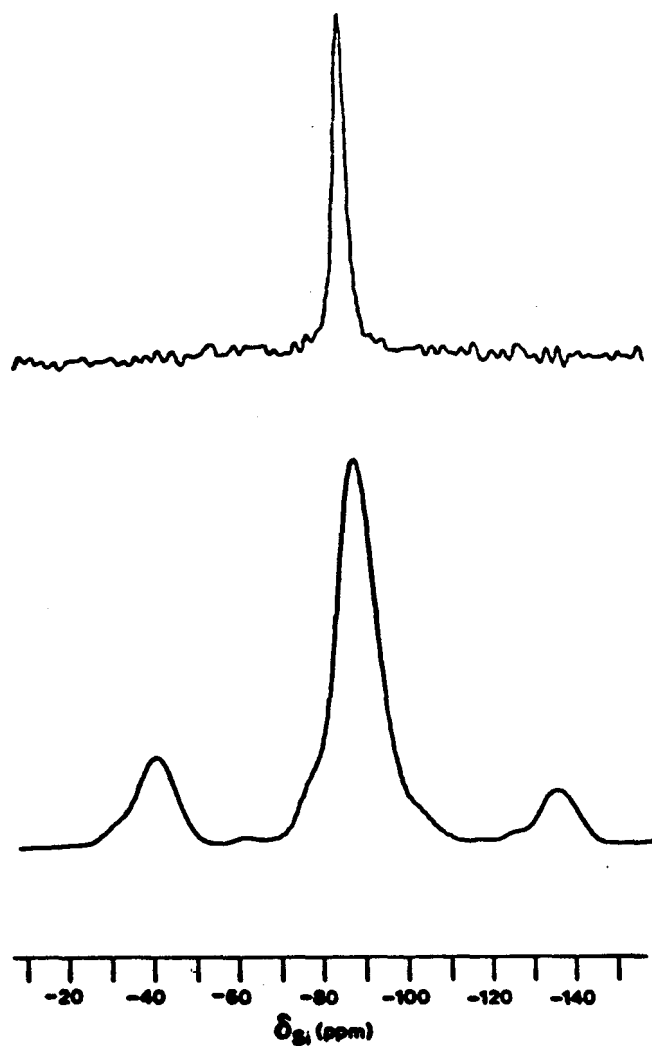
Figure 32: ^{29}Si NMR spectra of sodium disilicate. (lower) The ^{29}Si MAS NMR spectrum of glass $Na_2Si_2O_5$. The breadth of the line is due to a range of isotropic chemical shifts caused by a distribution in Si-O-Si bond angles and Si-O bond lengths in the glass state. (upper) ^{29}Si NMR spectrum of molten $Na_2Si_2O_5$ (825°C). Motional averaging allows only a time average (of the range of bond angles and bond lengths present in the glass) to be observed in the liquid state.

XBL 8511-11520
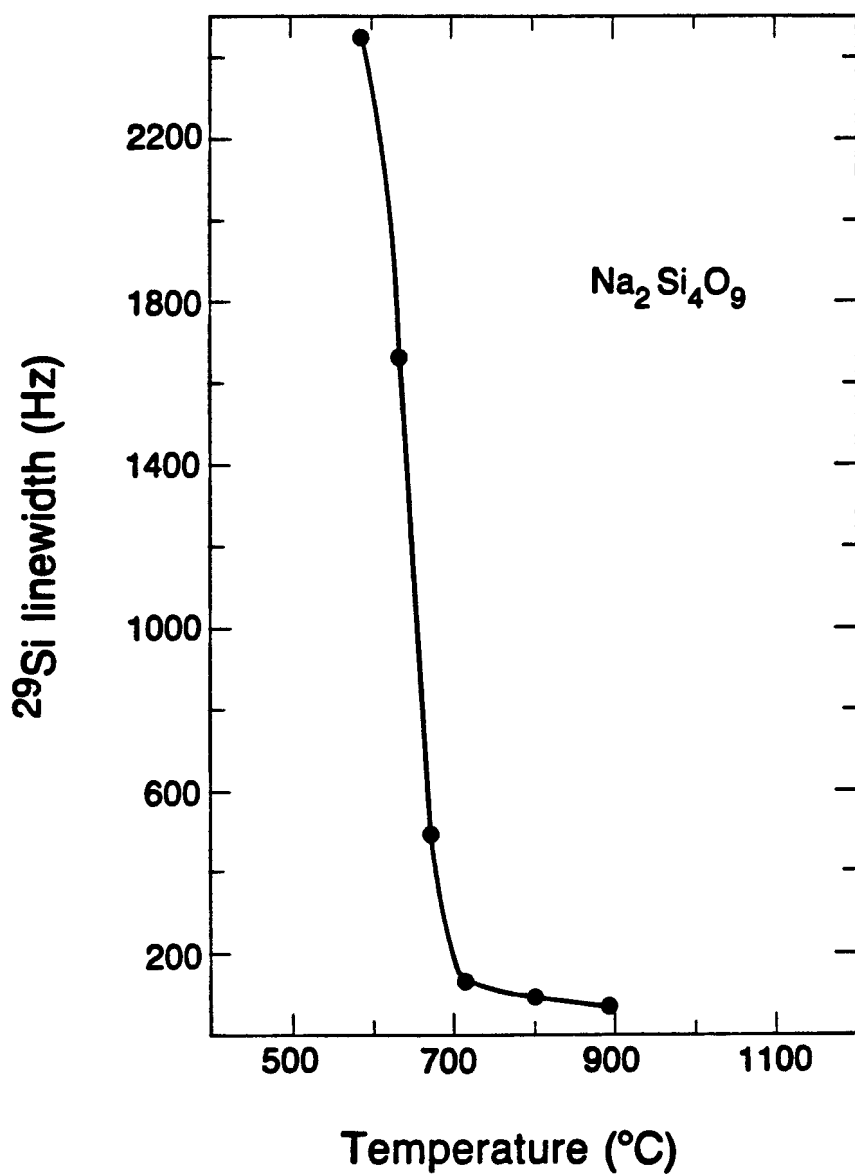
Figure 33: ^{29}Si linewidth of liquid sodium tetrasilicate as a function of temperature. As temperature is decreased, the melt viscosity increases, motions slow and line-broadening occurs. The glass transition temperature is $\approx 580^{\circ}C$ for $Na_2Si_4O_9$.

meric flow of the structural units, torsional rotation and vibration, or bond breaking and reformation motions (e.g. ring opening and closing, or reactions between silicate units).

The viscosity of the silicate melts varies in a non-Arrhenian manner with temperature and composition over six orders of magnitude. In general, aluminosilicates have a larger coefficient of viscosity than do binary alkali silicate liquids. The order of viscosity also depends on the polymerization state (Q^n) of the melt. The compositions investigated by high temperature NMR, in order of increasing liquid viscosity, are: Na_2SiO_3, $Na_2Si_2O_5$, $NaKSi_2O_5$, $Na_2Si_4O_9$, R-15, and $NaAlSi_2O_6$. The less viscous melts are observed to have narrower linewidths, indicating the presence of faster molecular motions, than more polymerized silicate liquids at the same temperature.

VI.1.1. ^{29}Si Chemical Shift

In crystalline aluminosilicates, $\delta(^{29}Si)$ primarily depends on the silicate polymerization state (Chapter IV). The same trend has been observed in aluminosilicate glasses (Chapter V). In a melt, motions occur which may change the silicate speciation, as described by Equation (45) in Chapter III and evidenced in silicate glass spectra (Chapter V).

In liquid silicates, $\delta(^{29}Si)$ changes linearly with Q^n speciation, as expected from data on the corresponding crystalline and glass silicates (Figure 34). Liquids which are more polymerized (higher average Q^n number) have lower resonance frequencies (more negative δ values and are more chemically shielded). Substitution of aluminum
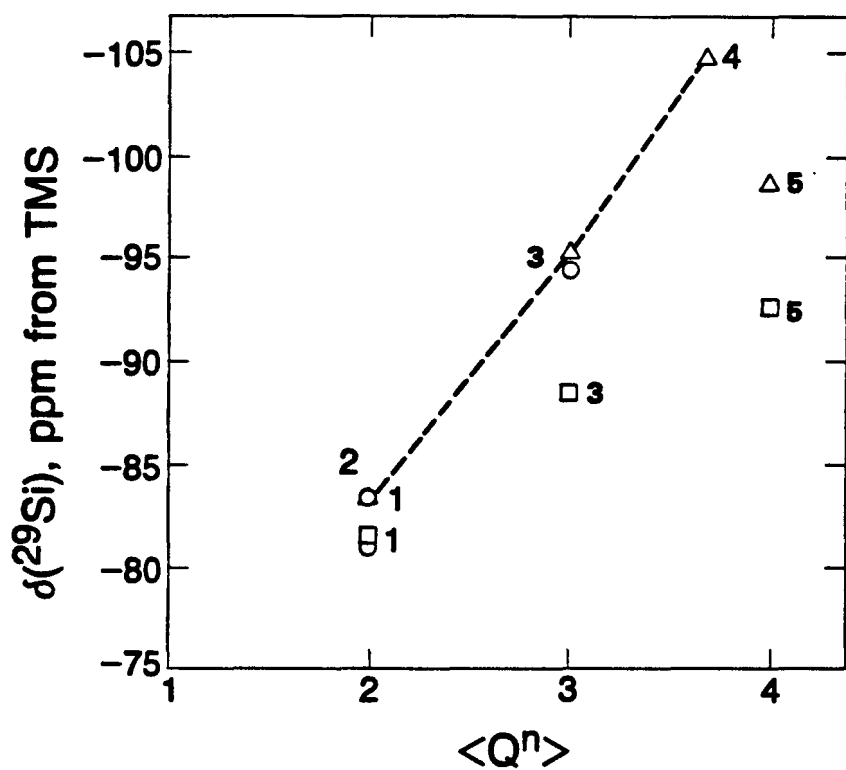
XBL 8511-11530

Figure 34: Isotropic ^{29}Si chemical shifts for molten, glass, and crystalline silicates as a function of average Q^n composition. Silicate liquids which are more polymerized have lower resonance frequencies (more negative $\delta(^{29}Si)$) as expected from data on crystalline materials. [1, crystalline and glass $MgSiO_3$; 2, molten Na_2SiO_3; 3, crystalline, glass, and liquid $Na_2Si_2O_5$; 4, molten $Na_2Si_4O_9$ (high temperature); 5, liquid and glass jadeite. (○, crystalline; □, glass; △, liquid.)]

atoms for silicon atoms reduces the chemical shielding, as shown for
$NaAlSi_2O_6$ and R-15. Silicon chemical shifts in the liquids are sys-
tematically less negative (less shielded) than in the corresponding
glass and crystalline state (Figure 34). The offset is $\approx$ 5 ppm.
This difference in chemical shift could result from several sources:
a bonefide difference in electronic environments between a glass and
the corresponding melt; a ^{29}Si chemical shift calibration inaccur-
acy; or a small dependence of the magnetic susceptibility on temper-
ature for ^{29}Si.

VI.1.ii. Chemical Exchange

In NMR spectroscopy, chemical exchange consists of spins chan-
ging from one environment to another at an exchange frequency, Ω
$\propto \tau_c^{-1}$. The form of the lineshape resulting from the motion of the
spins is determined by two parameters, Ω and Δ (the frequency sep-
aration between the different sites). Figure 35 contains an example
of one spin undergoing two site exchange. Significantly different
spectral features are obtained as the ratio of Ω to Δ is changed.
In the region of slow exchange, $\Omega << \Delta$, the two sites are fully
resolved (two narrow lines, separated by frequency Δ, are observed).
The lines are broadened by the average time the spin spends in each
site (lifetime broadening, $\approx \Omega$). As the rate of exchange increases
(e.g. the temperature is increased), the lines broaden and move
toward each other, and eventually coalesce into one broad line (Ω
$\approx \Delta$. As the exchange frequency continues to increase, the line
narrows. In the limit of fast exchange (the jumping frequency, Ω,
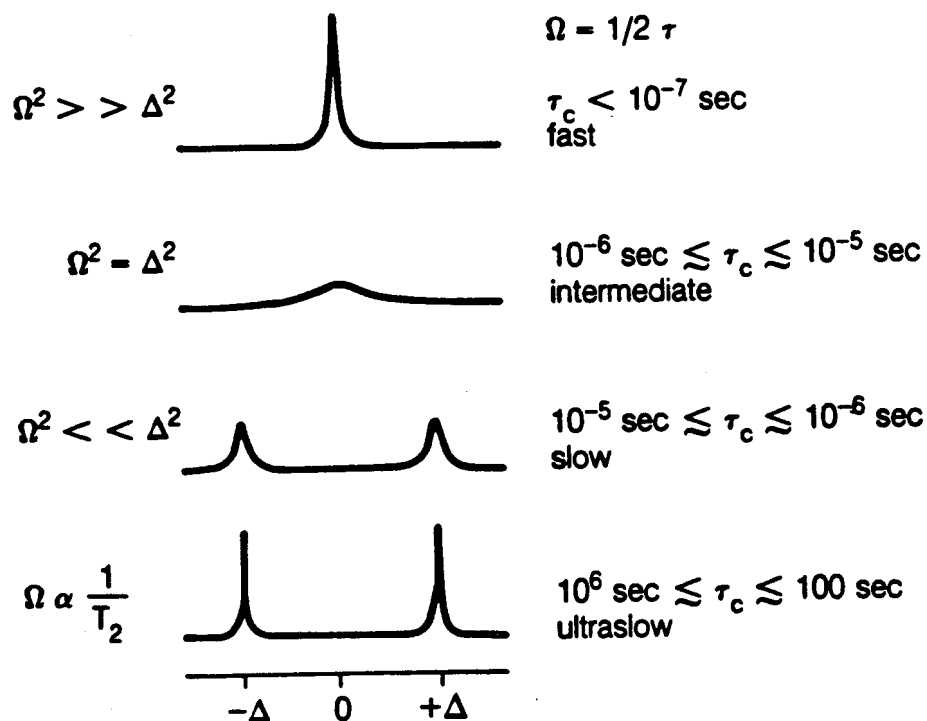
XBL 857-10632

Figure 35: Two site chemical exchange. (lower) When the exchange frequency, $\Omega \propto \tau_c^{-1}$, is much slower than the frequency separation between the two sites, Δ, two narrow lines are observed. As the exchange rate increases, the two lines broaden and begin to move toward each other. For $\Omega \approx \Delta$, one broad line is observed. (upper) As the exchange rate is further increased, one narrow line appears at the average frequency of the sites.

is much greater than the separation between the two resonance lines, Δ) a time averaged spectrum is observed. One line, of exchange narrowed width,[26]

$$\delta\omega \approx (\Delta)^2 / \Omega \ , \tag{57}$$

is located at an average frequency determined by the relative lifetime and populations of the two sites.

In the most viscous melt examined by high temperature ^{29}Si NMR ($Na_2Si_4O_9$), the narrow Lorenztian resonance line is observed to broaden and separate into two peaks as temperature is decreased (Figure 36). The presence of two resonance lines was observed at temperatures as low as 606^oC, which is very near T_g for $Na_2Si_4O_9$ ($\approx 580^oC$). At 606^oC the separation between the two peaks is about 20 ppm. Several possible explanations for this phenomena have been proposed. A phase separation of the melt into two immiscible liquids or mixtures of liquids and small crystallites is one possibility. The coupling of chemical shielding anisotropy to chemical exchange is another probable cause. Phase separation of the liquid $Na_2Si_4O_9$ sample has been eliminated because thermodynamically, only a very small amount of Q^3 species would form and the ^{29}Si MAS NMR spectrum of the single phase glass indicates that two chemically inequivalent sites exist (Chapter V) in almost equal proportions. ($\delta(^{29}Si$ of the two sites are separated by 14 ppm in the glass; the Q^3 site is axially symmetric with $\Delta\sigma \approx 100$ ppm and the Q^4 site has $\Delta\sigma$ estimated to be 0-20 ppm.)

The proposed explanation of the liquid $Na_2Si_4O_9$ spectral changes

Figure 36: Static ^{29}Si NMR spectra of isotopically enriched liquid

$Na_2Si_4O_9$ as a function of temperature. (bottom) At high

temperatures (828°C), molecular motions are rapid and one

narrow, symmetric ^{29}Si resonance line is observed.

(middle) As the temperature is decreased (695°C), the

line broadens and becomes asymmetric. (top) At temper-

atures slightly above the glass transition (606°C,

T_g ≈ 580°C), two silicon sites are apparent. The species

at the lower frequency (δ ≈ -107.7 ppm) is attributed to

a Q^4 species, as observed in the glass. The silicon site

with peak maximum at δ ≈ -86.5 ppm is the $\sigma_\perp$ correspon-

ding to the CSA tensor of a Q^3 species.

$Na_2{}^{29}Si_4O_9$

$\delta(^{29}Si)$, ppm from TMS

138
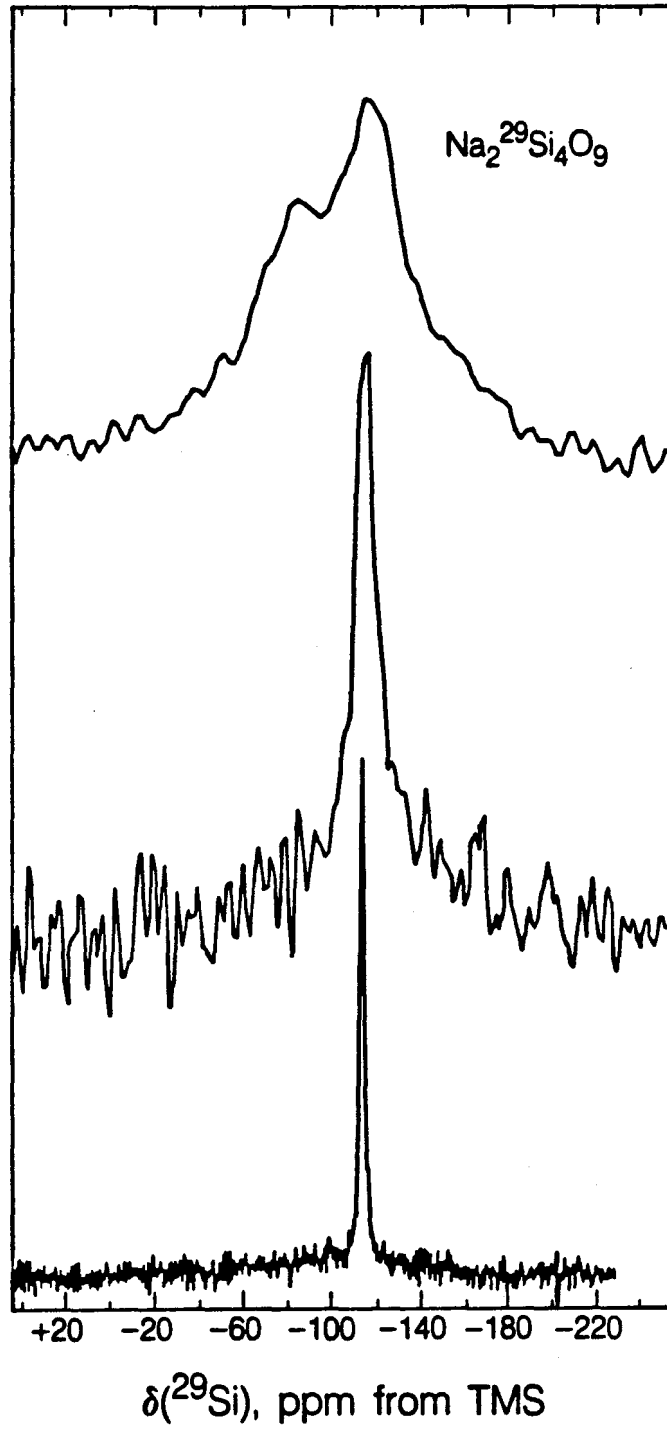
as a function of temperature, is that molecular motion has slowed suf-
ficiently such that the CSA tensor is no longer completely averaged
at temperatures between 700 and 800°C, and that below 700°C chemical
exchange (bond breaking and reformation rotations) slows to yield
two chemically inequivalent Q^n species.

VI.2. ^{23}Na Measurements

For all sodium aluminosilicates observed, the molten ^{23}Na spec-
trum is composed of one narrow, symmetric Lorentzian line. The single
resonance line broadens as temperature is decreased and the viscosity
of the melt increases (Figure 37). The one, fairly narrow line obser-
ved for this quadrupole nucleus allows an accurate isotropic chemical
shift to be assigned. Measurements on solid and molten NaCl indicate
that no temperature dependence is found for the ^{23}Na chemical shift.

Sodium, a spin 3/2 nucleus, presumably diffuses through the melt
as an ion. This motion must occur rapidly, such that the effects of
the quadrupole coupling is averaged away ($e^2qQ/h \approx 300$ kHz for
$NaNO_3$).[162,163] Relaxation times (a method of determining the rate of
motion), have been measured as a function of temperature, and are
discussed in detail in Chapter VII.

In the molten sodium (and mixed alkali) silicates examined,
$\delta(^{23}$Na) was observed to be independent of chemical composition. How-
ever, in the aluminosilicates examined, molten R-15 and $NaAlSi_2O_6$,
and crystalline albite ($NaAlSi_3O_8$), a linear dependence of chemical
shift on the ratio of O/Na has been found (Figure 38). The differ-
ence in the compositional dependence implies that the electronic
environments for the charge balancing sodium cations in aluminosili-

Figure 37: ^{23}Na linewidth as a function of temperature. As the tem-
perature is decreased, the melt viscosity increases,
motions slow, and the linewidth increases. The less vis-
cous melts are observed to have narrower linewidths,
indicating the presence of faster molecular motions, than
more polymerized silicate liquids at the same temperature.
($+$ Na_2SiO_3; O $Na_2Si_2O_5$; ● $KNaSi_2O_5$; △ $Na_2Si_4O_9$;
and □ $NaAlSi_2O_6$).

+20

+15

+10

+5

0

−5

−10

−15

δ (^{23}Na), ppm from NaCl

0   1   2   3   4   5   6   7   8   9

O/Na, mole%
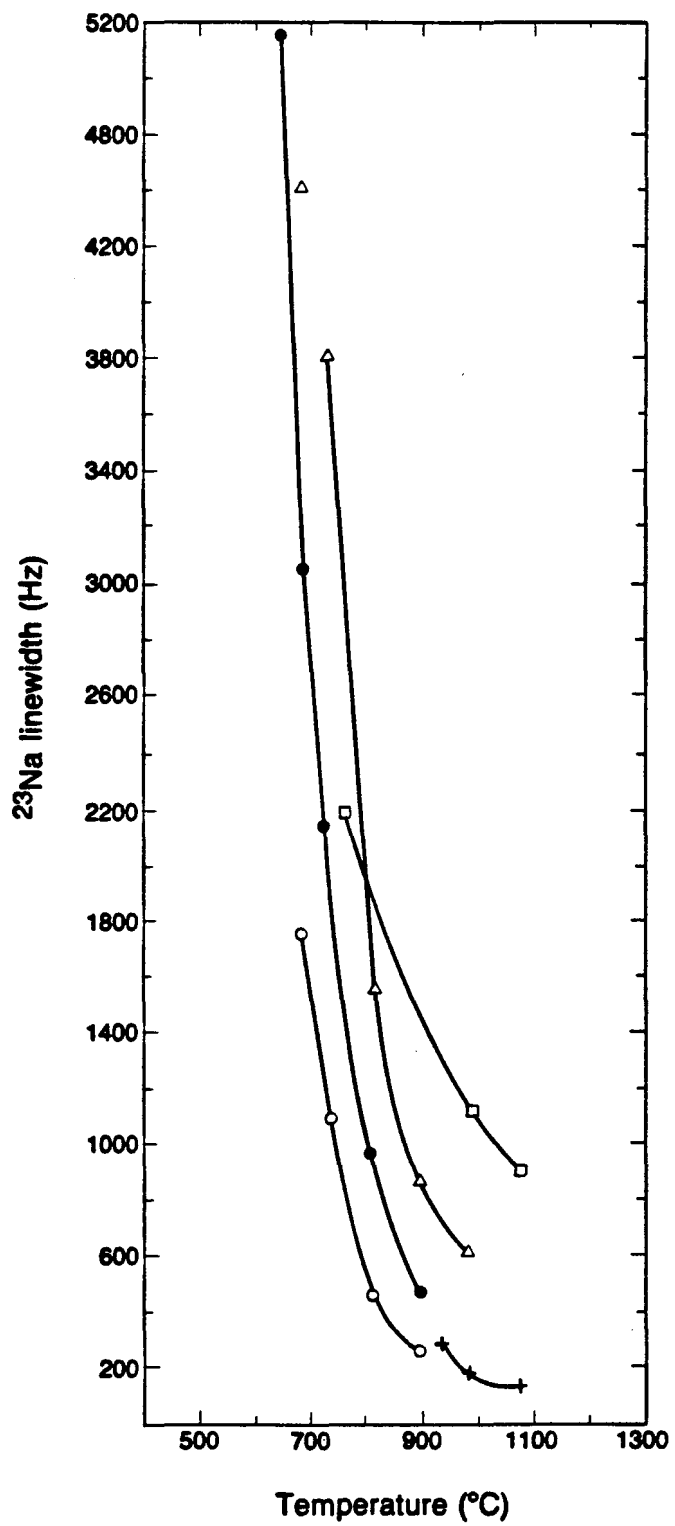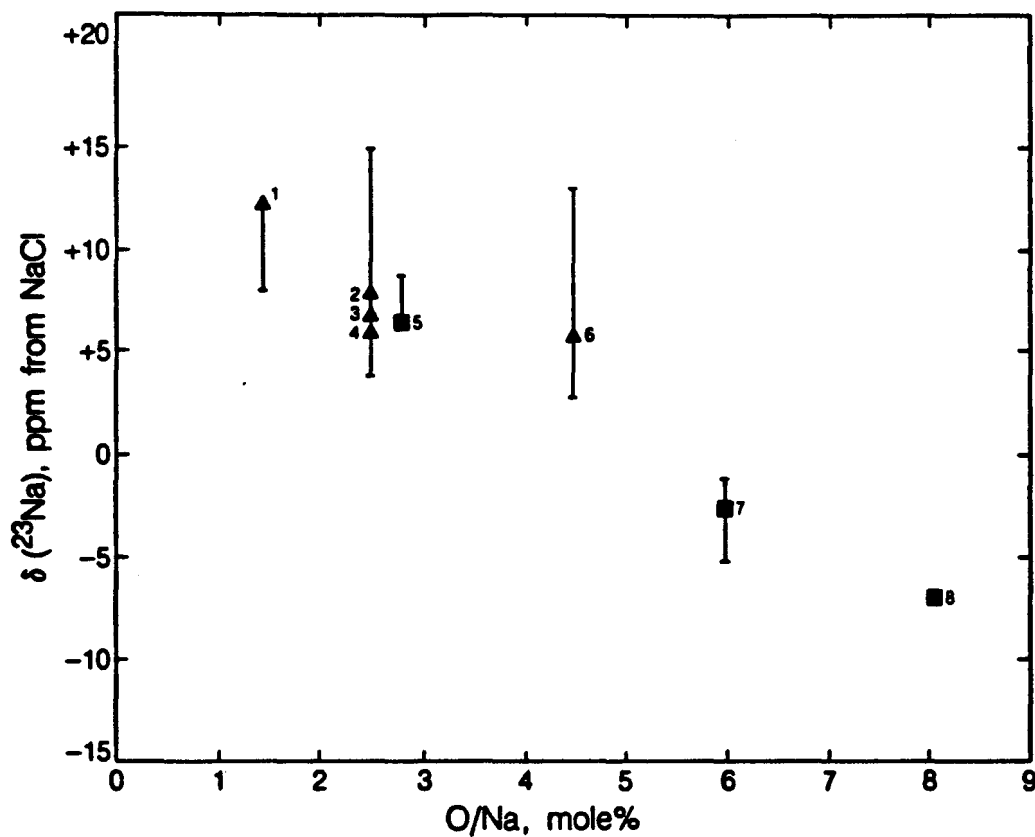
XBL 859-3803

Figure 38: Isotropic ^{23}Na chemical shifts, relative to 3M aqueous NaCl, as a function of composition for alkali silicates (▲) and sodium aluminosilicates (■). The lines shown are not error bars, instead they indicate the range of δ(^{23}Na) as a function of temperature. The error in chemical shift determination is within the size of the symbol. [1, molten Na_2SiO_3 (1070°C); 2, molten $Na_2Si_2O_5$ (803°C); 3, molten $NaKSi_2O_5$ (803°C); 4, molten $NaKSi_2O_5$ (803°C); 5, molten R-15 (892°C); 6, molten $Na_2Si_4O_9$ (803°C); 7, molten $NaAlSi_2O_6$ (981°C); 8, crystalline albite ($NaAlSi_3O_8$).]

cates differ from the sites in the sodium silicate melts observed. The compositional dependence of ^{23}Na chemical shifts in aluminosilicate melts is impossible to infer from the two data points collected, but some imaginable contributors are the ratio of number of oxygen atoms to the number of sodium atoms, the Si/Al ratio, or the silicate polymerization state. The last possibility is rather unlikely, as the sodium silicates observed also should be influenced by the melt polymerization state.

VI.3. ^{27}Al Measurements

In a melt, the role of aluminum atoms is unknown. In crystalline jadeite, aluminum occupies a network forming site as does silicon. At high temperatures or in a glass, it is unknown if aluminum atoms which were tetrahedrally coordinated in the crystalline form remain 4-coordinate, or whether they become 6-coordinate. ^{27}Al NMR should easily distinguish, on the basis of isotropic chemical shift, the type and quantity of occupied aluminum sites in molten aluminosilicates.

^{27}Al spectra of molten samples of $NaAlSi_2O_6$ and R-15 contain only a single, very broad featureless resonance absorption (about 20 kHz wide), centered at about 29 ± 20 ppm. If aluminum atoms occupy sites similar to those occupied by sodium atoms, then Al^{3+} diffuses rapidly thoughout the melt hence ^{27}Al relaxation times (and spectral appearance) should be similar to those of ^{23}Na. However, if aluminum atoms occupy sites similar to those of silicon atoms, then broad ^{27}Al lines could be caused by two sources: very rapid spin lattice relax-

relaxation (lifetime broadening); or, the aluminate tetrahedra undergo motions much slower than the electric quadrupole coupling (the size of which reflects the symmetry of the site). However, the role of aluminum atoms in silicate liquids can not be determined because $\delta(^{27}Al)$ cannot be accurately determined due to the breadth of the resonance.

VI.4. Relaxation Times

Nuclear spin relaxation meaurements are capable of determining the rate of molecular motion as well differentiating relaxation mechanisms which characterize the motion. When a spin system is subjected to rf radiation at the resonance frequency, a population distribution between the spin states is established such that the spin system and the lattice (everything except the nuclei under investigation) are no longer in thermal equilibrium. When the radiation is turned off, the condition of thermal equilibrium can then be restored. The rate at which the nuclear magnetization approaches its thermal equilibrium value is characterized by the spin-lattice relaxation time, T_1. The rate at which internal equilibrium between the spin system is established is controlled by the spin-spin relaxation time, T_2, via modulation of the nuclear spin energy levels. Both types of relaxation are caused by time dependent fluctuations of magnetic or electric fields at the nucleus and, these fluctuating fields arise from molecular motions.

Typically, only motions which occur on the relatively slow time-scale of magnetic resonance can be investigated. In liquids, rota-

tional and diffusional motions are important sources of relaxation. Spin relaxation measurements are also useful for investigating lattice vibrations in solids, collisions in gases, certain slow rotational or torsional motions within molecules, and some chemical exchange processes. Interactions which occur at a rate much faster than the nuclear resonance frequency ($\omega_0 \approx 10^8$ Hz) have little effect. Thus electronic motions and molecular vibrations are relatively unimportant sources of relaxation. On the other hand, any interaction which causes transitions between spin states and fluctuates near the resonance frequency strongly effects spin lattice relaxation and can contribute to broadening of the NMR line.

VI.4.i. T_1 Measurement

Pulse methods provide the simplest method for measuring T_1's over a wide range of values. The most commonly used technique is the 'inversion-recovery' $180^{\circ}_x - \tau - 90^{\circ}_x$ pulse sequence as illustrated in Figure 39. The inverted magnetization decays by pure spin-lattice relaxation, and the rate can be measured by plotting the magnetization as a function of delay time τ. To minimize pulse phase adjustment errors and improve the signal-to-noise ratio, phase cycling of the 90° detection pulse has been used along with the subsequent addition or subtraction of each FID to the accumulated signal. To optimize the excitation bandwidth, inversion pulse sequences which compensate for frequency offset (and if possible also for rf inhomogeneity) should be used in place of the 180° pulse for liquid samples. In solids, inversion sequences (such as $45_0 180_{90} 90_{180} 180_{90} 45_0$,[181]
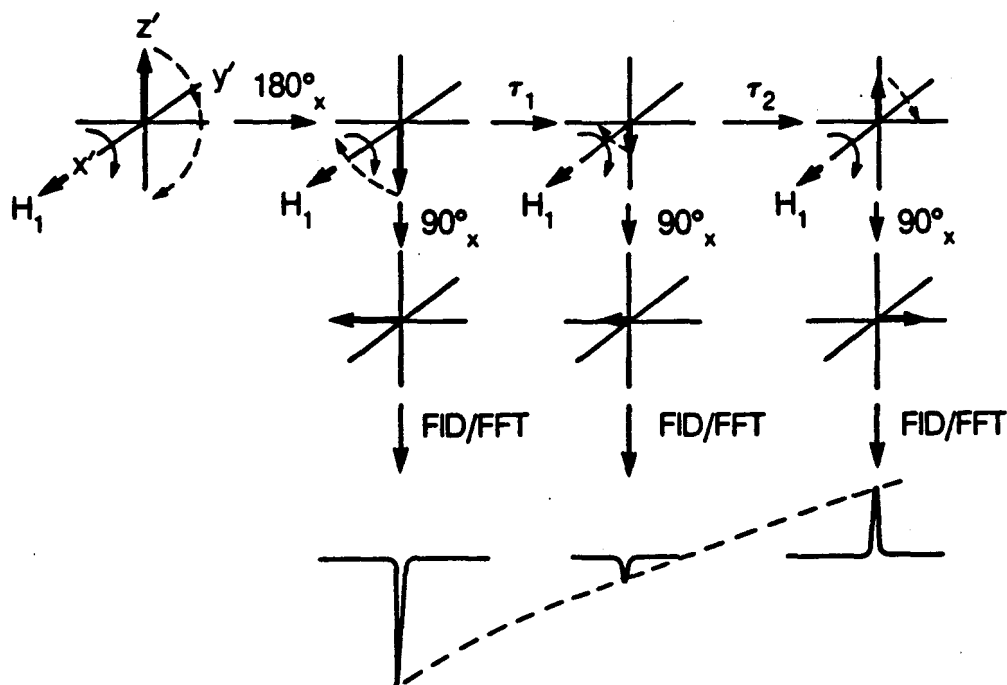
XBL 857-10635

Figure 39: Inversion recovery pulse sequence for T_1 determination.
First a 180° pulse inverts the total magnetization along
the -z axis. During the delay time, τ, spin-lattice
relaxation mechanisms allow some of the magnetization to
return to its equilibrium state. The $90°_x$ pulse then
allows detection of the magnetization remaining aligned
along the -z axis. After recording the FID, the spin
system is allowed to return completely to equilibrium
by waiting a delay period of at least 5 times T_1. The
sequence may then be repeated for different value of τ.

described in Appendix B) which compensate for quadrupolar or dipole-dipole interactions can be used.

Quantitatively, the rate of return to equilibrium of the M_z component of magnetization by spin lattice relaxation is given by the classical Bloch equations[2,6]

$$\frac{d}{dt} M(t) = - \frac{1}{T_1} [M(t) - M_o] \ . \tag{58}$$

For the inversion recovery technique, this first order differential equation has the solution

$$M_z(\tau) = M_o [1 - 2 \exp (-\tau/T_1)] \ , \tag{59}$$

where $M_o = M(\tau=\infty)$ is the equilibrium magnetization, and $M(\tau)$ is the residual magnetization remaining aligned along the z axis after a time τ. (It is assumed that all of the magnetization is inverted upon application of the 180° pulse.) In practice, it is easier to extract the value of T_1 if Equation (59) is rewritten in logarithmic form

$$\ln \left([M_o - M(\tau)]/(2M_o) \right) = - \tau/T_1 \tag{60}$$

and plotted. T_1 can be determined from the slope of the line or, less accurately by finding the τ value which causes $M(\tau) = 0$ and $\tau = T_1 \ln 2$.

VI.4.ii. T_2 Measurement

The spin-spin relaxation time, T_2, can be measured most accurately by use of the Hahn spin echo[19] (90°_x - τ - 180°_y - τ). The spin echo was first introduced to overcome the problem of broadening liquid resonance lines due to $\underline{H}_o$ inhomogenieties. For T_2 determination, phase cycling of the initial 90°_x pulse and subsequent FID addition or subtraction are utilized to improve the signal-to-noise ratio as in the T_1 experiments. The spin echo method for determining T_2 is limited by the rate of molecular diffusion which causes the nuclei to move from one part of the sample to another over the time of the experiment.

The spin echo consists of establishing a spin coherence via the 90° pulse, allowing the spin coherence (or spin isochromats) to dephase in the x-y plane via T_2 processes for a time τ. The 180° pulse refocuses the spin isochromats to give a 'Hahn echo' at a time τ after the 180° pulse. The echo amplitude depends on T_2, and the spin-spin relaxation time may be determined from a plot of echo amplitude as a function of 2τ.

The composite pulses used in a T_2 measurement sequence must be selected carefully, and phase coherence in the x-y plane is mandatory. Other pulse sequences such as the Carr-Purcell-Meiboom-Gill experiment[148,149] determine T_2 in a more time efficient manner than the conventional Hahn echo sequence, and in many instances, these sequences are the appropriate choice for measuring T_2.

Quantitatively, the loss of coherence by the spin isochromats due to T_2 processes are described by the Bloch equations.[2] Integra-

ting the appropriate equation gives

$$M(2\tau) = M_0 \exp(-2\tau/T_2) \ . \tag{61}$$

M_0 is the equilibrium magnetization, and $M(2\tau)$ is the magnetization remaining in the x-y plane (along the y axis) at a time 2τ after the initial 90° pulse. By plotting the logarithm of M versus delay time, 2τ, T_2 can be determined from the slope of the line. If the natural linewidth of the sample is much larger than the broadening introduced by inhomogeneities in the static external magnetic field, then T_2 can be determined merely by measuring the linewidth

$$T_2 = 1/\Delta\omega_{FWHM} \ , \tag{62}$$

where $\Delta\omega_{FWHM}$ is the linewidth at half intensity in units of angular frequency.

VI.4.iii.   Temperature Dependence of Relaxation Times

If relaxation times are assumed to obey an Arrhenius-type temperature response (i.e. thermally activated processes), then the temperature dependence of T_1 and T_2 can be described as follows.[4,26] For most liquids at high temperatures, motions are fast and the spin-lattice relaxation time is long and equal to the spin-spin relaxation time. As the temperature decreases, the liquid becomes more viscous and the relaxation times decrease linearly with inverse temperature. The graph of T_1 as a function of inverse temperature (or correlation time, as in Figure 40) has a minimum located at $\omega_0\tau_c = 1$. τ_c, the correlation time of the motion, is the mean residence time or the

average time between interstitial jumps and is inversely proportional to temperature. The minimum value of T_1 indicates that the energy exchange process with the lattice is most efficient when motions occur on a timescale the order of ω_0 (the Larmour frequency). The position of the T_1 minimum is dependent upon the static external field strength, with weaker fields (smaller Larmour frequencies) shifting the minimum to lower temperatures (longer correlation times).

As the temperature continues to decrease, the component of local field fluctuations at the resonance frequency decreases. If motions are less than ω_0, as in a solid, then the value of T_1 increases due to a decrease in energy exchange with the lattice. T_2, however, continues to linearly decrease until molecular motions freeze (the rigid lattice limit). At this stage, the material is a randomly oriented solid, and T_2 is temperature independent and dominated by the dipole-dipole relaxation process. In a solid $T_2 < T_1$, whereas in a liquid the two relaxation times are equal, $T_2 = T_1$.

The minimum value of T_1 depends not only on the magnitude of the magnetic field, but also on the molecular radius. (The molecular size determines the reorientation rate.) For mobile liquids where molecular reorientation is rapid and $\omega_0\tau_c \ll 1$ (the extreme narrowing or fast motion limit), T_2 becomes equal to T_1. If the relaxation mechanisms are plagued by anisotropic motion and are no longer describable by a single τ_c, the relaxation rate equations become very complicated. And, coupled correlation times can cause the T_1 to increase dramatically (e.g. the ^{13}C T_1 on a spinning methyl group is approximately nine times longer than the T_1 for a ^{13}C attached to the framework).

Figure 40:   Temperature dependence of T_1 and T_2 relaxation times. τ_c is the correlation time, or the average time between jumps, and is inversely proportional to temperature. The higher the temperature, the faster the motion, the shorter the correlation time, and the slower the spin relaxation. For a liquid, τ_c is short $\omega_0 \tau_c \ll 1$ and T_1 = T_2. As the liquid becomes more viscous, the correlation time increases. The result is that T_2 (inversely proportional to linewidth) decreases, although it is still proportional to $1/(2\tau_c)$. But T_1 now becomes very long, proportional to $2\tau_c/(1 + \omega_0^2 \tau_c^2)$. T_1 goes through a minimum at the point $\omega_0 \tau_c = 1$. The minimum value of T_1 indicates that energy exchange with the lattice is the most efficient when motion occurs at frequencies near the Larmour frequency, ω_0. As the temperature continues to decrease, the component of the local field fluctuations at the resonance frequency, ω_0, decreases, tending to zero when $\omega_0 \tau_c \gg 1$. This decrease in energy exchange causes the value of T_1 to increase, if motional frequencies are less than ω_0, as in a solid. The full linewidth at half-intensity (in angular frequency units) is $(\pi \times T_2)^{-1}$, and continues to increase linearly with τ_c until the molecular motion becomes completely frozen. At this stage, the sample is a randomly oriented solid, and line broadening is caused by dipole-dipole interactions.
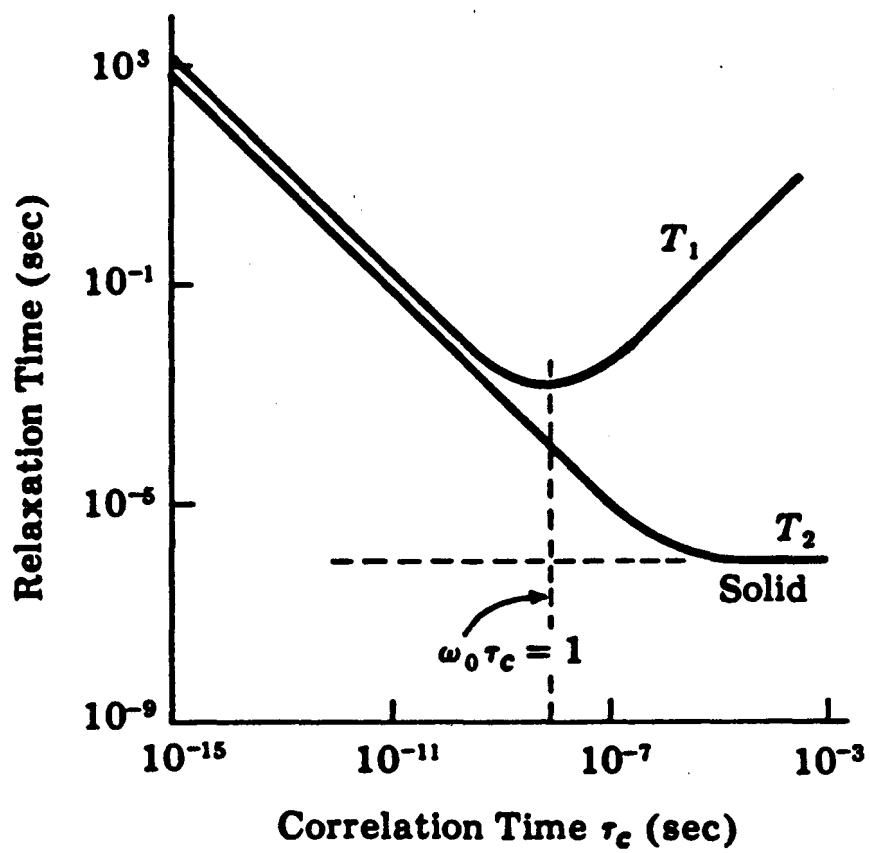
If τ_c follows an Arrhenius-type rate law, then an activation energy, E_a, can be extracted from the slope of both the high and low temperature regions of the relaxation time versus correlation time plot.

VI.5. Relaxation Mechanisms

Important relaxation mechanisms include magnetic dipole-dipole interactions between nuclei, fluctuating local fields caused by the anisotropic chemical shift tensor in a tumbling molecule, coupling of nuclear spins (dipole-dipole) to magnetic fields caused by molecular rotations, interactions between nuclear quadrupole moments and electric field gradients which may change during molecular motion, and strong magnetic fields due to unpaired electrons present as paramagnetic impurities. Only the mechanisms which possibly apply to silicate melts will be examined. For additional information and references, R.K. Harris[27] (Chapter 3), D. Shaw[40] (Chapter 9), are good starting points as are review articles by J.R. Lyerla and G.C. Levy[159] and J.M. Chezeau and J.H. Strange.[164] A thorough treatment of most relaxation mechanisms can be found in A. Abragam.[6]

The observed relaxation time is the sum of all the relaxation times from the various mechanisms. Each relaxation mechanism can give different chemical information, consequently, the contribution of each mechanism must be resolved. Using relaxation rates $(R_1=T_1^{-1})$ it is frequently possible to differentiate between contributions from different relaxation mechanisms, by varying ω_0 or temperature. Several contributions can be simply distinguished only in the fast exchange limit $(T_1 \approx T_2)$.

VI.5.I. Correlation Times

A useful way of describing molecular motion is in terms of a correlation time. τ_c is defined as the average time between molecular collisions for translational motion, or the average time for a molecule to rotate by one radian for reorientational motion.[40] The correlation time of a molecule in a liquid will depend on many factors, such as molecular size, symmetry, and liquid viscosity. Molecular size and symmetry effect τ_c by causing disordering of the solvent upon rotation or translation. Smaller or more symmetric molecules will move faster than larger or more asymmetric molecules. Viscosity describes the ease with which reordering of the solution can be achieved. τ_c can be related to viscosity (η) for a hard sphere of radius, a, by the Debye theory of liquids[6,40,156]

$$\tau_c = \frac{12 \pi \eta a^3}{k T} \tag{63}$$

where k is the Boltzmann constant and T is the absolute temperature.

VI.5.II. ^{29}Si Relaxation Mechanisms

Natural abundance ^{29}Si interactions are intramolecular in origin and should be uncomplicated by homonuclear spin couplings. Isotopically enriched ^{29}Si (95%), however, has been used to enhance sensitivity of the melt experiments. Because homonuclear dipole-dipole interactions are inversely proportional to the cube of the distance between spin pairs, this relaxation mechanism, in the fast motion limit, is proportional to r^{-6}. However, ^{29}Si pairs separated by an

oxygen atom have an average Si-Si bond distance of 3 Å, and a maximum ^{29}Si-^{29}Si dipole-dipole coupling $|D(^{29}Si$-$^{29}Si)|$ of ~ 250 Hz. This small coupling is easily averaged away, hence analysis of 95% enriched ^{29}Si relaxation time data should parallel that of natural abundance ^{13}C data (in the absence of proton couplings).

The motions silicate units are assumed to undergo in a melt are those of viscous flow and molecular rotation, both of which require breakage and reformation of Si-O-Si or Si-O-Al bonds. Relaxation mechanisms of importance to ^{29}Si in molten aluminosilicates are nuclear dipole-dipole (very small contributions) and chemical shielding anisotropy (which may be large, $\Delta\sigma$ ~ 3.5 kHz).

VI.5.11.a. Nuclear Dipole-Dipole Relaxation Mechanism

Dipole-dipole interactions in liquids and solids may be modulated by molecular tumbling or translational diffusion, thus causing relaxation. Assuming a dipolar mechanism for relaxation in the high field limit, and a single molecular reorientation characterized by one temperature dependent correlation time τ_c, the intramolecular homonuclear dipole relaxation (in the extreme narrowing limit) for a pair of spin 1/2 nuclei separated by a distance r is[27]

$$T_1^{-1} = (\mu_0 /4 \pi)^2 \, 3/2 \, \gamma_I^4 \, \hbar^2 \, \tau_c \, r^{-6} . \tag{64}$$

VI.5.II.c. Chemical Shift Anisotropy

The shielding at the nucleus, and hence the magnetic field seen by the nucleus varies with molecular orientation in the static external magnetic field $\underline{H}_o$. As the molecule tumbles or diffuses, the anisotropic term, $\underline{\sigma}'$, is equivalent to a fluctuating local field at the nucleus and can cause relaxation. In the fast motion regime (when τ_c is short), the spin lattice relaxation rate of a spin 1/2 nucleus is given by

$$T_1^{-1} = \frac{1}{15} [\sigma_{11}'^2 + \sigma_{22}'^2 + \sigma_{33}'^2] \, 2 \, \tau_c \ . \qquad (67)$$

The chemical shift anisotropy relaxation mechanism is unusual, in the fast motion regime the two relaxation times are not equal (T_1/T_2 = 7/6). Another characteristic feature of this mode of relaxation is that $1/T_1$ is proportional to H_o^2. This field dependence of the relaxation rate unfortunately has not been taken advantage of for characterizing the relaxation mechanisms in molten silicates.

VI.5.III. ^{23}Na Relaxation Mechanisms

In the sodium silicate melts observed, sodium is presumed to rapidly diffuse through the melt as an ion (Na^+). The local magnetic fields modulated by this diffusion probably are nuclear dipole-nuclear dipole coupling, translational diffusion, and the electric quadrupole gradient.

VI.5.iii.a. Nuclear Quadrupole Interaction

Quadrupole broadening is troublesome when attempting to analyze high resolution spectra. Not only is the quadrupole resonance broadened, but so are the lines from other nuclei which have spin-spin coupling to a quadrupole nucleus (e.g. ^{23}Na coupled to ^{29}Si).

In solutions or melts, rapid molecular tumbling and diffusion will reduce the quadrupolar interaction strength. If the motion is isotropic, only a single NMR absorption will be seen. However in most cases, the averaging is not sufficient to reduce the linewidth to that of a spin 1/2 nuclei undergoing rapid, isotropic motion. These broader lines found in solutions or melts for quadrupolar nuclei are caused by rapid modulation of spin energy levels, an additional mode of relaxation allowed for quadrupole nuclei. For isotropic motion (such as in a liquid), T_1 and T_2 are equal, and it has been shown[27]

$$T_{2Q}^{-1} = T_{1Q}^{-1} = 3/40 \ (2I + 3) \ I^{-2} \ (2I - 1)^{-1}$$
$$\cdot (e^2 qQ/h)^2 \ \tau_c \ [1 + 1/3 \ \eta^2] \ . \tag{68}$$

η is the asymmetry parameter and e^2qQ/h is the quadrupole coupling constant. If motion is not fast enough $(\omega_0^2 \tau_c^2 \gg 1)$, τ_c must be replaced by $\tau_c/(1 + \omega_0^2 \tau_c^2)$. The correlation time τ_c is that for molecular motion and is the same as used for dipolar relaxation. τ_c increases as viscosity increases and therefore as temperature decreases. The slower the molecular motion, the faster the spin relaxation.

Generally, quadrupolar relaxation is the dominant relaxation

mechanism for nuclei with spin greater than 1/2, and leads to line-widths substantially larger than those caused by other mechanisms. Spin 1/2 nuclei which have heteronuclear magnetic dipole-dipole couplings with quadrupole nuclei will also manifest linebroadening, decreased relaxation times, and possibly the appearance of spin multiplets which can be computed.[27]

VI.5.iii.b. Translational Diffusion

In the fast motion limit, the translational diffusion relaxation mechanism is independent of the strength of the magnetic field. Translational diffusion, however, is dependent upon both temperature and composition (viscosity), and the size of the diffusing particle.[6] For a spin 3/2 nucleus in the fast motion regime, the translational diffusion mechanism yields relaxation times[6]

$$T_1^{-1} = T_2^{-1} = 9/2 \ \pi^2 \ \gamma^4 \ \hbar^2 \ N \ \eta \ (kT)^{-1} \ . \tag{69}$$

N is the density of spins and k is the Boltzmann constant. Equation (69) depends upon the Stokes-Einstein correlation of solution viscosity with diffusion rate. The behavior of silicate melts is very difficult to characterize, however, sodium diffusion is known to be non-Arrhenian and cannot be accurately described by this equation.

VI.6. High Temperature Relaxation Time Measurements

Experimental ^{29}Si and ^{23}Na relaxation times, T_1 and T_2, have been measured for several sodium aluminosilicate compositions over a temperature range above their respective glass transition tempera-

tures, T_g. Two different series of experiments were performed, one in July 1984, the other in December 1984. The sample temperature is known less precisely for the July set of experiments, and the $\underline{H}_o$ homogeneity is inferior to the series of experiments performed in December.

VI.6.1. ^{29}Si

As previously stated, 95% isotopically enriched ^{29}Si samples were used to obtain high temperature spectra and relaxation times. In July 1984, ^{29}Si relaxation data consisted primarily of T_2^* measurements as a function of temperature. The majority of the T_2^* values occured below the instrumental limit of $\underline{H}_o$ inhomogeneity (< 200 Hz) and are of little analytical value.[103] In December 1984, the linewidth imposed by $\underline{H}_o$ inhomogeneities was reduced to 45 Hz.

During the second period of experimental activity, ^{29}Si T_1 and T_2 measurements were collected only for molten $Na_2Si_4O_9$ over a very limited temperature range (Figure 41, T_2 values calculated from the linewidth have also been included). The ^{29}Si T_2 appears to be larger than T_1. Physically, this cannot occur, however it can be used to estimate the experimental error in ^{29}Si relaxation time determination (± 5 msec). This uncertainty is rather large, possibly due to changes in experimental conditions during the long averaging cycles necessary to acquire the data. Because the motions undergone by the ^{29}Si nuclei are expected to be slower than the Larmour frequency (for $H_o \approx 42$ kG, $\omega_o \approx 35.5$ MHz), the fast motion limit is not valid.

The two observed ^{29}Si T_1 values can be used to calculated an
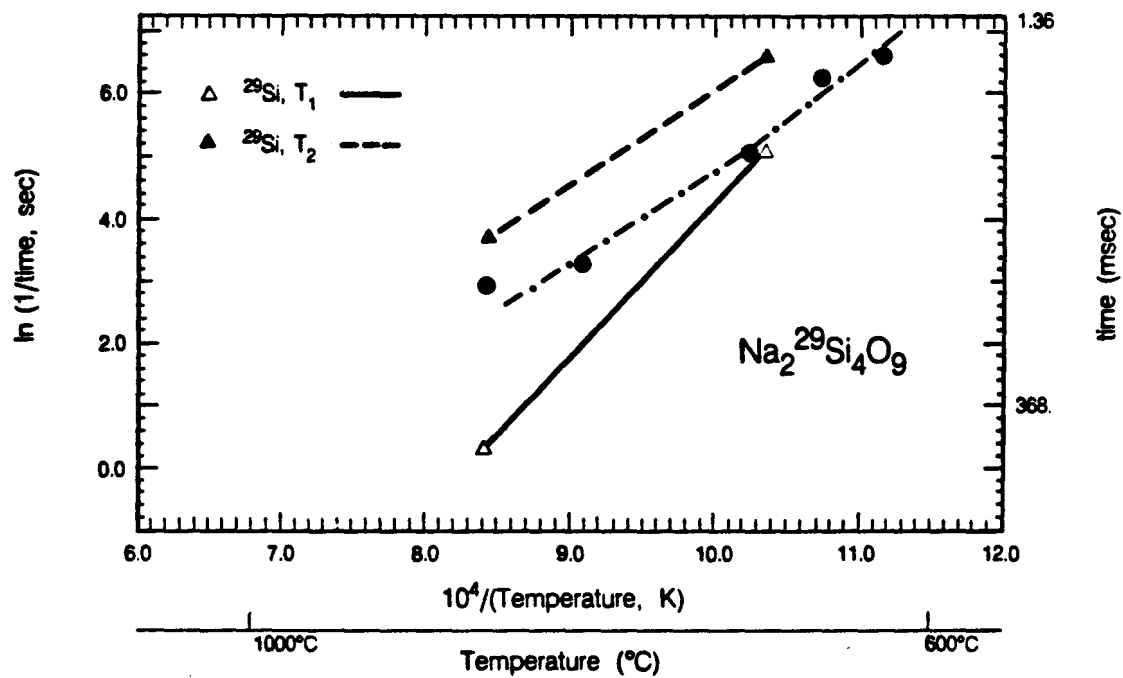
Figure 41: ^{29}Si relaxation in molten $Na_2^{29}Si_4O_9$. $\triangle$, $\blacktriangle$ correspond to T_1 and T_2 measurements using the inversion recovery and Hahn spin echo techniques, respectively. $\bullet$ represent T_2 measurements calculated from the linewidth.

activation energy of 205.2 kJ/mole (the slope of ln T_1^{-1} plotted versus inverse temperature) for relaxation (or some type of viscous flow process). From ^{29}Si MAS NMR spectra of $Na_2Si_4O_9$ glass, it is known that two chemically different silicate species exist (Q^3 and Q^4, Chapter V.3.ii). The difference in isotropic ^{29}Si chemical shift between the two species is ≈ 14 ppm, the chemical shielding anisotropy is ≈ 3.5 kHz for the Q^3 site and is estimated to be ≈ 0-0.7 kHz for the Q^4 site. At high temperatures, one narrow (1-3 ppm) ^{29}Si line with a symmetric Lorentzian lineshape is observed for sodium tetra-silicate. The narrow high temperature linewidth indicates that motion of the silicate units is fast enough to average the effects of the Q^3 chemical shift anisotropy ($\Delta\sigma$ ≈ 3.5 kHz). However, the presence of only one ^{29}Si resonance absorption at high temperatures is also indicative of chemical exchange occuring on a timescale faster than the chemical shift separation of the two sites (≈ 500 Hz).

VI.6.ii. ^{23}Na

^{23}Na relaxation times have been measured for several compositions over much larger temperature ranges than for ^{29}Si. The graphs of ln T_1^{-1} and ln T_2^{-1} versus inverse temperature usually have the same qualitative appearance (linear dependence on temperature) for all compositions investigated. Activation energies for relaxation have been calculated from the high temperature portion of the relaxation time versus temperature plots (Table 6). In general, the ^{23}Na T_1 ≈ T_2 in molten silicates, hence the high temperature approximation is valid. In $NaKSi_2O_5$, the data suggests that a T_1 minimum is located

near 630°C. (Na$_2$Si$_2$O$_5$ and jadeite also exhibit possible T$_1$ minima near 700°C and 850°C, respectively). For these compositions, the fast motion limit is probably valid for the relaxation measurements taken at temperatures above the minimum. Figures 42 through 45 con-contain measured T$_1$ and T$_2$ relaxation times, T$_2$ from linewidth measurements, and the calculated T$_1$ component of translational diffusion plotted as a function of inverse temperature.

In a melt, sodium (the network modifying cation) is presumed to undergo rapid translational diffusion as an ion. Na$^+$ diffusion is expected to be responsible for electrical conductivity in molten silicate materials. However, the calculation of T$_1$ due to translational diffusion is not straight forward as no model exists for this process.

The Na$_2$SiO$_3$ (sodium metasilicate) sample (Figure 42) crystal-lized sometime during the experiment. Because the sample is poly-crystalline, the Na$^+$ ions are no longer free to diffuse throughout the melt. In a solid, the Na$^+$ ions are presumed to be trapped in cages composed of silicate tetrahedra, although some type of dif-fusion could still be possible. At elevated temperatures, the Na$^+$ ions must be moving very rapidly throughout the limited space of their cages. The motion serves to average $\mathcal{H}_Q$, resulting in the narrow, melt-like spectra observed for NaSiO$_3$. If the predominant relaxation mechanism is modulation of the quadrupolar interaction, then Equation (68) is applicable (T$_1 \approx$ T$_2$, hence the fast motion limit is valid). The slope of T$_1^{-1}$ versus inverse temperature is directly related to the correlation time. Assume the quadrupole

Table 6: Activation energies for relaxation in aluminosilicate

  melts.

Composition	Nucleus	Type of Relaxation	E_a (kJ/mole)
$Na_2Si_4O_9$	^{29}Si	T_1	205.2[+]
$Na_2Si_4O_9$	^{29}Si	T_2	125.8[+]
$Na_2Si_4O_9$	^{29}Si	T_2*	115.1
$Na_2Si_4O_9$	^{23}Na	T_1	65.7
$Na_2Si_4O_9$	^{23}Na	T_2	60.7
Na_2SiO_3[†]	^{23}Na	T_1	15.6
Na_2SiO_3[†]	^{23}Na	T_2	8.1
$Na_2Si_2O_5$	^{23}Na	T_1	109.5[‡]
$KNaSi_2O_5$	^{23}Na	T_1	90.5
$KNaSi_2O_5$	^{23}Na	T_2	64.9
$NaAlSi_2O_6$	^{23}Na	T_1	75.0
$NaAlSi_2O_6$	^{23}Na	T_2	103.0

[+] Activation energy is calculated from only two data points.

[†] Na_2SiO_3 was probably crystalline.

[‡] Activation energy for ^{23}Na spin lattice relaxation was calculated from the three highest temperature data points.
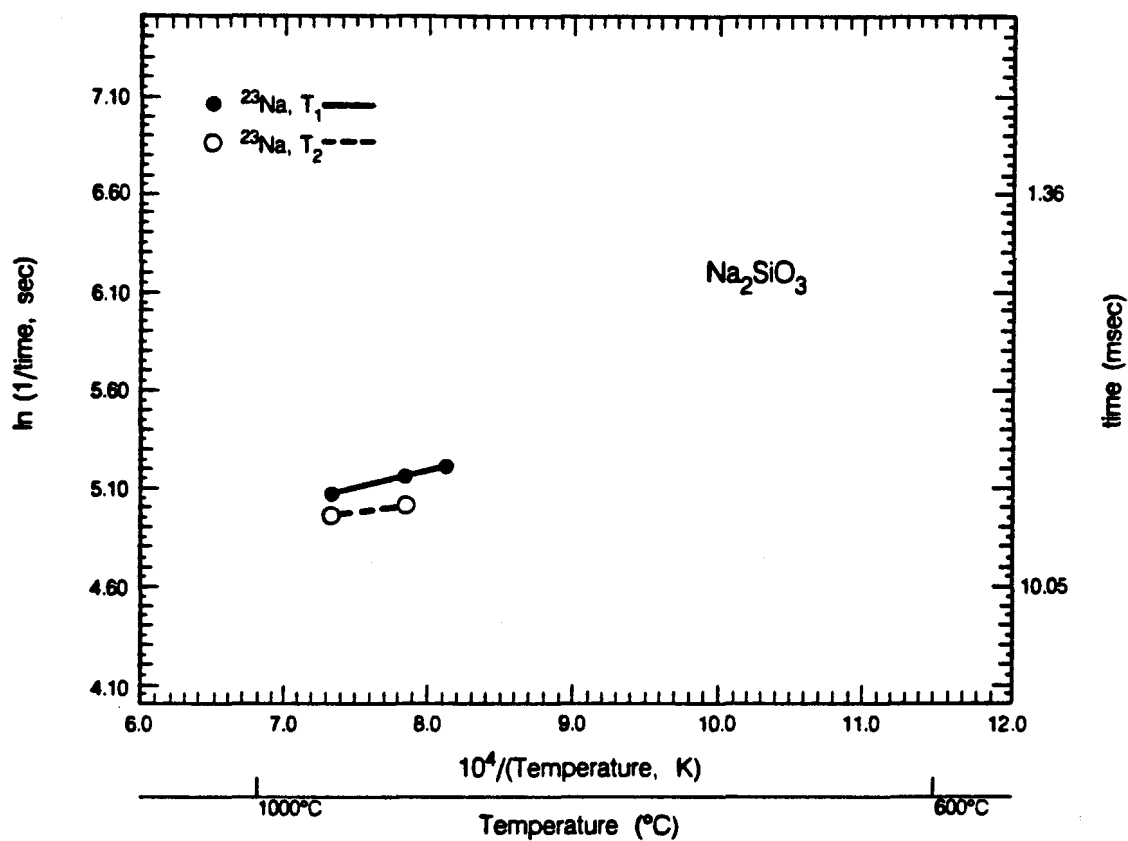
Figure 42: ^{23}Na relaxation in polycrystalline Na_2SiO_3. ● and ○ .correspond to T_1 and T_2 measurements using the inversion recovery and Hahn spin echo techniques, respectively.

Figure 43: ^{23}Na relaxation in molten $Na_2Si_2O_5$ (top) and $NaKSi_2O_5$

(bottom). ● and ○ correspond to T_1 and T_2 measurements

using the inversion recovery and Hahn spin echo techni-
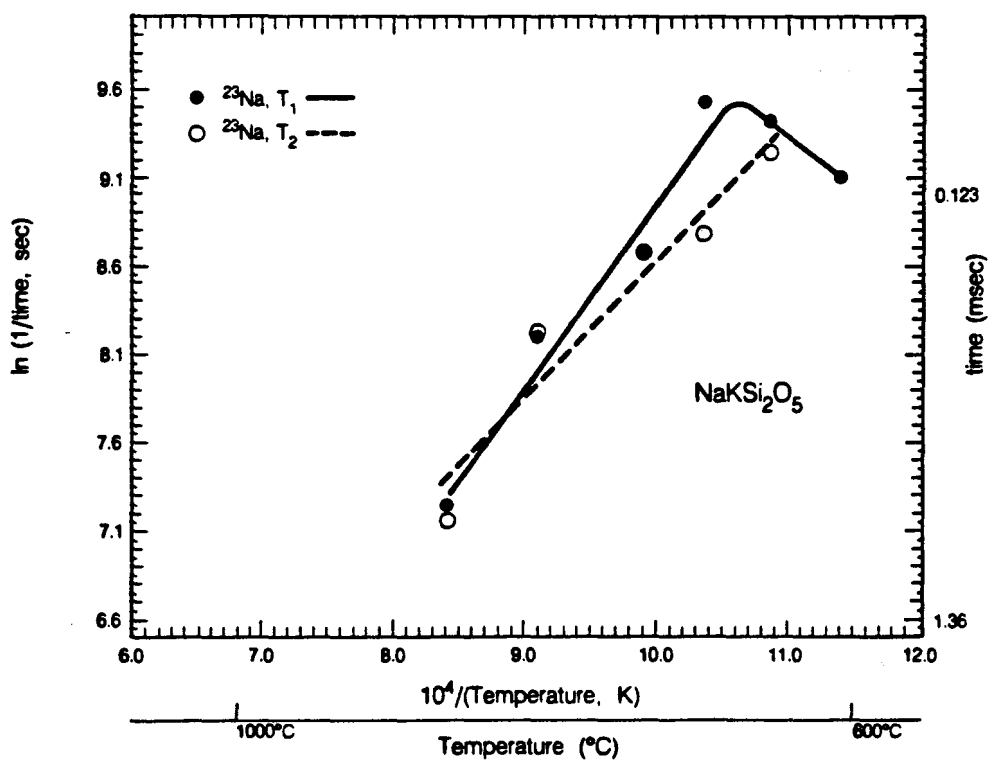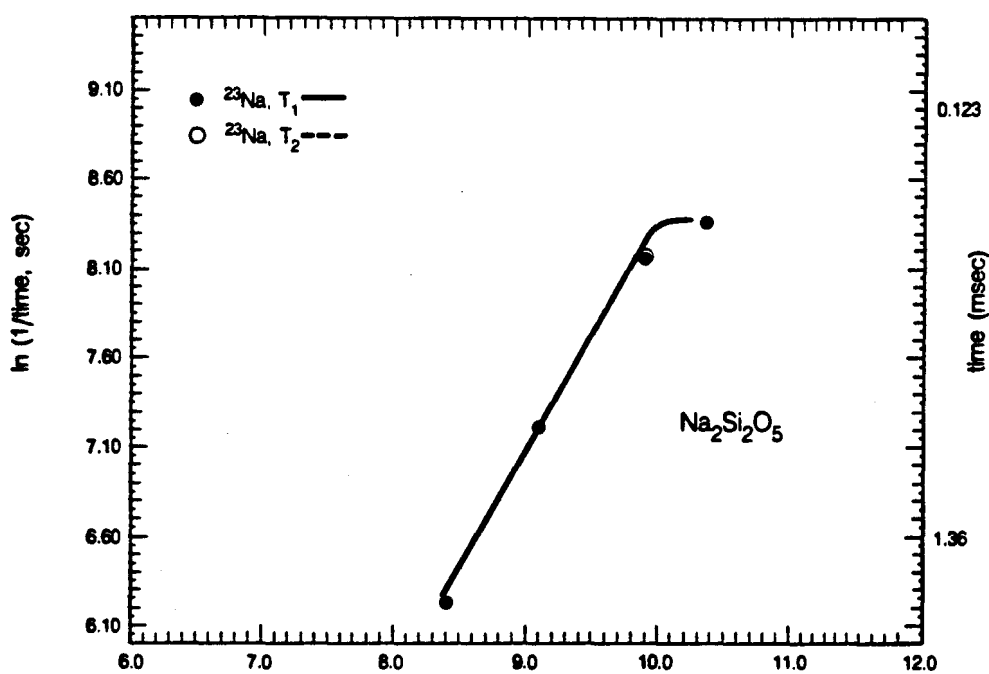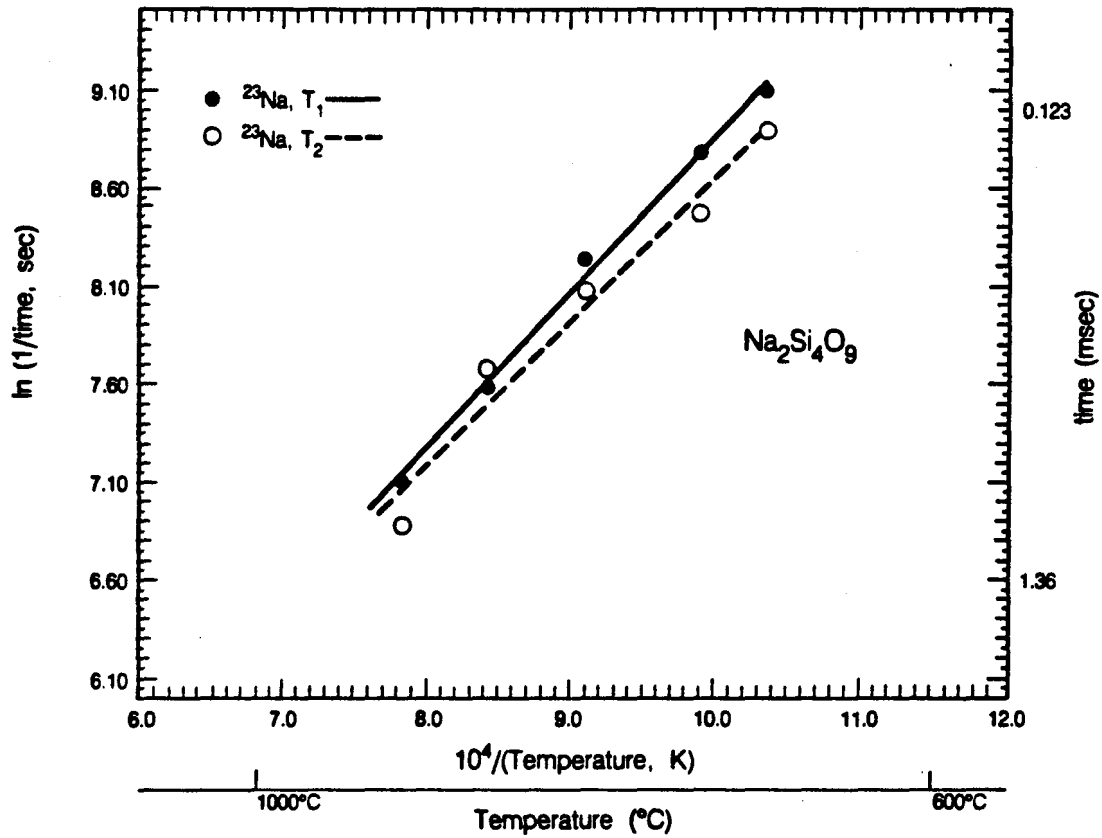
Figure 44: ^{23}Na relaxation in molten $Na_2Si_4O_9$. ● and ○ correspond to T_1 and T_2 measurements using the inversion recovery and Hahn spin echo techniques, respectively.
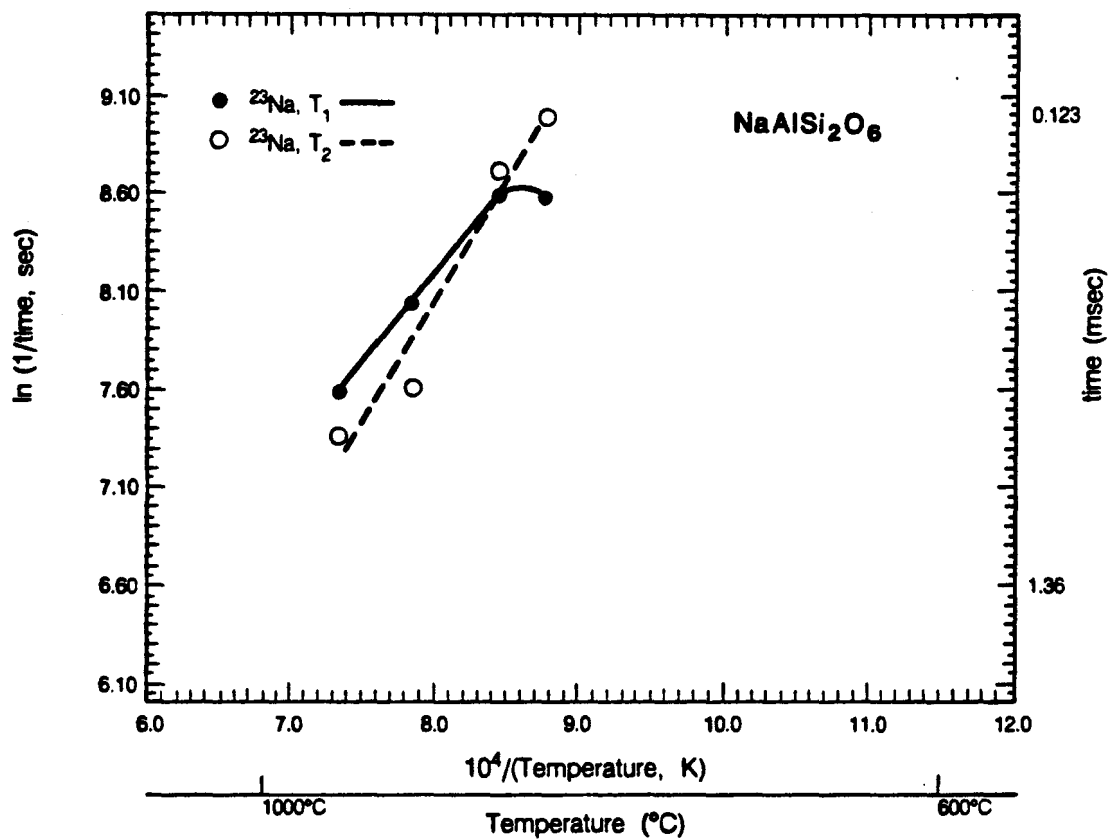
Figure 45: ^{23}Na relaxation in molten NaAlSi$_2$O$_6$. ● and ○ corres-
pond to T$_1$ and T$_2$ measurements using the inversion
recovery and Hahn spin echo techniques, respectively.

asymmetry parameter to be zero (because it is unknown and will not effect this order of magnitude calculation by more than 30%), and estimate the quadrupole coupling constant, e^2qQ/h, to be the same as in $NaNO_3$ (0.3 MHz),[162,163] then the correlation time of Na^+ diffusion can be calculated as a function of temperature from

$$\tau_c = 10 \text{ slope } T(K)^{-1} (e^2qQ/h)^{-2} .$$ (72)

The [23]Na T_1 and T_2 relaxation rates have a slope of 3.15×10^5 K/sec and 1.71×10^5 K/sec, respectively. For the temperature range 1234 K $< T(K) <$ 1368 K, the correlation times are (T_1) 3.2×10^{-8} sec $> \tau_c >$ 2.8×10^{-8} sec and (T_2) 1.5×10^{-7} sec $> \tau_c >$ 1.4×10^{-7} sec. The calculated correlation times are reasonable estimates for the time-scale of sodium motion at high temperature since the high temperature limit is valid ($\omega_0 \tau_c > 1$), hence $\tau_c < 2 \times 10^{-8}$ seconds.

VI.7. Conclusions

At temperatures several hundred degrees above the glass transition temperature (Tg), one narrow, Lorentzian line was observed in the ^{23}Na and ^{29}Si NMR spectra of silicate liquids. The ^{27}Al NMR spectra, however, were very broad and featureless. The observed linewidths (full width at half maximum, or FWHM) at the highest temperatures, for both [23]Na and [29]Si, are quite narrow (60-350 Hz or 1-10 ppm). The narrow, symmetrical Lorentzian lineshapes are indicative of molecular motions occuring at or above the kHz frequency range in silicate melts at high temperatures.

In a melt, the average silicon environment is approximately the

same as in the corresponding glass or crystalline material. However, the dynamic motions present are rapid enough to average out the details of silicate speciation in liquid aluminosilicates. Chemical exchange has been found to occur in the ^{29}Si NMR spectra of molten $Na_2Si_4O_9$ at temperatures near the glass transition. This is indicative of some type of equilibrium such as the one in Equation (45) existing in a melt. Information about silicate speciation in the molten state is more easily, and accurately, determined from the solid state ^{29}Si NMR spectra of glasses. The dynamics, however, are suitable to investigation by this novel high temperature NMR technique.

Narrow high temperature ^{29}Si lines indicate that silicate species move rapidly enough to average out the effects of the chemical shielding anisotropy (at least 3.5 kHz) in all but the most viscous melts near T_g. Narrow linewidths for ^{23}Na, however, indicate that the motion in melts is probably at least as fast as the quadrupole coupling constant (≈ 0.3 MHz). For both nuclei, the linewidth increases dramatically as temperature decreases (as the motion which averages $\mathcal{H}_{int}$ is 'frozen out'). In Na_2SiO_3, this broadening is probably the result of crystallization. The other samples, however, were recovered as homogeneous glasses, indicating that the samples were probably still in the liquid state during the experiments.

If structural rearrangements involving bond breaking and reformation occur in the melt (a change in the distribution of Q^n species), then the silicate species present in a melt undergo chemical exchange rapidly with respect to the typical separation in ^{29}Si Larmour fre-

quency between Q^n species (approximately 10-15 ppm or 350-500 Hz). At high temperatures, only a time averaged spectrum is observed in silicate liquids. As the temperature is lowered, the molecular motion and chemical exchange rate in molten $Na_2Si_4O_9$ slow, two resonance lines emerge. The development of shoulders on the ^{29}Si NMR melt spectra of several other silicate compositions suggest a similar slowing of reaction rates.

The dynamics of aluminosilicate melts have been probed by ^{29}Si and ^{23}Na relaxation time measurements. Sodium, presumed to diffuse through the melt as an ion, has activation energies for relaxation which are of the same order of magnitude as those of electic conductivity in similar composition melts. Silicon, involved with bond breaking and reformation motions, has relaxation time activation energies very close to the corresponding activation energies for viscous flow. Unfortunately, further analysis of the ^{23}Na relaxation data will be difficult since experimental viscosity data is sparse and the non-Arrhenius temperature dependence does not allow extrapolation of existing values. Also, few reliable measurements have been made on alkali diffusivity in melts at elevated temperatures.

CHAPTER VII:

SUMMARY

As demonstrated in this thesis, NMR spectroscopy has proven to be an invaluable technique for investigating the local structure of aluminosilicates. In addition to probing the dynamics present in silicate melts, NMR is a sensitive means of characterizing materials which lack long range order. Glasses and many crystalline minerals are observed by x-ray diffraction techniques to be disordered. However, ^{29}Si MAS NMR has been used to separate and quantify the different types of disorder possible in (crystalline) members of the nepheline mineral family.[131]

As observed by ^{29}Si NMR, silicate glasses are composed of well defined, symmetric local structures without long range ordering.[17,115] For homogeneous, single phase glasses of integral mean Q^n polymerization state, only one broad resonance is observed. The resonance corresponds to one average polymerization state (the Q^n compositional state). For the nonintegral mean Q^n composition glasses investigated, two discrete ^{29}Si NMR resonances corresponding to the two adjacent Q^n compositional species are present. However, a distribution of Q^n polymerization species are probably present with populations less than ~ 5%. In the noninteger mean Q^n composition glasses, the local environment of the Q^3 site is observed to have axial symmetry (three equivalent Si-O-Si bonds). Within experimental uncertainties, the glass Q^4 species is observed to have tetrahedrally symmetric Si-O-Si bonds.

In the liquid state, the silicate tetrahedra retain four Si-O bonds as well as the average (and most probable) number of Si-O-Si bonds found in the corresponding glass or crystalline form. The

isotropic ^{29}Si chemical shifts are the same, when comparison is possible, for a melt and the corresponding glass and/or crystalline material. This result indicates that the same silicate species are present in the liquid as well as in the glass state. Additionally, the predominant species in a melt is the one found in the corresponding glass and/or crystal. The dynamics of silicate liquids, however, are rapid enough at high temperatures to average the effects of speciation and local structure. As temperatures decrease to the glass transition, the motions slow and NMR becomes a more sensitive probe of the ^{29}Si and ^{23}Na electronic environments, separation of different silicate species is possible. The dynamics of aluminosilicate melts have been probed by ^{29}Si and ^{23}Na relaxation time measurements. Sodium, presumed to diffuse through the melt as an ion, has activation energies for relaxation which are of the same order of magnitude as those of electrical conductivity in melts of similar composition. Silicon, involved with bond breaking and reformation motions, has relaxation time activation energies very close to the corresponding activation energies for viscous flow.

APPENDIX A:

MAGIC ANGLE SPINNING (MAS)

The most common means of deriving isotropic chemical shift values in solid samples utilizes magic angle spinning (MAS) techniques. The ability to obtain isotropic chemical shifts from spectra of polycrystalline and noncrystalline samples allows identification and characterization of chemically and crystallographically distinct environments, as well as obtaining similar types of structural information which is routinely inferred from solution NMR measurements.

If the sample is rapidly spun at an angle β with respect to the static external magnetic field $\underline{H}_o$, the time averaged value of the angle between all internuclear vectors and the magnetic field is $<\theta_{ij}> = \beta$. When $\beta = 54°44'$, the 'magic' angle, then $<\cos^2\theta_{ij}> = 1/3$, hence $<\cos^2\theta_{ij} - 1> = 0$. This factor is important for the Hamiltonians which describe the magnetic dipole-dipole, chemical shielding, and nuclear quadrupole interactions present in solids. The mechanically induced time dependence of the anisotropic nuclear interactions of interest in solid state NMR will be examined.

A.1. MAS Averaged Homo- and Heteronuclear Dipolar Interactions

The time dependence imposed on the dipolar broadening Hamiltonian by rapid specimen rotation at an angle β to the static magnetic field $\underline{H}_o$ (conventionally choosen to be along the z axis) is[21]

$$< \mathcal{H}_{||} > = 1/2 \, (3<\cos^2\beta> - 1) \sum_{i<j} 1/2 \, \gamma_i \, \gamma_j \hbar^2 r_{ij}^{-3}$$
$$\cdot \, [\underline{I}_i \cdot \underline{I}_j - 3I_{zi}I_{zj}] \, (3\cos^2\beta_{ij} - 1) \, . \qquad (73)$$

Equation (73) is equivalent to $\mathcal{H}_{||}$, equation (21), multiplied by a scaling factor, $1/2(3\cos^2\beta - 1)$, dependent upon the angle of rota-

tion. For a polycrystalline or amorphous material, the spectrum retains an identical shape, but is reduced by the scaling factor. The spectrum of a dipolar broadened solid will narrow very sharply to a central line if the rotor frequency is much faster than the coupling.[21],[23]

A.2. MAS Averaged Chemical Shielding Anisotropy

Chemical shift anisotropy displays, under MAS conditions, the following property[21]

$$\langle \sigma_{zz} \rangle = \frac{3}{2} \sigma_{iso} \langle \sin^2 \beta \rangle + \frac{1}{2} (\langle 3\cos^2 \beta \rangle - 1)$$

$$\cdot \sum_{j=1}^{3} \sigma_{jj} \cos^2 \theta_{ij} \quad , \qquad (74)$$

where θ_j is the angle between the spinning axis and each of the three principal axes. Spinning at the magic angle causes $\langle \cos^2 \beta \rangle$ = 1/3 and $\langle \sin^2 \beta \rangle$ = 2/3, thus the time averaged value of σ_{zz} is reduced to the isotropic value σ_{iso}, and the CSA is removed.

For dipolar broadened spectra, the MAS rotation rate must be comparable to the linewidth in order for substantial line narrowing to be achieved. However, the central line is narrow for CSA, but its intensity is reduced by the presence of satellite peaks (spinning sidebands). The CSA interactions differ from dipolar broadening because under $\mathcal{H}_{CS}$ the spectrum is inhomogeneously broadened;[21] that is, each element of the static spectrum arises from crystallites in a particular orientation relative to the static external magnetic field. Hence, more information can be obtained from spinning at rates slower than the CSA because the principal axis components of

the anisotropies may be computed from the spinning sideband inten-
sities.[21,22] Also, removal of the anisotropic broadening inter-
actions by magic angle spinning can reveal magnetic fine structure
(e.g. isotropic scalar coupling which give rise to spin multiplets).

A.3. MAS Averaged Nuclear Quadrupole Interaction

Fast MAS should also average the quadrupolar Hamiltonian to a
small value. Because quadrupole interactions in noncubic environ-
ments are very large and second order broadening often occurs (Sec-
tion II.1.vi.), it is difficult to spin rapidly enough to average
Q completely away. However, by sampling the free induction decay
synchronously timed with the rotor period of the sample, it is pos-
sible to use magic angle specimen rotation at a few kHz to narrow a
^2H spectrum by three orders of magnitude.[24] Using this technique,
the first order quadrupole broadening is removed, allowing the small
isotropic ^2H chemical shifts and second order quadrupolar inter-
actions to be resolved.

A.4. MAS Spinning Sideband Analysis

For isotopically dilute spin 1/2 nuclei, the lineshapes of het-
eronuclear decoupled spectra are generally dominated by the chemical
shift anisotropy. The specimen rotation rate must exceed the breadth
of the shift anisotropy, otherwise partial averaging will occur and
result in satellite peaks (spinning sidebands or SSB) appear at
multiples of the rotor frequency.[21,23,25] Often, high resolution
spectra are obtained at the expense of losing the information con-

tained in the CSA. By reducing the spinning speed, the isotropic chemical shift and the spinning sideband intensities can together provide enough information to calculate the chemical shielding parameters.

Maricq and Waugh[25] developed a method based upon analysis of the second and third moments to compute the CSA tensor from MAS spectra. However, this technique requires accurate measurement of all the spinning sideband intensities, which is usually not possible. The intensities of individual sidebands are complicated functions of the chemical shift parameters, and are not readily manipulated to give analytic expressions for them. However, Herzfeld and Berger[22] evaluated the intensity functions numerically and constructed a graphical technique for extracting the chemical shielding parameters and estimating experimental error based on the intensities of just a few sidebands.

A.4.i. Chemical Shielding Anisotropy Tensor Determination

Using the conventional assignment of the principal values of the chemical shift tensor $\sigma_{11} > \sigma_{22} > \sigma_{33}$, a new set of variables are defined[22]

$$\mu = (\gamma H_o) (\sigma_{33} - \sigma_{11}) / \omega_r \qquad (75)$$

which is always positive, ω_r is the specimen rotation frequency, γH_o is the Larmour frequency at the isotropic chemical shift, σ_{iso}. And

$$\rho = (\sigma_{11} + \sigma_{33} - \sigma_{22}) / (\sigma_{33} - \sigma_{11}) \qquad (76)$$

has a value between -1 and +1. The extreme values of ρ correspond to axially symmetric tensors.

Contour plots of ρ versus μ for relative sideband intensities (up to $\pm$ 5 ω_r) were generated and published[22] using the central isotropic shift peak intensity as the reference. These plots are used to graphically obtain μ and ρ from an NMR spectrum. If the contours which correspond to the experimentally measured intensity ratio are drawn from the appropriate diagrams, then they will intersect at the corresponding values of μ and ρ. In general, due to experimental errors and difficulty interpolating between contour lines, the lines will not intersect at one point and the amount of dispersion is a measure of the uncertainity in μ and ρ. Note that contours for negative sidebands are as they appear for the contour maps while positive sidebands have contours which are flipped over.

A.4.ii. Alkali Silicate Glass CSA Computation

The ^{29}Si chemical shielding anisotropy tensor has been evaluated for several binary silicate glasses [natural abundance and 95% isotopically enriched $Na_2Si_4O_9$, $K_2Si_4O_9$, and $(Na_2O)_{0.4}(SiO_2)_{0.6}$] using the technique presented earlier in this Appendix. The spectra (Figures 23, 24, and 25) are first deconvoluted to separate the two central resonance lines and to obtain relative peak intensities for the spinning sidebands. The ratio of each sideband to the central Q^3 (or Q^2) peak are calculated and graphically analyzed by use of the contour maps. A sample contour plot of natural abundance $Na_2Si_4O_9$ glass is shown in Figure 47.
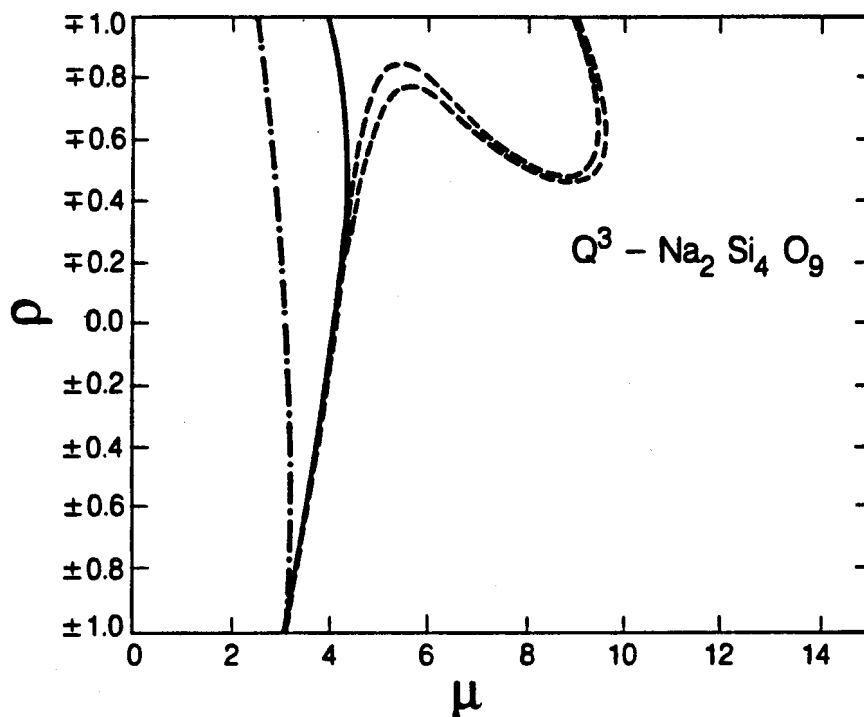
XBL 8511-11748

Figure 46: Contour plot for determination of the [29]Si chemical
shielding anisotropy tensor for the Q^3 silicate species
of glass $Na_2Si_4O_9$ (natural abundance) using the tech-
nique presented by Herzfeld and Berger.[22] When ρ is ± 1,
as in this diagram, then the CSA tensor is axially symmet-
ric. Three spinning sidebands were analyzed (+1, -1,
and -2). The +1 and -2 sidebands had very little error
associated with the deconvoluted fit, however the range
of possible values the -1 sideband can take on is outlined
with the double dashed line.

APPENDIX B:

COMPOSITE PULSES: SIMULATIONS AND EXPERIMENTS

A universal problem in pulsed NMR is that of exciting a nuclear spin system containing a broad spectrum of resonant frequencies using only a single frequency of rf radiation. Two types of excitation are of particular importance, namely the creation of coherence between spin states and the creation of a population inversion. Both of these can be accomplished with single rf pulses, the familiar 90° and 180° pulses, respectively. If the pulse power is such that the resulting Rabi frequency is ω_1, uniform excitation can only be achieved with single pulses over a spectral width $\Delta\omega$ satisfying the condition $\Delta\omega \ll \omega_1$. The precise limits on the inequality depend on the specific application, but the problem is severe enough that much effort has been devoted to improvements of the basic 90° and 180° pulses.

The square rf pulse required for pulse NMR techniques is generated by rapidly switching a rf oscillator. If the oscillator were allowed to run continuously, only the monchromatic frequency ω_0 would reach the sample. However, the finite pulse width generates a Fourier spectrum centered at the frequency ω_0, with a Lorentzian band of frequencies, $\Delta\omega = \omega_0 \pm 2\pi/t_p$, where t_p is the length of the pulse, reaching the sample.

B.1. Composite Pulses

The idea of replacing single rf pulses with sequences of pulses with phase shifts between them and with a constant amplitude for broadband excitation was first proposed by Levitt and Freeman. Such sequences were called "composite pulses." The development of these sequences has subsequently been an area of active research in

NMR[165-176] and coherent optics.[177] In the case of NMR, sequences of phase shifted rf pulses have been designed which excite nuclear spins over a larger range of some experimental parameter than the single 90° or 180° pulses that they replace.

B.2. Pulse Sequence Construction

The majority of composite pulses which have been derived emphasize the uniform excitation of spins over a range of chemical shifts in liquid samples.[165-168] In addition, composite pulses have been constructed for uniform excitation in the presence of inhomogeneity in the rf field strength[165-167,178] and spin coupling constants.[175, 176] A common feature of the chemical shift and the rf inhomogeneity problems is that they are both single spin problems. Single spins are easily described by the classical Bloch vector model.[2,6] This model allows geometric arguments and intuition to supplement exact numerical simulations of pulse sequences. Most of the progress in composite pulse sequence development for liquid state NMR has depended on this combination of geometric pictures and computer simulations.

Recently, new routes to the design of composite pulses have been explored. One of these is the generation of pulse sequences as approximations to continuously phase modulated pulses with broadband excitation properties.[7,179] This approach is well suited to constructing long sequences which excite spins over a very large spectral width. A second (relatively) new approach is the use of iterative schemes to produce successive improvements on a basic pulse

sequence unit.[172-174]   Again, this approach generates long sequences with very large excitation bandwidths.

The third approach to constructing composite pulses,[175] is the use of the Magnus expansion[176,177] in a manner similar to the coherent averaging theory that is central to many techniques in the NMR of solids, liquid crystals, and liquids.[1,7,180]   The Magnus expansion approach is, in principle, the most general method used.   It can be applied to both composite 180° and composite 90° pulses in a system of an arbitrary number of spins in which the spectral width results from any type of interaction.   Use of the Magnus expansion reduces the problem of finding a composite pulse to that of analytically or numerically solving a specific set of equations.   The generality obtained using the Magnus expansion is achieved at the expense of the physical, intuitive geometric pictures which characterized earlier approaches.   However, in a general, coupled many spin system, such as occurs in the NMR of anisotropic materials, the Bloch vector model does not apply (the system is not describable by only three coordinates).

The theory underlying average Hamiltonian approach to pulse sequence derivation may be found in detail in references 1, 7, 174, 175, 180, and 221.   Using the Magnus expansion, composite pulses are often most easily found by numerically solving the desired system of nonlinear equations.   Criteria are established for the precision to which the equations are to be solved, and a search for solutions is then conducted over a set of possible pulse length (t_p) and pulse phase (ϕ) combinations.   (A pulse, θ_ϕ, is described by the flip angle

$\theta = \omega_1 \cdot t_p \cdot 360^o$ and ϕ the pulse phase in the rotating frame; unless obvious, both are given in degrees.) Typically, more than one solution is found. In such cases, simulations of the performance of the composite pulses on model spin systems are used to select the best compostite pulse. Differences in the performance of composite pulses of the same calculated efficiency may be attributed to properties of higher terms in the Magnus expansion that are not set to zero. A composite π pulse derived in reference 190 ($45_0 180_{90} 90_{180} 180_{90} 45_0$, inverts a spectral width resulting from quadrupolar or dipole-dipole coupled spin systems) is used for demonstration in the next sections.

B.3. Simulations and Experiments

The composite pulses derived from the Magnus expansion approach often involve unusual rf phase shifts; that is, phase shifts other than the common multiples of 90°. For the experiments described in this appendix, the phase shifts were usually accomplished with a digitally controlled phase shifter based on a commercial Daico unit, capable of $360^o/256$ (1.4^o) phase increments. Alternatively, the rf phases can be set by inserting delay lines of the appropriate length into the quadrature generation circuit. Simulations indicate that the composite pulses can typically tolerate 5° to 10° deviations from the quoted phase shifts without a serious degradation of performance.[181] Thus, a phase shifter which produces rf phases in 15° increments would be sufficient. Similar phase shifting capabilities are necessary for other NMR techniques, notably multiple quantum spectroscopy.

B.3.1. Two Spin Systems

To make a comparison of the characteristics of several composite π pulses and a normal π pulse, computer simulations are shown (in Figure 47) of the inversion performance as a function of dipole-dipole coupling strength in a system composed of a pair of equivalent spin 1/2 nuclei. Inversion is defined as the final projection of spin angular momentum onto the $-z$ axis.

From Figure 47, it is apparent that both of the sequences, $45_0180_{90}90_{180}180_{90}45_0$ and $180_0180_{120}180_0$, provide substantial improvements in inversion performance over a single π pulse in a two spin dipole-dipole coupled system. Good inversion is accomplished using the composite pulses for couplings that are as large as $2\omega_1$. (Initially, the spin angular momentum is aligned with the z axis and has unit length.) These results apply identically to the inversion of a quadrupole spin 1 nucleus, substituting $2\omega_Q/\omega_1$ for d/ω_1 on the abscissa of Figure 47.

A pulse sequence used to experimentally contrast the inversion performance of composite π pulses against that of a single π pulse is illustrated in Figure 48. Spins initially at equilibrium are inverted by a π (Figure 48a) or composite π (Figure 48b) pulse. During a delay τ, coherences other than zero quantum dephase, leaving the spin system in a state describable by a density operator which commutes with I_z. The free induction decay is then collected following a $\pi/2$ pulse and Fourier transformed to give the spectrum. Spectral distortions at low rf power reflect imperfect inversion. The sequence of Figure 48a is commonly used to study spin lattice relaxation.

For number sequence only.
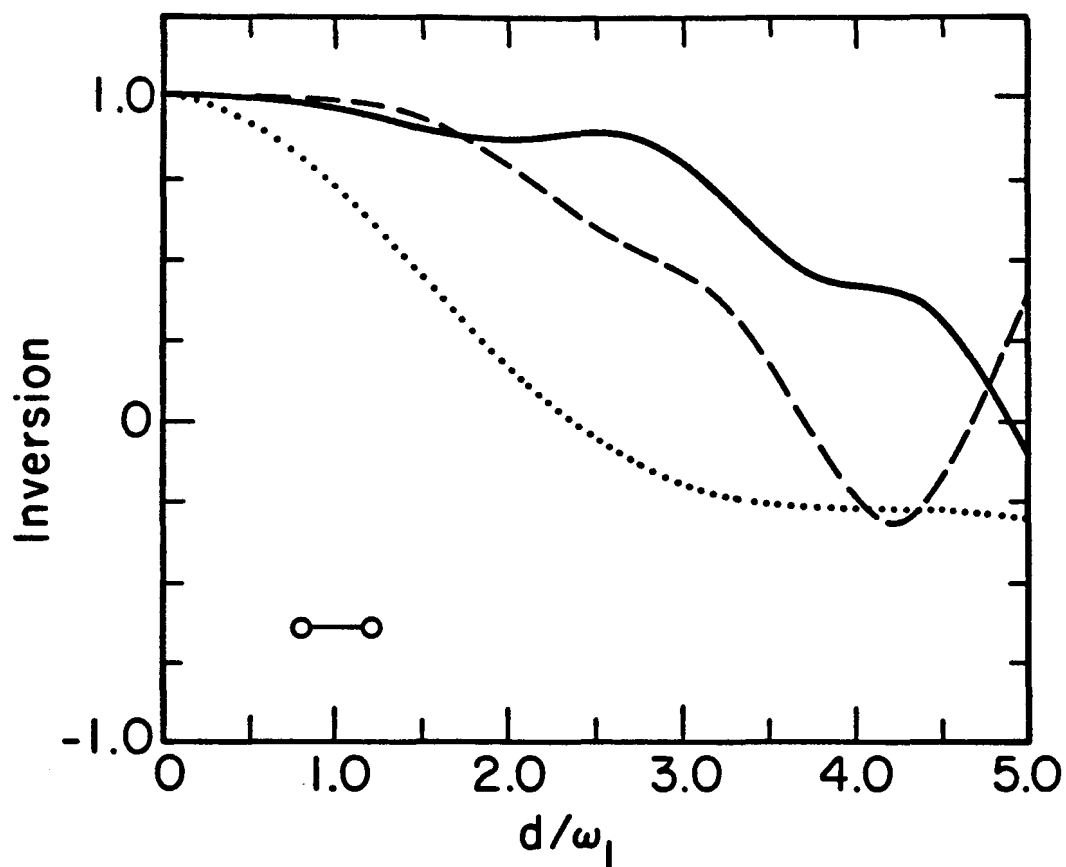
Figure 47: Simulation of inversion for a system of two dipole coupled spin 1/2 nuclei as a function of the ratio of the coupling constant d to the applied rf amplitude ω_1. Results are shown for a single π pulse (dotted line), a $45_0 180_{90} 90_{180} 180_{90} 45_0$ composite π pulse (solid line), and a $180_0 180_{120} 180_0$ composite π pulse (dashed line).

180_x

90_x

a)

τ

45_x 180_y $90_{\bar{x}}$ 180_y 45_x

90_x

b)

τ
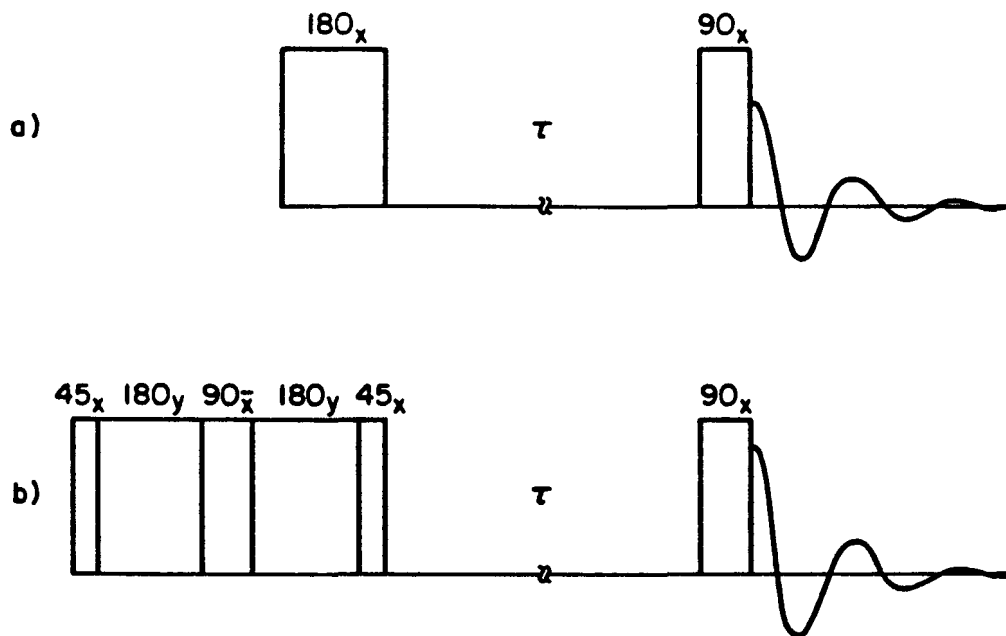
XBL 841-298

Figure 48: Schematic representation of the pulse sequences used in the simulations of Figure 47 and 49 and the experiments of Figures 50, 51 and 52. a) Spins are inverted by a π pulse. Single quantum and higher coherences, which are created at low rf amplitudes, dephase during a delay of length τ. The FID signal after the $\pi/2$ pulse is digitized and Fourier transformed to give a spectrum that reflects the inversion efficiency of the initial π pulse. b) Same as a), but with a $45_0 180_{90} 90_{180} 180_{90} 45_0$ composite π pulse in place of the single π pulse. A $180_0 180_{120} 180_0$ composite π pulse may be used as well.

Figure 48b represents the analogous experiment employing a composite π pulse. The fact that the two spin result apply identically to quadrupolar spin 1 nuclei makes the composite π pulses of obvious utility in deuterium and ^{14}N NMR.

B.3.I.A. Simulations of Powder Spectra

In Figure 49, simulations are shown of powder pattern[1,6] spectra resulting from the sequence of Figure 48a applied to an isotropic orientational distribution of spin 1/2 nuclei. The usual pattern results from the $3\cos^2\theta - 1$ dependence of the dipole-dipole coupling constant on the angle between the applied magnetic field and the internuclear displacement vector. Here, the maximum coupling is taken to be $d/2\pi = 80$ kHz. Clearly, the characteristic spectral features are lost as the rf amplitude is reduced.

Also in Figure 49, simulated spectra are shown which result from the sequence of Figure 48b. The composite π pulse has been substituted for the normal π pulse. The spectral distortion is dramatically reduced at low rf amplitudes. Using the other composite π pulse, $180_0 180_{120} 180_0$, gives essentially the same results.

The slight asymmetry in the spectrum of Figure 49f resulting from the composite π pulse is unusual, because it is generally assumed that the spectrum of a quadrupolar or dipole-dipole coupled spin system must be symmetric.[183] If a sequence of weak pulses ($\omega_1 < \omega_{coupling}$) is applied to a spin system described by an initial density operator I_z, then the presence of the couplings interferes with the applied rf pulse in such a way that the magnitude of the

Figure 49: Simulated NMR spectra of an isotropic orientational dis-
tribution of pairs of dipole coupled, spin 1/2 nuclei.
The maximum coupling is $d_{max}/2\pi$ = 80 kHz. 1 kHz line-
broadening is added. a) Spectrum after a single $\pi/2$
pulse, with $\omega_1/2\pi = \nu_1$ = 10 kHz. Since $\omega_1 \gg d_{max}$, the
spectrum is undistorted. b) Spectrum after a single $\pi/2$
pulse, with ν_1 = 32 kHz, illustrating the distortion
resulting from a $\pi/2$ pulse alone at low rf amplitudes.
c) Spectrum resulting from sequence a of Figure 49 with
ν_1 = 32 kHz. d) Spectrum resulting from sequence b of
Figure 49 with ν_1 = 32 kHz. e) Spectrum from sequence
b with ν_1 = 20 kHz. The characteristic features of the
spectrum, which are lost by a single π pulse at low rf
amplitudes, are preserved by a composite π pulse.

a
$\nu_I = 10$ MHz

b
$\nu_I = 32$ kHz

Single $\pi/2$ Pulse

c
$\nu_I = 32$ kHz

d
$\nu_I = 32$ kHz

e
$\nu_I = 20$ kHz

f
$\nu_I = 20$ kHz
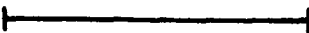
Single π Pulse
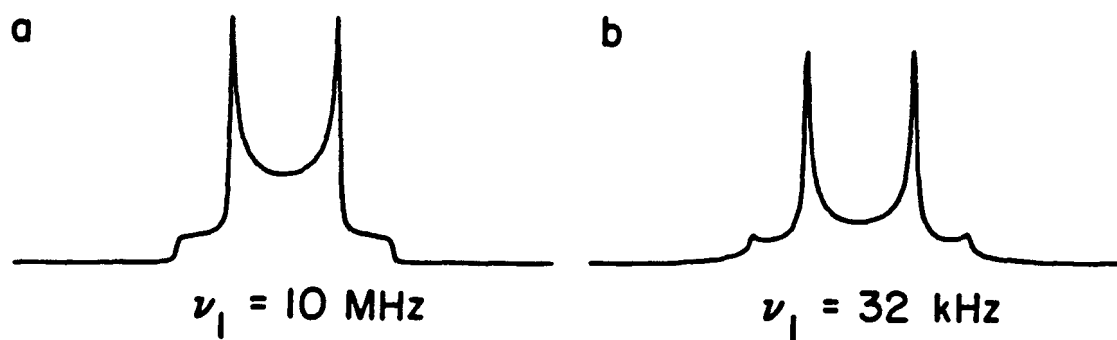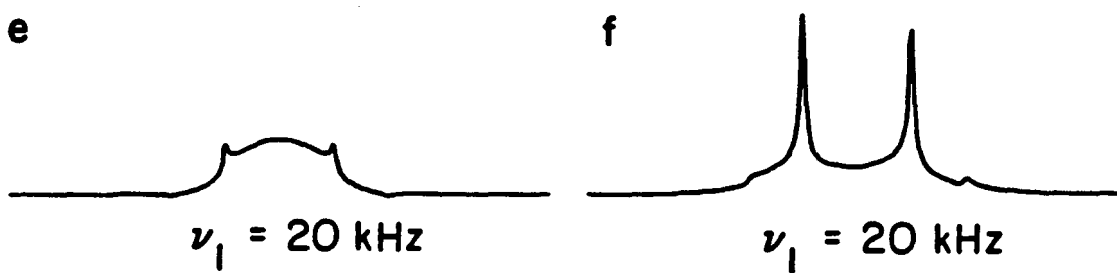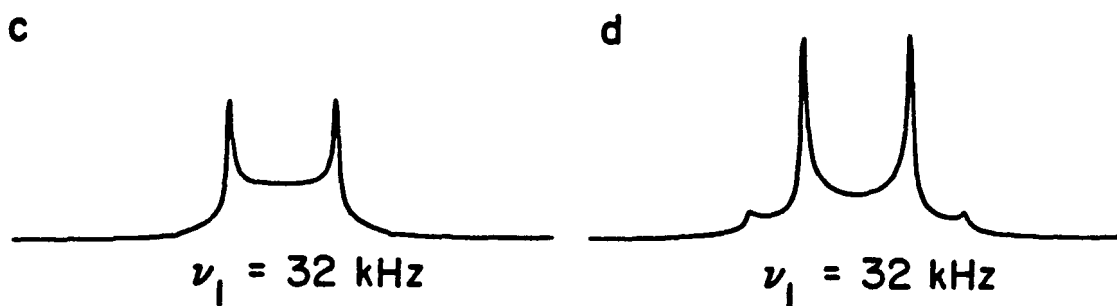
Composite π Pulse

100 kHz

expectation value of the spin angluar momentum actually changes. In other words, the magnetization shrinks. The density operator has evolved into not only linear combinations of I_x, I_y, and I_z, but also into multiple quantum coherence, zero quantum coherence, and nonobservable single quantum coherence. Therefore, the density operator for the spin system immediately before the final weak 90° pulse contains a component of dipolar order.[184] It is this dipolar order which produces the asymmetry in the spectrum in Figure 49f. The spectral asymmetry is absent in the spectra resulting from a single π pulse. This occurs because no dipolar order is created by a 180° pulse, regardless of rf amplitude.

B.3.1.B. Experimental Comparison

In Figure 50, the proton NMR spectra of $Ba(ClO_3)_2 \cdot H_2O$ powder is obtained with the squences of Figure 48 applied at two different rf amplitudes. The delay τ in Figure 48 is taken to be 5 ms. As predicted by the simulations, the spectral distortion with weak rf is quite obviously reduced by the use of a composite π pulse.

The spectrum of barium chlorate monohydrate reflects the fact that individual water molecules are essentially isolated from one another, giving a pattern characteristic of pairs of protons.[1,6] The experimental pattern is somewhat distorted from the ideal pattern assumed in the simulations by two factors. The first is the presence of couplings between water molecules. Such intermolecular couplings have the effect of broadening each individual transition, as reviewed in reference 146. The second factor is the presence of chemical

Figure 50: Experimental proton NMR spectra of $Ba(ClO_3)_2 \cdot H_2O$ powder. All spectra are the average of 60 scans, with a recycle delay of 30 seconds. a) Spectrum after a single $\pi/2$ pulse with ν_1 = 63 kHz. b) Spectrum after a single $\pi/2$ pulse with ν_1 = 33 kHz. c) Spectrum from sequence a of Figure 48 with ν_1 = 33 kHz. d) Spectrum from sequence b of Figure 48 with ν_1 = 33 kHz. e) Spectrum from sequence a with ν_1 = 20 kHz. f) Spectrum from sequence b with ν_1 = 20 kHz. The principal features of the simulations of Figure 49 are reproduced.

a

$\nu_I = 63$ kHz

b

$\nu_I = 33$ kHz

Single $\pi/2$ Pulse

c

$\nu_I = 33$ kHz

d

$\nu_I = 33$ kHz

e

$\nu_I = 20$ kHz

Single π Pulse

f

$\nu_I = 20$ kHz
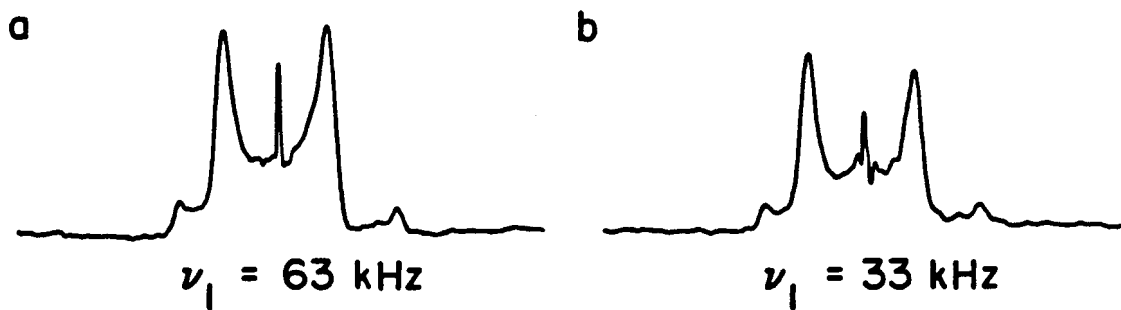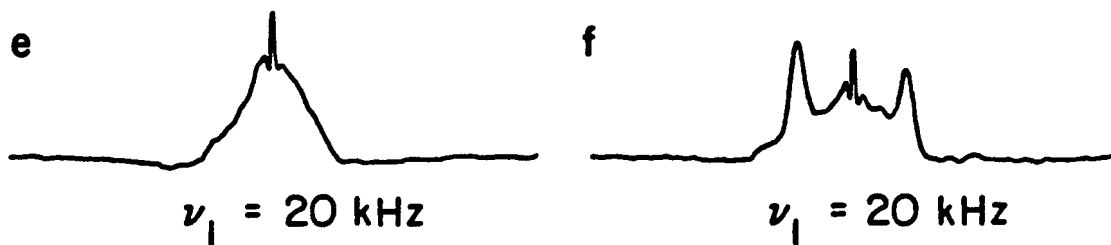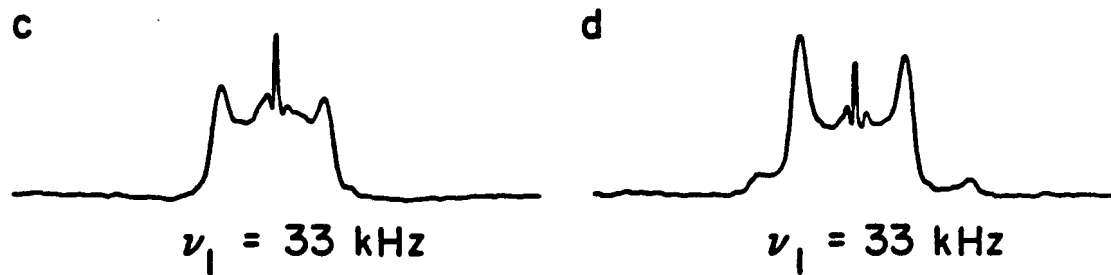
Composite π Pulse

|———————————|
100 kHz

shift anisotropy. The proton chemical shift anisotropy for H_2O in ice has been measured to be about 34 ppm.[185] The sharp peak in the center of the barium chlorate monohydrate spectra is attributed to residual protons and to water molecules that are free to reorient rapidly and isotropically. Similar experimental results to those in Figure 50 were obtained for the $180_0 180_{120} 180_0$ sequence.

B.2.11. Coupled, Multispin Systems

Coupled spins occur in configurations other than isolated pairs. For composite π pulses to be of general use in solid state NMR, they should provide an advantage over a single π pulse in an arbitrary system. Therefore, the inversion performance of composite π pulses is investigated in systems of more than two coupled spin 1/2 nuclei.

B.2.11.A. Simulations

In Figure 51, the results of computer simulations are presented of the inversion performance of the $45_0 180_{90} 90_{180} 180_{90} 45_0$ and $180_0 180_{120} 180_0$ composite π pulse sequences, as well as that of a single π pulse in three different spin systems. The spin system of Figure 51a consists of three spin 1/2 nuclei arranged in an equilateral triangle perpendicular to the applied constant magnetic field, so that all dipole coupling constants are equal. Figure 51b represents a system of four spin 1/2 nuclei in a square, again perpendicular to the applied field. The coupling constants are taken to be proportional to r_{ij}^{-3}, where r_{ij} is the distance between nucleus i and nucleus j. The spin system of Figure 51c is a row of six, equally

Figure 51: Simulations of inversion as a function of the ratio of
the nearest neighbor dipole coupling constant d to the
rf amplitude ω_1 for three possible systems of coupled
spin 1/2 nuclei. Results are shown for a single π pulse
(dotted lines), a $45_0 180_{90} 90_{180} 180_{90} 45_0$ composite π pulse
(solid lines), and a $180_0 180_{120} 180_0$ composite π pulse
(dashed lines). a) Three spins in an equilateral tri-
angle. b) Four spins in a square. c) Six spins in a
row. Coupling constants are taken to be proportional to
r_{ij}^{-3}, where r_{ij} is the distance between nuclei i and j.
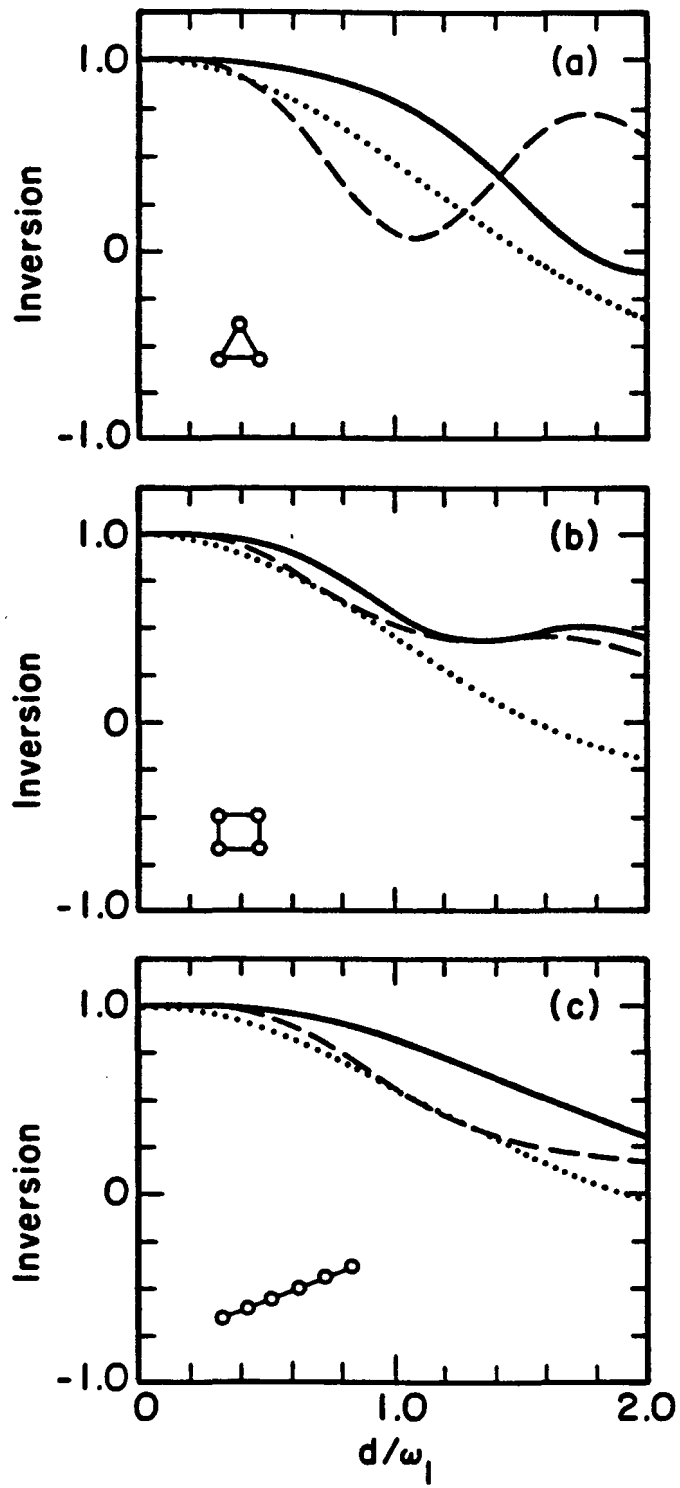
spaced spin 1/2 nuclei. Again, the coupling constants are proportional to r_{ij}^{-3}.

In all cases considered, both composite pulses gave better inversion than a single π pulse over some range of couplings. Generally, the $45_0 180_{90} 90_{180} 180_{90} 45_0$ sequence is the more effective of the two. The range of nearest neighbor couplings over which good inversion is achieved is substantially smaller than in the two spin case, for the single π as well as the composite π pulses.

B.2.11.B. Experimental Comparison

Experimental spectra resulting from the sequences of Figure 48 applied to a single crystal squaric acid ($C_4O_4H_2$) sample are shown in Figure 52. In the crystal, squaric acid molecules are arranged in planes in such a way that the hydrogen nuclei, or protons, form chains perpendicular to the molecular planes. The spacing between adjacent protons in a chain is known to be 2.635 Å .[187] Squaric acid has been the subject of NMR[189,190] and other studies,[186,188] in particular due to the observation of a structural phase transition at 370 K which exhibits critical behavior suggestive of a two dimensional system. Squaric acid was choosen for demonstration purposes because it is a true many spin solid, yet there is resolved structure in its proton NMR spectrum.

The spectra in Figure 52 are from a single crystal, although they superficially resemble a powder pattern. In a powder pattern, as in Figure 50, the features of the spectrum furthest from the center result from spins with the largest couplings. Therefore, those

Figure 52: Experimental proton NMR spectra of a squaric acid crystal.

All spectra are the averages of 20 scans, with a recycle

delay of 30 seconds. The narrow peak to the right of

center of each spectrum results from residual protons.

Its displacement from the center is due to the large

chemical shift of squaric acid, approximately 20 ppm

with respect to TMS at this orientation.   a)   Spectrum

after a single $\pi/2$ pulse with ν_1 = 63 kHz. b)   Spectrum

after a single $\pi/2$ pulse with ν_1 = 20 kHz. Low rf ampli-

tude results in a loss of intensity from the center of

the spectrum.   c)   Spectrum from sequence a of Figure 48

with ν_1 = 20 kHz.   d)   Spectrum from sequence a with ν_1 =

15 kHz.   e)   Spectrum from sequence b with ν_1 = 15 kHz.

Use of the composite π pulse results in greater overall

intensity, reflecting a more complete inversion.

a $\nu_I = 63$ kHz

b $\nu_I = 20$ kHz

Single $\pi/2$ Pulse

c $\nu_I = 20$ kHz

d $\nu_I = 20$ kHz

e $\nu_I = 15$ kHz

f $\nu_I = 15$ kHz
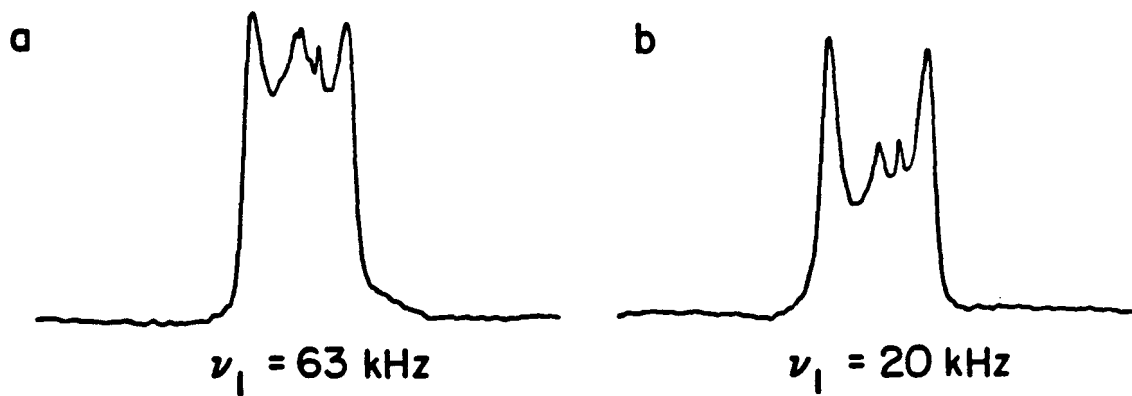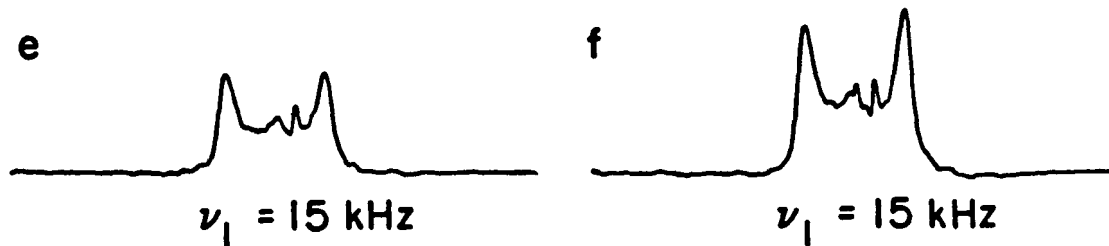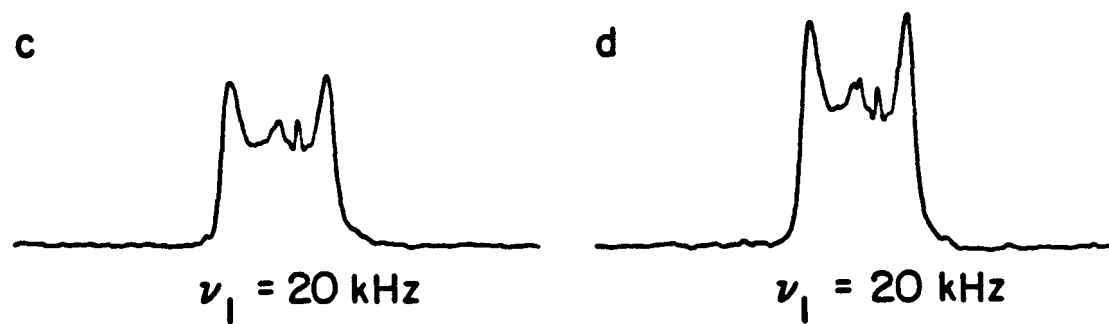
Single π Pulse   Composite π Pulse

100 kHz

features are lost first due to poor inversion at low rf amplitudes. The squaric acid spectrum, on the other hand, is the product of an essentially infinite network of coupled spins, with the strongest couplings occurring along chains. Each of the individual, unresolved transitions that make up the spectrum is a transition of the spin system as a whole. Because of this, it should not be expected that the outer spectral features would be attenuated at low rf amplitudes.

For the squaric acid experiments, the τ used was 5 ms. The crystal was doped with chromium to reduce the proton T_1 to approximately 10 s. The crystal was oriented with the b axis[186,188] parallel to the static magnetic field. In this orientation, the proton chains are parallel to the field, giving the strongest possible couplings.

B.4. Computational Approach

The computational approach used for simulations appearing in this appendix originated with a previous Pinenut, Jim Murdoch.[145]

Initially, the Hamiltonian which governs the interactions of interest is expressed as a second rank tensor (matrix) in a convenient basis set (usually the set of spin-product states). Direct calculation of the propagator U(t) is possible only under special circumstances. In general, first diagonalize the Hamiltonian

$$\mathcal{H}(t) = U(t) \, E(t) \, U^+(t) \, , \tag{77}$$

where E(t) is a diagonal matrix of eigenvalues, and U(t) is the unitary transformation matrix of column eigenvectors. The diagon-

alization of a Hermitian matrix can be performed numerically using standard algorithms.[145]

Having computed $U(t)$ and $E(t)$, the propagator may then be calculated by

$$\exp [-i \; \mathcal{H}(t) \; t \;] = U(t) \; \exp [-i \; E(t) \; t \;] \; U^{+}(t) \; . \tag{78}$$

Now, $\rho(t)$ is given by the expression

$$\rho(t) = U(t) \; \exp[-i \; E(t) \; t] \; U^{+}(t) \; \rho(t=0) \; U(t)$$

$$\exp[+i \; E(t) \; t] \; U^{+}(t) \; . \tag{79}$$

Mathematically, this expression is a series of matrix multiplications; physically, it describes the transformation of $\rho(t=0)$ to the basis set of $\mathcal{\hat{H}}(t)$, the evolution of $\rho(t)$ in that basis, and then the transformation back to the original eigenbasis.

Use of the fully time dependent Hamiltonian allows rigorous spectral simulation as well as computation of pulse sequence effects on various spectral artifacts caused by spectrometer imperfections (e.g. finite pulse width, phase errors, flip angle errors, and phase distortions).

B.4.1. Homonuclear Spin 1/2 System

Main Program:

```
      program dinkpulse
c
c     simulates a generic weak pulse sequence on a 6 or less
c     spin system previously described in MOLEC.FOR.
c     Variable pulse intensity is available.
c     The final density matrix and a fid is computed.
c     FFT2PLOT.FOR is able to perform a fourier transform on the
c     'data', and plot the spectrum.
c
      dimension h(210),s(400),x(2080)
      dimension numb(2,64),d(28),cj(28),ist(20),isp(8),lst(2,64),
     1  cs(8),iflip(2),e(64),xi(64,64),zi(64,64)
      dimension ss(922),istart(7),nbc(9)
      dimension flip(30),phase(30),ntype(30),tau(30)
      dimension u(4096),hh(2080),ham(2080),ee(64),vv(1001)
      complex yi(64,64),zv(256),rho(64,64),phi(64,64),pham(64,64),phh(64,64)
      complex yyy,zzz,uu(64,64)
      common/dat1/n,nop,voff,d,cj,cs,nfid,dt
      common/dat2/nv,v0,vinc,npul,ntype,flip,phase,tau
      common/ss/ss,s,nbc
      data hh/2080*0.0/
c
      mat(i,j)=j * (j-1) / 2   +   i
      indx(i,j)= (j-1) * nst  +  i
c
      call info
c
      nm1=n-1
      np1=n+1
      nst=2**n
      nnst=nst * nst
      nstm1=nst-1
      twopi=8.0 * atan(1.0)
      cst=1.0e-6 * twopi
c
c     first, set up the dipolar hamiltonian (block diagonal when in
c     Iz basis set).  Block according to m value, then diagonalize .....
c        Hd = sum over i, sum over j, D(i,j) [I(z,i)*I(z,j)
c                  - 0.5 * (I(x,i)*I(x,j) + I(y,i)*I(y,j)) ]
c
      nbc(1)=1
      nbc(np1)=1
c
c     first look at the extreme cases, all spins up or all down
c
      acs=0.0
      do 20 i=1,n
20    acs=acs + cs(i)
      ecp=0.0
      do 25 i=1,nop
25    ecp=ecp + d(i) + cj(i)
      e(1)=-n*voff + ecp - acs
      e(nst)=n*voff + ecp + acs
      hh(1)=e(1)
      lp=mat(nst,nst)
      hh(lp)=e(nst)
      nst0=1
      mnst0=0
      call numsort(numb,n,nst)
      lst(1,1)=numb(1,nst)
      lst(2,1)=numb(2,nst)
      lst(1,nst)=numb(1,1)
      lst(2,nst)=numb(2,1)
```

```
                     kkk=1
c
c            now examine individual blocks (greater than 1x1 matrices)
c            only the upper triangular matrix elements need be computed
c
             do 110 js=1,nm1
             istart(js)=mmst0
             is=n - js
             itsp=2*is - n
             kk=0
             do 40 j=1,nst
             if(numb(2,j) .ne. is) go to 40
             kk=kk+1
             kkk=kkk+1
             ist(kk)=numb(1,j)
             lst(1,kkk)=numb(1,j)
             lst(2,kkk)=is
40           continue
             mst=kk
             nbc(js+1)=kk
             lm=0
             do 80 m=1,mst
             do 80 l=1,m
             lm=lm+1
             ij=mat(mst0+l,mst0+m)
c
c            fill in the diagonal elements
c
             if(l .ne. m) go to 60
             msk=1
             do 50 k=1,n
             isp(k)=-1
             if((ist(l) .and. msk) .ne. 0) isp(k)=1
             msk=msk + msk
50           continue
             h(lm)= -voff*itsp
             kk=0
             do 55 i=1,nm1
             ip1=i+1
             do 55 j=ip1,n
             kk=kk+1
             h(lm)=h(lm)   +   (d(kk) + cj(kk)) * isp(j) * isp(i)
55           continue
             do 45 i=1,n
45           h(lm)=h(lm)  - cs(i)*isp(i)
             go to 85
c
c            and now, the off-diagonal elements
c
60           jw=1
             jsp=0
             h(lm)=0.0
             msk=1
             do 75 k=1,n
             if((ist(l) .and. msk) - (ist(m) .and. msk)) 70,75,70
70           jsp=jsp+1
             iflip(jw)=k
             jw=2
75           msk=msk * 2
             if(jsp .ne. 2) go to 80
             k5= (2*n - iflip(1))*(iflip(1) - 1)/2  -  iflip(1)  +  iflip(2)
             h(lm)= -d(k5) + 2.0*cj(k5)
85           hh(ij)=h(lm)
```

```
80        continue
c
c         diagonalize the individual blocks of the internal hamiltonian
c
          call reigen(h,s,mst)
c
c         piece together the complete transformation matrix for Hint
c
          do 90 i=1,mst
90        e(mst0+i)=h(i)
          do 100 m=1,mst
          do 100 l=1,mst
          lm=l + (m-1)*mst
          ss(mmst0+lm)=s(lm)
100       continue
          mst0=mst0 + mst
          mmst0=mmst0 + mst*mst
110       continue
c
          open(unit=01,name='fid.dat',type='new',err=800)
c
c         loop over pulse strength values ......
c
          write(1,600) nfid
          ndt1 = dt/1
          write(1,600) ndt1
          write(1,600) nv
600       format(i14)
          do 400 iv=1,nv
          vv(iv) = d(1)/(v0  +  (iv-1) * vinc)
          vv2=-vv(iv) / 2.0
          csr = d(1)/vv(iv)
          write(1,610) iv,vv(iv),csr
610       format (//,4x,'vv(',i4,' ) = ',e12.6,/,10x,
     1      ' coupling strength =',f12.6)
c
c         generation of the full hamiltonian:  H(internal) + H(rf) .....
c         (upper triangle of matrix only)
c
          do 230 j=1,nst
          do 230 i=1,j
          ij=mat(i,j)
          ham(ij)=hh(ij)
          x(ij)=0.0
c
c         if 1 spin is flipped an I(x) element is present
c
          if(iabs(lst(2,i) - lst(2,j)) .ne. 1) go to 230
          ksp=0
          msk=1
          do 220 k=1,n
          if((lst(1,i) .and. msk) .eq. (lst(1,j) .and. msk)) go to 220
          ksp=ksp + 1
220       msk=msk + msk
c
c         if I(x) is present, the matrix element is the pulse strength
c
          if(ksp.ne.1) go to 230
          ham(ij)=vv2
          x(ij)=0.5
230       continue
c
c         diagonalize the full hamiltonian and get eigenvectors and energies
```

```
c
            call reigen(ham,u,nst)
c
c           fill in complete transformation matrix UU(nst,nst)
c
            do 210 i=1,nst
            do 210 j=1,nst
            ij = indx(i,j)
            uu(i,j) = cmplx(u(ij),0.0)
210         continue
c
            do 235 i=1,nst
235         ee(i)=ham(i)
c
c           set up Iz in the spin-product basis .....
c           (off-diagonal elements are 0.0)
c
            do 240 i=1,nst
            do 240 j=1,nst
            rho(i,j)=cmplx(0.0,0.0)
            zi(i,j)=0.0
            if(i .ne. j) go to 240
            zi(i,j)=lst(2,i) - n/2.0
240         rho(i,j) = cmplx(zi(i,j),0.0)
c
c           calculate I(x) and I(y) in the spin product basis set
c
            do 170 j=1,nst
            do 170 i=1,j
            ij = mat(i,j)
            xi(i,j) = x(ij)
            xi(j,i) = x(ij)
            yi(i,j) = xi(i,j)*cmplx(0.0, -1.0)
            yi(j,i) = xi(j,i)*cmplx(0.0, 1.0)
170         continue
c
c           calculate the evolution matrix for each step
c
            do 120 ipul=1,npul
            if (ntype(ipul).eq.0) go to 130
            tau(ipul)=(flip(ipul)*1000000)/(vv(iv)*360.0)
c
c           examine the pulses first
c           NOTE: pulses may be represented by
c           exp -i*(v*I(phi) + Hint)*tau = exp -i*I(z)*phi
c                 exp -i*(v*I(x) + Hint)*tau   exp i*I(z)*phi
c
c           so, the propagator is
c           exp -i*H(phi)*t = exp -i*phi*I(z)   exp -i*H(x)*t   exp i*phi*I(z)
c                 = exp -i*phi*I(z)   U   exp -i*H(x)*t   Uadj   exp i*phi*I(z)
c
c           first the set-up the x-pulse matrix
c
            do 140 i=1,nst
            do 140 j=1,nst
            pham(i,j)=cmplx(0.0,0.0)
            phi(i,j)=cmplx(0.0,0.0)
            if (i.ne.j) go to 140
            pham(i,j) = cexp (cmplx (0.0, ee(i)*tau(ipul)*cst))
            rot = zi(i,j)*phase(ipul)*twopi/360.0
            phi(i,j) = cexp (cmplx (0.0, rot))
140         continue
c
```

```
c          find the x-pulse propagator
c
           call umua (uu,pham,nst,zv)
c
c          then rotate about the z-axis
c
           call uamu (phi,pham,nst,zv)
           go to 160
c
c          now examine the delays
c
130        do 150 i=1,nst
           do 150 j=1,nst
           pham(i,j) = cmplx(0.0,0.0)
           if (i.ne.j) go to 150
           pham(i,j) = cexp (cmplx (0.0, e(i)*tau(ipul)*cst))
150        continue
c
c          the propagator for the internal hamiltonian is
c          exp -i*H*t  =  SS  exp -i*E*t   SSadj
c
c
c          multiply, blockwise, SS * PHAM * SSadj
c
           call blkmua (pham,nst,zv,n)
           call blkmau (pham,nst,zv,n)
c
c          evolve the density matrix
c
160        call uamu (pham,rho,nst,zv)
120        continue
c
c          calculate the internal hamiltonian's propagator for an
c          evolution time of dt
c
           do 200 i=1,nst
           do 200 j=1,nst
           phh(i,j) = cmplx(0.0,0.0)
           if (i.ne.j) go to 200
           phh(i,j) = cexp (cmplx (0.0, e(i)*dt*cst))
200        continue
c
c          multiply, blockwise, SS * PHH * SSadj
c
           call blkmua (phh,nst,zv,n)
           call blkmau (phh,nst,zv,n)
c
c          calculate normalization factors
c
           xx = 0.0
           yy = 0.0
           zz = 0.0
           do 260 i=1,nst
           do 260 j=1,nst
           xx = xx + xi(i,j)*xi(j,i)
           yy = yy + yi(i,j)*yi(j,i)
           zz = zz + zi(i,j)*zi(j,i)
260        continue
           write(1,270) zz
270        format(/, 2x,'normalization constant = <I(z)**2>',
     1              2x,f8.4)
c
c          generate an FID by computing observables as a function of time
```

```
              do 180 k=1,nfid
c
c          to calculate <X>, <Y>, and <Z>
c              <A> = Tr (A*rho) = sum over i (A*rho)(ii)
c                  = sum over i [ sum over j (A(ij)*rho(ji)) ]
c
              avex = 0.0
              avey = 0.0
              avez = 0.0
              do 190 i = 1,nst
              do 190 j = 1,nst
              avex = avex + xi(i,j)*rho(j,i)
              avey = avey + yi(i,j)*rho(j,i)
              avez = avez + zi(i,j)*rho(j,i)
190           continue
              avez = avez/zz
              zzz = cmplx(avex/zz, avey/zz)
              write(1,640) k,zzz,avez
640           format(1x,i4,3f16.8)
              if (k.eq.nfid) go to 180
c
c          allow the density matrix to evolve under Hint
c
              call uamu (phh,rho,nst,zv)
180           continue
c
400           continue
c
              close(unit=01,err=900)
              go to 950
800           type 810
810           format(/,' open error!!',/)
              go to 950
900           type 910
910           format(/,' close error!!',/)
950           continue
              end
c
c
c
c


              subroutine info
c
c          reads and print molecular information and pulse sequence stored
c          in molec.da
c
              dimension d(28),cj(28),cs(8)
              dimension flip(30),phase(30),tau(30),ntype(30)
              common/dat1/n,nop,voff,d,cj,cs,nfid,dt
              common/dat2/nv,v0,vinc,npul,ntype,flip,phase,tau
c
              open(unit=01,name='molec.dat',type='old',err=800)
              read(1,600) n
              read(1,600) nop
600           format(i14)
              read(1,610) voff
              do 605 i=1,nop
              read(1,610) d(i)
              read(1,610) cj(i)
605           continue
              do 615 i=1,n
```

```
        read(1,610) cs(i)
615     continue
610     format(e12.6)
        read(1,600) nv
        read(1,610) v0
        read(1,610) vf
        read(1,610) vinc
        read(1,600) npul
        do 625 i=1,npul
        read(1,600) ntype(i)
        read(1,610) flip(i)
        read(1,610) phase(i)
        read(1,610) tau(i)
625     continue
        read(1,600) nfid
        read(1,610) dt
        close(unit=01,err=900)
c
        nm1=n-1
        np1=n+1
        print 500,voff
500     format(6x,'offset freq. = ',f7.1,' Hz',//)
        voff=voff/2.0
        print 505
505     format(6x,'dipolar and J couplings (in Hz)',/,6x,31(1h-),/)
        k=0
        do 10 i=1,nm1
        ip1=i+1
        do 10 j=ip1,n
        k=k+1
        if (v0.gt.0.0) go to 20
        d(k) = -d(k)
        cj(k) = -cj(k)
20      print 510,i,j,d(k),i,j,cj(k)
510     format(6x,'D(',i1,',',i1,') =',f9.2,5x,'J(',i1,',',i1,') =',
     1   f6.2)
c
c       to enable comparison with Rob's couplings
c
        d(k)=d(k)/4.0
        cj(k)=cj(k)/4.0
10      continue
        print 515
515     format(//,6x,'chemical shifts in Hz',/,6x,21(1h-),/)
        print 520,(cs(i), i=1,n)
520     format(6x,8f10.2)
        do 15 i=1,n
15      cs(i)=cs(i)/2.0
c
        print 525, nv
525     format(//,1x,i6,' values of coupling constant considered',/)
        print 530, v0
530     format(8x,'initial value = ',f10.3)
        print 560, vf
560     format(8x,'final value   = ',f10.3)
        print 535, vinc
535     format(8x,'increment     = ',f10.3)
c
        print 540,npul
540     format(5x,'number of steps in the pulse sequence =',i4)
        print 545
545     format(//,2x,'step',2x,'type',2x,'flip angle (deg)',
     1      2x,'pulse phase (deg)',2x,'delay (usec)',//)
```

```
        do 30 i=1,npul
        print 550,i,ntype(i),flip(i),phase(i),tau(i)
550     format(2(3x,i4),3(3x,f8.2))
30      continue
c
        type 555,nfid,dt
555     format(/,' number of points in the fid =',i4,
     1       '.  Sampling rate is',f10.4,'usec.',/)
c
        go to 950
800     type 810
810     format(/,' open error!!',/)
        go to 950
900     type 910
910     format(/,' close error!!',/)
950     continue
        return
        end
c
c
c
c
c
        subroutine blkmua (a,nst,r,n)
c
c       blockwise multiplication of A = X * A
c
        complex a(64,64),r(256),zz
        dimension ss(922),x(20,20),nbc(7),s(400)
        common/ss/ss,s,nbc
c
        np1 = n+1
        kk = 0
        ns = 0
c
        do 100 ib=1,np1
        nb=nbc(ib)
        if (nb.eq.1) x(1,1)=1.0
        if (nb.gt.1) call stuff (nb,kk,ss,x)
c
        do 40 j=1,nst
        do 20 i=1,nb
        zz=0.0
        do 10 k=1,nb
10      zz = zz + x(i,k)*a(ns+k,j)
20      r(i) = zz
        do 30 i=1,nb
30      a(ns+i,j) = r(i)
40      continue
c
        ns = ns + nb
100     continue
        return
        end
c
c
c
c
c
        subroutine blkmau (a,nst,r,n)
c
c       another blockwise matrix multiplier A = A * Xadj
```

```
      complex a(64,64),r(256),zz
      dimension ss(922),x(20,20),nbc(7),s(400)
      common/ss/ss,s,nbc
c
      np1 = n+1
      kk = 0
      ns = 0
c
      do 100 ib=1,np1
      nb=nbc(ib)
      if (nb.eq.1) x(1,1)=1.0
      if (nb.gt.1) call stuff (nb,kk,ss,x)
c
      do 40 i=1,nst
      do 20 j=1,nb
      zz=0.0
      do 10 k=1,nb
10    zz = zz + a(i,ns+k)*x(j,k)
20    r(j) = zz
      do 30 j=1,nb
30    a(i,ns+j) = r(j)
40    continue
c
      ns = ns + nb
100   continue
      return
      end
c
c
c
c
c
      subroutine stuff (nb,kk,uu,u)
c
      dimension uu(922), u(20,20)
c
      do 20 j=1,nb
      do 10 i=1,nb
      kk=kk+1
10    u(i,j) = uu(kk)
20    continue
      return
      end
```

Initial, supplementary program:

```
        program molec
c
c       asks questions about the system to be studied
c
        dimension d(40),cj(40),cs(8)
        dimension flip(30),phase(30),ntype(30),tau(30)
        type 500
500     format(/,' enter the number of spins: ',$)
        accept *,n
        nm1=n-1
        ncp=n*nm1/2
        type 510
510     format(/,' enter the offset freq. in Hz (not kHz) : ',$)
        accept *,voff
        type 520
520     format(/,' enter dipole and j couplings in Hz....',/)
        k=1
        do 10 i=1,nm1
        ip1=i+1
        do 10 j=ip1,n
        type 530,i,j,i,j
530     format(' d(',i1,',',i1,') and j(',i1,',',i1,') : ',$)
        accept *,d(k),cj(k)
        k=k+1
10      continue
        type 540
540     format(/,' enter chemical shifts in Hz....',/)
        do 20 i=1,n
        type 550,i
550     format(5x,'cs(',i1,') : ',$)
        accept *,cs(i)
20      continue
c
        type 570
570     format(/,' initial and final values of coupling ratio',
     1         ' to be considered??', $)
        accept *, v0, vf
        if (v0.eq.vf) go to 50
        type 580
580     format(/,' increment ',$)
        accept*, vinc
        nv = (vf - v0)/vinc + 1
        go to 60
50      nv = 1
        vinc = 0.0

c
60      type 650
650     format(/,' how many steps in pulse sequence?',$)
        accept*,npul
        do 30 i=1,npul
        flip(i)=0.0
        phase(i)=0.0
        tau(i)=0.0
        type 660,i
660     format(/,' is step',i3,' a pulse (=1) or a delay (=0)?',$)
        accept*,ntype(i)
        if (ntype(i).eq.1) go to 40
        type 670
670     format(/,' enter delay time in usec',$)
        accept*,tau(i)
        go to 30
40      type 680
```

```
680        format(/,' enter pulse flip angle and phase (in deg)',$)
           accept*,flip(i),phase(i)
30         continue
c
           type 690
690        format(/,' how many points in the fid?',$)
           accept*,nfid
           type 700
700        format(/,' how often should sampling occur (usec)?',$)
           accept*,dt
c
           open(unit=01,name='molec.dat',type='new',err=800)
           write(1,600) n
           write(1,600) ncp
600        format(i14)
           write(1,610) voff
           do 605 i = 1, ncp
           write(1,610) d(i)
           write(1,610) cj(i)
605        continue
           do 615 i=1,n
           write(1,610) cs(i)
615        continue
610        format(e12.6)
           write(1,600) nv
           write(1,610) v0
           write(1,610) vf
           write(1,610) vinc
           write(1,600) npul
           do 625 i=1,npul
           write(1,600) ntype(i)
           write(1,610) flip(i)
           write(1,610) phase(i)
           write(1,610) tau(i)
625        continue
           write(1,600) nfid
           write(1,610) dt
           close(unit=01,err=900)
           stop
800        type 590
590        format(/,' open error!!',/)
           stop
900        type 595
595        format(/,' close error!!',/)
           stop
           end
```

B.4.ll. Heteronuclear Multispin System (I=1/2, S=1/2)

Main program (requires the same initial, supplementary program
as in section A.4.l.):

```
        program hetdp
c
c       a variation of DINKPULSE which simulates a heteronuclear
c       system with one S-spin and n-protons (I, S = 1/2).
c
c       initial density matrix = S(x) + I(z)
c       only I spins are manipulated.
c
c
c       simulates a generic weak pulse sequence on a 6 or less
c       spin system previously described in HETDPQUE.FOR.
c       Variable pulse intensity is available.
c       The final density matrix and a fid is computed.
c       FFT2PLOT.FOR is able to perform a fourier transform on the
c       'data', and plot the spectrum.
c
        dimension h(210),s(400),xd(64,64),zd(64,64)
        dimension numb(2,64),d(50),cj(50),ist(20),isp(8)
        dimension lst(2,64),cs(8),iflip(2),e(64),xx(64,64),zz(64,64)
        dimension ss(922),istart(7),nbc(9)
        dimension flip(50),phase(50),ntype(50),tau(50)
        dimension u(4096),hh(2080),ham(2080),ee(64),vv(1001)
        complex zv(256),rho(64,64),phi(64,64),pham(64,64),phh(64,64)
        complex zzz,uu(64,64),yy(64,64),yd(64,64)
        common/dat1/n,nop,voff,d,cj,cs,nfid,grat,ncy,ncsteps
        common/dat2/nv,v0,vinc,npul,ntype,flip,phase,tau
        common/ss/ss,s,nbc
        data hh/2080*0.0/
c
        mat(i,j)=j * (j-1) / 2   +   i
        indx(i,j)= (j-1) * nst  +  i
c
        call info
c
        nm1=n-1
        np1=n+1
        nst=2**n
        nnst=nst * nst
        nstm1=nst-1
        twopi=8.0 * atan(1.0)
        cst=1.0e-6 * twopi
c
c       set up the dipolar hamiltonian (block diagonal when in
c       Iz basis set).  Block according to m value, then diagonalize .....
c          Hd = sum over i, sum over j, D(i,j) [I(z,i)*I(z,j)
c                   - 0.5 * (I(x,i)*I(x,j) + I(y,i)*I(y,j)) ]
c
        nbc(1)=1
        nbc(np1)=1
c
c       first look at the extreme cases, all spins up or all down
c
        acs=0.0
        do 20 i=1,n
20      acs=acs + cs(i)
        ecp=0.0
        do 25 i=1,nop
25      ecp=ecp + d(i) + cj(i)
        e(1)=-nm1*voff + ecp - acs
        e(nst)=nm1*voff + ecp + acs
        hh(1) = e(1)
        lm = mat(nst,nst)
        hh(lm) = e(nst)
```

```
         mst0=1
         mmst0=0
         call numsort(numb,n,nst)
         lst(1,1)=numb(1,nst)
         lst(2,1)=numb(2,nst)
         lst(1,nst)=numb(1,1)
         lst(2,nst)=numb(2,1)
         kkk=1
c
c        now examine individual blocks (greater than 1x1 matrices)
c        only the upper triangular matrix elements need be computed
c
         do 110 js=1,nm1
         istart(js)=mmst0
         is=n - js
         itsp=2*is - n
         kk=0
         do 40 j=1,nst
         if(numb(2,j) .ne. is) go to 40
         kk=kk+1
         kkk=kkk+1
         ist(kk)=numb(1,j)
         lst(1,kkk)=numb(1,j)
         lst(2,kkk)=is
40       continue
         mst=kk
         nbc(js+1)=kk
         lm=0
         do 80 m=1,mst
         do 80 l=1,m
         lm=lm+1
         ij = mat(mst0+l,mst0+m)
c
c        fill in the diagonal elements
c
         if(l .ne. m) go to 60
         msk=1
         do 50 k=1,n
         isp(k)=-1
         if((ist(l) .and. msk) .ne. 0) isp(k)=1
         msk=msk + msk
50       continue
c
c        count total proton spin
c
         ips = is
         if (isp(1).eq.1) ips = is - 1
         itsp = 2*ips - nm1
         h(lm)= -voff*itsp
         kk=0
         do 55 i=1,nm1
         ip1=i+1
         do 55 j=ip1,n
         kk=kk+1
         h(lm)=h(lm)   +   (d(kk) + cj(kk)) * isp(j) * isp(i)
55       continue
         h(lm) = h(lm) - cs(1)*grat*isp(1)
         do 45 i=2,n
45       h(lm)=h(lm) - cs(i)*isp(i)
         hh(ij) = h(lm)
         go to 80
c
c        and now, the off-diagonal elements
```

```
60          jw=1
            jsp=0
            h(lm)=0.0
            msk=1
            do 75 k=1,n
            if((ist(l) .and. msk) - (ist(m) .and. msk)) 70,75,70
70          jsp=jsp+1
            iflip(jw)=k
            jw=2
75          msk=msk * 2
            if(jsp .ne. 2) go to 80
            k5= (2*n - iflip(1))*(iflip(1) - 1)/2  -  iflip(1)  +  iflip(2)
c
c           eliminate heteronuclear flip-flop terms
c
            if (k5.gt.nm1) h(lm) = -d(k5) + 2.0*cj(k5)
            hh(ij) = h(lm)
80          continue
c
c           diagonalize the individual blocks of the internal hamiltonian
c
            call reigen(h,s,mst)
c
c           piece together the complete transformation matrix for Hint
c
            do 90 i=1,mst
            e(mst0+i)=h(i)
90          continue
            do 100 m=1,mst
            bigs = 0.0
            do 95 l=1,mst
            lm=l + (m-1)*mst
            ss(mmst0+lm)=s(lm)
            if (abs(s(lm)) .le. bigs) go to 95
            bigs = abs(s(lm))
            ll = l
95          continue
100         continue
            mst0=mst0 + mst
            mmst0=mmst0 + mst*mst
110         continue
c
c           generate Ix(xx),Iz(zz),Sx(xd),Sy(yd),and Sz(zd)
c           in the spin-product basis set.
c
c           the initial density matrix is also computed
c                   rho(0) = Sx + Iz
c
c           Iz in the spin-product basis has
c           off-diagonal elements equal to 0.0
c
            do 170 i=1,nst
            do 170 j=1,nst
            xx(i,j) = 0.0
            zz(i,j) = 0.0
            xd(i,j) = 0.0
            yd(i,j) = 0.0
            zd(i,j) = 0.0
            rho(i,j) = cmplx(0.0, 0.0)
            kk = 0
c
c           diagonal elements (Iz, Sz, rho)
```

```
c          mod(a,b) = int(a/b)
c
           if (i.ne.j) go to 250
           izax = mod(lst(1,i), 2)
           jzax = lst(2,i) - izax
           zd(i,j) = 0.5*grat*(2.0*izax - 1.0)
           zz(i,j) = jzax - (n-1)/2.0
           rho(i,j) = cmplx(zz(i,j), 0.0)
           go to 170
c
c          off-diagonal elements (Ix, Sx, Sy, rho)
c          if 1 spin is flipped an  element is present
c
250        if (iabs(lst(2,i) - lst(2,j)) .ne. 1) go to 170
           ksp=0
           msk=1
           do 220 k=1,n
           if((lst(1,i) .and. msk) .eq. (lst(1,j) .and. msk)) go to 220
           kk = k
           ksp=ksp + 1
220        msk=msk + msk
c
c          I spins
c
           if (ksp.ne.1) go to 170
           if (kk.eq.1) go to 240
           xx(i,j) = 0.5
           if (j.gt.i) yy(i,j) = cmplx(0.0, -0.5)
           if (i.gt.j) yy(i,j) = cmplx(0.0, 0.5)
           go to 170
c
c          S spins
c
240        xd(i,j) = grat/2.0
           if (j.gt.i) yd(i,j) = cmplx(0.0, -grat/2.0)
           if (i.gt.j) yd(i,j) = cmplx(0.0, grat/2.0)
           rho(i,j) = rho(i,j) + cmplx(xd(i,j), 0.0)
170        continue
c
           open(unit=01,name='fid.dat',type='new',err=800)
c
c          loop over pulse strength values ......
c
           write(1,600) nfid
600        format(i14)
           do 400 iv=1,nv
           vv(iv) = d(1)/(v0  +  (iv-1) * vinc)
c
c          calculate cycle time in usec (sampling rate),
c          assuming that all cycles are of the same duration.
c
           ndt = 0
           ni = npul + 1
           nf = npul + ncsteps
           do 410 ipul = ni,nf
           ndt = ndt + tau(ipul)
           ndt = ndt + (flip(ipul)*1000000)/(vv(iv)*360.0)
410        continue
           write(1,600) ndt
           write(1,600) nv
           csr = d(1)/vv(iv)
           write(1,610) iv,vv(iv),csr
```

```
610       format (//,4x,'vv(',i4,' ) = ',e12.6,/,10x,
      1    ' coupling strength =',f12.6)
c
c         generation of the full hamiltonian:  H(internal) + H(rf) .....
c         (upper triangle of matrix only)
c
          do 230 j=1,nst
          do 230 i=1,j
          ij=mat(i,j)
          ham(ij) = hh(ij) - vv(iv)*xx(i,j)
230       continue
c
c         diagonalize the full hamiltonian and get eigenvectors and energies ...
c
          call reigen(ham,u,nst)
c
c         fill in complete transformation matrix UU(nst,nst)
c
          do 210 i=1,nst
          ee(i) = ham(i)
          print 6, i, ee(i)
6         format (2x, i4, 2x, f16.8)
          do 210 j=1,nst
          ij = indx(i,j)
          uu(i,j) = cmplx(u(ij),0.0)
210       continue
c
c         calculate the evolution matrix for each step
c
          k = 0
          kncy = 0
          nnfid = 1
          ni = 1
          nf = npul
          if (npul.eq.0) go to 290
          go to 300
320       kncy = 0
          k = k + 1
310       kncy = kncy + 1
          ni = npul + 1 + (kncy-1)*ncsteps
          nf = npul + kncy*ncsteps
300       do 120 ipul=ni,nf
          if (ntype(ipul).eq.0) go to 130
          tau(ipul)=(flip(ipul)*1000000)/(vv(iv)*360.0)
c
c         examine the pulses first
c         NOTE: pulses may be represented by
c         exp -i*(v*I(phi) + Hint)*tau = exp -i*I(z)*phi
c               exp -i*(v*I(x) + Hint)*tau   exp i*I(z)*phi
c
c         so, the propagator is
c         exp -i*H(phi)*t = exp -i*phi*I(z)   exp -i*H(x)*t   exp i*phi*I(z)
c               = exp -i*phi*I(z)   U   exp -i*H(x)*t   Uadj   exp i*phi*I(z)
c
c         first the set-up the x-pulse matrix
c
          do 140 i=1,nst
          do 140 j=1,nst
          pham(i,j)=cmplx(0.0,0.0)
          phi(i,j)=cmplx(0.0,0.0)
          if (i.ne.j) go to 140
          pham(i,j) = cexp (cmplx (0.0, ee(i)*tau(ipul)*cst))
          rot = zz(i,j)*phase(ipul)*twopi/360.0
```

```
              phi(i,j) = cexp (cmplx (0.0, rot))
140           continue
c
c             find the x-pulse propagator
c
              call umua (uu,pham,nst,zv)
c
c             then rotate about the z-axis
c
              call uamu (phi,pham,nst,zv)
              go to 160
c
c             now examine the delays
c
130           do 150 i=1,nst
              do 150 j=1,nst
              pham(i,j) = cmplx(0.0,0.0)
              if (i.ne.j) go to 150
              pham(i,j) = cexp (cmplx (0.0, e(i)*tau(ipul)*cst))
150           continue
c
c             the propagator for the internal hamiltonian is
c             exp -i*H*t  =  SS  exp -i*E*t  SSadj
c
c
c             multiply, blockwise, SS * PHAM * SSadj
c
              call blkmua (pham,nst,zv,n)
              call blkmau (pham,nst,zv,n)
c
c             evolve the density matrix
c
160           call uamu (pham,rho,nst,zv)
120           continue
c
c             calculate normalization factors
c
290           y = 0.0
              z = 0.0
              do 260 i=1,nst
              do 260 j=1,nst
              y = y + xd(i,j)*xd(j,i)
              z = z + zz(i,j)*zz(j,i)
260           continue
              if (nnfid.eq.1) write(1,270) y, z
270           format(/, 2x,'normalization constant = (I(z)**2)',
     1                 2(2x,f8.4))
c
c             generate an FID by computing observables as a function of time
c
c             to calculate (X), (Y), and (Z) for the S-spin
c                 (A) = Tr (A*rho) = sum over i (A*rho)(ii)
c                     = sum over i [ sum over j (A(ij)*rho(ji)) ]
c
              avex = 0.0
              avey = 0.0
              avez = 0.0
              do 190 i = 1,nst
              do 190 j = 1,nst
              avex = avex + xd(i,j)*rho(j,i)
              avey = avey + yd(i,j)*rho(j,i)
              avez = avez + zd(i,j)*rho(j,i)
190           continue
```

```
        avez = avez/y
        zzz = cmplx(avex/y, avey/y)
        write(1,640) nnfid,zzz,avez
640     format(1x,i4,3f16.8)
        if (nnfid.eq.nfid) go to 400
        nnfid = nnfid + 1
        if (npul.eq.0.and.k.eq.0) go to 320
        if (kncy.lt.ncy) go to 310
        go to 320
c
400     continue
c
        close(unit=01,err=900)
        go to 950
800     type 810
810     format(/,' open error!!',/)
        go to 950
900     type 910
910     format(/,' close error!!',/)
950     continue
        end
c
c
c
c


        subroutine info
c
c       reads and print molecular information and pulse sequence stored
c       in hetdpque.dat
c
        dimension d(50),cj(50),cs(8)
        dimension flip(50),phase(50),tau(50),ntype(50)
        common/dat1/n,nop,voff,d,cj,cs,nfid,grat,ncy,ncsteps
        common/dat2/nv,v0,vinc,npul,ntype,flip,phase,tau
c
        open(unit=01,name='hetdpque.dat',type='old',err=800)
        read(1,600) n
        read(1,600) nop
600     format(i14)
        read(1,610) voff
        do 605 i=1,nop
        read(1,610) d(i)
        read(1,610) cj(i)
605     continue
        do 615 i=1,n
        read(1,610) cs(i)
615     continue
610     format(e12.6)
        read(1,610) grat
        read(1,600) nv
        read(1,610) v0
        read(1,610) vf
        read(1,610) vinc
        read(1,600) npul
        read(1,600) ncy
        read(1,600) ncsteps
        read(1,600) nfid
        nn = npul + ncsteps*ncy
        do 625 i=1,nn
        read(1,600) ntype(i)
        read(1,610) flip(i)
        read(1,610) phase(i)
```

```
         read(1,610) tau(i)
625      continue
         close(unit=01,err=900)
c
         nm1=n-1
         np1=n+1
         type 595,nm1
595      format(/,' the system being studied has 1',
     1       ' carbon and',i3,' protons.',/)
         type 565,grat
565      format(' gamma(S)/gamma(I) = ',f12.6)
         print 500,voff
500      format(6x,'proton offset freq. = ',f7.1,' Hz',//)
         voff=voff/2.0
         print 505
505      format(6x,'dipolar and J couplings (in Hz)',/,6x,31(1h-),/)
         k=0
         do 10 i=1,nm1
         ip1=i+1
         if (i.eq.1) print 570
570      format (' carbon-proton heteronuclear couplings')
         if (i.eq.2) print 575
575      format (' proton-proton homonuclear couplings')
         do 10 j=ip1,n
         k=k+1
         if (v0.gt.0.0) go to 20
         d(k) = -d(k)
         cj(k) = -cj(k)
20       print 510,i,j,d(k),i,j,cj(k)
510      format(6x,'D(',i1,',',i1,') =',f9.2,5x,'J(',i1,',',i1,') =',
     1   f6.2)
c
c        to enable comparison with Rob's couplings
c
         d(k)=d(k)/4.0
         cj(k)=cj(k)/4.0
10       continue
         print 580, cs(1)
580      format (/,' carbon chemical shift (in Hz) =',f10.3)
         print 515
515      format (/,' proton chemical shifts (in Hz)',/)
         print 520,(cs(i), i=2,n)
520      format(6x,8f10.2)
         do 15 i=1,n
15       cs(i)=cs(i)/2.0
c
         print 525, nv
525      format(//,1x,i6,' values of coupling constant considered',/)
         print 530, v0
530      format(8x,'initial value = ',e12.6)
         print 560, vf
560      format(8x,'final value   = ',e12.6)
         print 535, vinc
535      format(8x,'increment     = ',e12.6)
c
         print 585
585      format (' NOTE:  no carbon pulses may be given.')
         if (npul.eq.0) go to 50
         print 540,npul
540      format (5x,'number of steps in the proton',
     1       ' preparation pulse sequence =',i4)
         print 545
545      format(//,2x,'step',2x,'type',2x,'flip angle (deg)',
```

```
      1        2x,'pulse phase (deg)',2x,'delay (usec)',//)
               do 30 i=1,npul
               print 550,i,ntype(i),flip(i),phase(i),tau(i)
550            format(2(3x,i4),3(3x,f8.2))
30             continue
c
50             type 555,nfid
555            format(/,' number of points in the fid =',i4,
      1        '. ',/,
      2        ' Sampling occurs at the beginning of each cycle.')
               print 590,ncy,ncsteps
590            format (/,' there are',i4,' different cycles consisting',
      1        ' of',i4,' steps each.',/)
               print 545
               ni = npul + 1
               nf = npul + ncy*ncsteps
               do 40 i=ni,nf
               in = i - npul
               print 550, in,ntype(i),flip(i),phase(i),tau(i)
40             continue
c
               go to 950
800            type 810
810            format(/,' open error!!',/)
               go to 950
900            type 910
910            format(/,' close error!!',/)
950            continue
               return
               end
c
c
c
c
c
               subroutine blkmua (a,nst,r,n)
c
c              blockwise multiplication of A = X * A
c
               complex a(64,64),r(256),zz
               dimension ss(922),x(20,20),nbc(7),s(400)
               common/ss/ss,s,nbc
c
               np1 = n+1
               kk = 0
               ns = 0
c
               do 100 ib=1,np1
               nb=nbc(ib)
               if (nb.eq.1) x(1,1)=1.0
               if (nb.gt.1) call stuff (nb,kk,ss,x)
c
               do 40 j=1,nst
               do 20 i=1,nb
               zz=0.0
               do 10 k=1,nb
10             zz = zz + x(i,k)*a(ns+k,j)
20             r(i) = zz
               do 30 i=1,nb
30             a(ns+i,j) = r(i)
40             continue
c
               ns = ns + nb
```

```
100       continue
          return
          end
c
c
c
c
c
          subroutine blkmau (a,nst,r,n)
c
c         another blockwise matrix multiplier A = A * Xadj
c
          complex a(64,64),r(256),zz
          dimension ss(922),x(20,20),nbc(7),s(400)
          common/ss/ss,s,nbc
c
          np1 = n+1
          kk = 0
          ns = 0
c
          do 100 ib=1,np1
          nb=nbc(ib)
          if (nb.eq.1) x(1,1)=1.0
          if (nb.gt.1) call stuff (nb,kk,ss,x)
c
          do 40 i=1,nst
          do 20 j=1,nb
          zz=0.0
          do 10 k=1,nb
10        zz = zz + a(i,ns+k)*x(j,k)
20        r(j) = zz
          do 30 j=1,nb
30        a(i,ns+j) = r(j)
40        continue
c
          ns = ns + nb
100       continue
          return
          end
c
c
c
c
c
          subroutine stuff (nb,kk,uu,u)
c
          dimension uu(922), u(20,20)
c
          do 20 j=1,nb
          do 10 i=1,nb
          kk=kk+1
10        u(i,j) = uu(kk)
20        continue
          return
          end
```

APPENDIX C:

HIGH TEMPERATURE NMR APPARATUS

Most crystalline silicates melt at temperatures above 800°C, and many melt at much higher temperatures. In some systems however, true liquids may persist metastably down to glass transition temperatures as low as about 450°C. These high temperatures create experimental difficulties that are more severe for magnetic resonance than for other techniques. In Fourier transform NMR spectroscopy, the nuclear magnetization is excited by application of an intense radiofrequency pulse. As the magnetization returns to equilibrium, a weak current is induced in a rf coil which surrounds the sample. This coil must be close enough to the sample to detect the very small signal (0.01-10 mV) generated by the relaxation of nuclear magnetization and yet be far enough away to avoid becoming heated. High resolution NMR requires the rf electronics to be as cool as possible to reduce instrumental spectral broadening due to poor RLC circuit tuning and matching over a wide temperature range. Cool rf electronics will reduce the thermal noise generated at elevated temperatures, and hence improve the signal-to-noise. Because of restrictions on the bore diameter of high field superconducting magnets and the necessary proximity of sensitive electronic components to the sample, compromises of resolution and/or sensitivity must be made in the design of high temperature NMR probes.

Nonetheless, NMR spectroscopy has been performed at temperatures as high as 1700°C.[36] Two general approaches have been taken in the past: the rf coil needed to excite the magnetization and receive the signal has been placed either outside or inside the furnace. The effect of the design on the signal-to-noise ratio ψ of an NMR exper-

iment is compared using the following simplified expression[6,44]

$$\psi = C \, V_s \, T_c^{-1/2} \, \rho^{-1/4} \, V_c^{\alpha} \quad .$$ (80)

C is a constant, V_s is the sample volume, T_c is the coil temperature, V_c is the coil volume, ρ is the resistivity of the coil material (possibly a refractory metal much less conductive than copper) which may increase rapidly with temperature, and α has been estimated as -1/3 or -1/2.

In the first approach, the rf coil is kept at low temperature, surrounding the furnace, its thermal insulation, and the sample container.[37-39] The cool rf coil ensures the electronic stability (circuit tuning and matching over a wide temperature range) and the low noise operation of the detection system, but severely reduces the ratio of coil volume to sample volume [the "filling factor", $V_s/(2V_c)$], and thus lowers the overall sensitivity. The space available for insulation is also generally very limited, reducing the maximum temperature obtainable. In the second approach,[36,40-43] the rf coil is placed close to the sample, inside the furnace. While this design increases the filling factor and maximum temperature, it also necessitates the use of exotic coil materials, and results in low signal-to-noise ratios and relatively poor resolution because of instrumental broadening.

C.1. Technique

To overcome the seemingly divergent requirements of maintaining cool rf electronics (for maximum resolution and sensitivity) and to

simultaneously optimize the filling factor, an alternative approach has been developed.[102] The sample is pneumatically shuttled between a furnace and a room temperature rf coil. Both the high temperature furnace and NMR probe (which contains all the rf electronics) are enclosed in a double walled stainless steel water jacket which is mounted in the 8.9 cm bore of a vertical 42 kG superconducting magnet as shown in Figure 53.

The sample in the lower position is located at the point of maximum magnetic field H_0 in the solenoid; in the upper position, the field is somewhat lower. Each shuttle cycle is synchronized with the rf pulse generation and data collection by the spectrometer computer. An acquisition cycle consists of shuttling the sample down 15 cm from the center of the furnace to the rf coil center ($\approx$ 0.2 seconds), a high resolution NMR measurement is taken (0.1-0.5 seconds), then the sample is returned to the center of the furnace ($\approx$ 0.2 seconds) where it remains for 10 seconds (for temperature equilibration and also, 10 seconds > 5 T_1). One or more rf pulses are given during each cycle, and a single free induction decay is recorded. The 90° pulse times were about 20 μsec, and a 200 Watt broadband transmitter was generally used. The results of 2 to 400 such cycles are averaged together for every high resolution spectrum obtained.

C.2. Furnace

The non-inductively wound furnace consists of 0.020" 30% Rh-70% Pt thermocouple wire threaded through 20 two hole, 8 mm diameter alumina tubes. A Pt(6%Rh)-Pt(30%Rh) thermocouple also contained in

229

Figure 53: Cross section of high temperature NMR apparatus. Horizon-
tal dimensions are somewhat exaggerated for clarity, and
the drawing is simplified. The bore of the magnet is
8.9 cm, the overall length of the apparatus is about 170
cm. (1) Water jacket plenum. (2) Water jacket (double
walled type 316 stainless steel). (3) Alumina sample
support rod. (4) Alumina tube. (5) Connection to sample
drive cylinder (not shown). (6) Thermal insulation.
(7) Furnace control thermocouple. (8) Furnace (vertical
windings). (9) Boron nitride sample container. (10) Rf
coil on air cooled, teflon support. (11) Water cooled
brass plate. (12) Superconducting solenoid (cryogen
dewar, superinsulation, and shim coils not shown). (13)
Sample container in position for rf pulse. (14) Tuning
electronics on support plates (schematic). (15) Probe
support and air supply tubes. (16) Blanket gas inlet.